UNIVERSIDADE ESTADUAL DE CAMPINAS

Faculdade de Engenharia Química

Marcelle Bruna de Mendonça Spera

On the diffusion of confined hydrocarbon mixtures via molecular dynamics simulation

Sobre a difusão de misturas de hidrocarbonetos confinados usando simulações de dinâmica molecular

CAMPINAS

2021

Marcelle Bruna de Mendonça Spera

On the diffusion of confined hydrocarbon mixtures via molecular dynamics simulation

Sobre a difusão de misturas de hidrocarbonetos confinados usando simulações de dinâmica molecular

Tese apresentada à Faculdade de Engenharia Química da Universidade Estadual de Campinas como parte dos requisitos exigidos para a obtenção do título de Doutora em Engenharia Química.
Dissertation presented to the School of Chemical Engineering of the University of Campinas in partial fulfillment of the requirements for the degree of Doctor in Chemical Engineering

Supervisor: Prof. Dr. Luís Fernando Mercier Franco
Co-advisor: Prof. Dr. Douglas Soares Galvão

ESTE EXEMPLAR CORRESPONDE À VERSÃO FINAL DA TESE DEFENDIDA PELA ALUNA MARCELLE BRUNA DE MENDONÇA SPERA, ORIENTADA PELO PROF. DR. LUÍS FERNANDO MERCIER FRANCO E CO-ORIENTADA PELO PROF. DR. DOUGLAS SOARES GALVÃO

Campinas
2021

Ficha catalográfica
Universidade Estadual de Campinas
Biblioteca da Área de Engenharia e Arquitetura
Rose Meire da Silva - CRB 8/5974

Sp36d

Spera, Marcelle Bruna de Mendonça, 1991-
On the diffusion of confined hydrocarbon mixtures via molecular dynamics simulations / Marcelle Bruna de Mendonça Spera. – Campinas, SP : [s.n.], 2021.

Orientador: Luís Fernando Mercier Franco.
Coorientador: Douglas Soares Galvão.
Tese (doutorado) – Universidade Estadual de Campinas, Faculdade de Engenharia Química.

1. Dinâmica molecular - Métodos de simulação. 2. Coeficiente de difusão. I. Franco, Luís Fernando Mercier, 1988-. II. Galvão, Douglas Soares, 1961-. III. Universidade Estadual de Campinas. Faculdade de Engenharia Química. IV. Título.

Informações para Biblioteca Digital

Título em outro idioma: Sobre a difusão de misturas de hidrocarbonetos confinados usando simulações de dinâmica molecular
Palavras-chave em inglês:
Molecular dynamics - Simulation methods
Diffusion coefficient
Área de concentração: Engenharia Química
Titulação: Doutora em Engenharia Química
Banca examinadora:
Luís Fernando Mercier Franco [Orientador]
Ioannis George Economou
Niels Hansen
Benoit Coasne
Amaro Gomes Barreto Júnior
Data de defesa: 26-07-2021
Programa de Pós-Graduação: Engenharia Química

Identificação e informações acadêmicas do(a) aluno(a)
- ORCID do autor: https://orcid.org/0000-0001-7841-0489
- Currículo Lattes do autor: http://lattes.cnpq.br/1184326558866850

Folha de Aprovação da Tese de Doutorado defendida por **MARCELLE BRUNA DE MENDONÇA SPERA** e aprovada em 26 de julho de 2021 pela Comissão Examinadora constituída pelos Doutores:

Prof. Dr. Luís Fernando Mercier Franco (Presidente / Orientador)

FEQ / UNICAMP

Videoconferência

Prof. Dr. Ioannis George Economou

Texas A&M University at Qatar

Videoconferência

Prof. Dr. Niels Hansen

University of Stuttgart

Videoconferência

Prof. Dr. Benoit Coasne

Université Grenoble Alpes

Videoconferência

Prof. Dr. Amaro Gomes Barreto Júnior

Departamento de Engenharia Química - UFRJ

Videoconferência

Ata de defesa assinada pelos membros da Comissão Examinadora, consta no SIGA/Sistema de Fluxo de Dissertação/Tese e na Secretaria do Programa da Unidade.

To my parents,

who gave me wings to fly.

To my beloved and dearest husband,

who has always flown by my side.

Dr. Watson: You don't seem to
give much thought
to the matter in hand.
Sherlock Holmes: No data yet.
It is a capital mistake to theorize
before you have all the evidence.
It biases the judgment.

A study in scarlet
Arthur Conan Doyle

ACKNOWLEDGMENTS

(in Portuguese)

A Deus, por me abrir as portas e guiar meu caminho até aqui.

Aos meus pais, Geraldo e Eliane, que sempre me incentivaram, ensinaram-me o valor do trabalho e da dedicação, nunca colocando barreiras nos meus sonhos.

À minha irmã, Natalia, por toda a paciência desde sempre com minhas manias e exigências, passando de aluna a colega de profissão. Mas, acima de tudo, companheira para a vida - apenas a uma ligação de distância.

Ao meu marido, Franco, não tenho como colocar em palavras o amor, carinho e admiração que sinto por você. Com certeza seu apoio foi crucial para esse trabalho, desde me escutar incansavelmente treinando apresentações e me ajudar com burocracias, a me distrair e me confortar nos momentos difíceis. Agradeço muito por ter você e o Bilbo em minha vida.

Ao meu orientador, Professor Luís Fernando, que durante esses 4 anos foi muito mais que professor, amigo e psicólogo. É grande minha admiração por você, sua inteligência e dedicação. Agradeço por aguentar meu jeito peculiar de ser, por tudo o que nos ensinou e todo o apoio que sempre nos deu. Sou grata à Prof. Marisa Beppu por nos apresentar.

A Joyce, Rodrigo e Isa, vocês foram cruciais para que esse período do doutorado tenha sido tão memorável e incrível. Para sempre guardarei com carinho nosso tempo juntos!

A todos os membros do LESC, obrigada pelo apoio e por dividir a loucura de trabalhar em um tema tão diferente dentro da FEQ. Em especial, ao Luiz Guilherme, por me acompanhar desde a graduação nos estudos e reviravoltas da vida, e à Flávia e ao Nikolas, pela ajuda na finalização desse trabalho.

A Thiago Pinheiro dos Santos, obrigada por toda ajuda com o cálculo do Soret e pela disponibilidade e paciência para tirar minhas dúvidas.

Ao Professor Douglas Galvão, por ter fornecido a estrutura computacional para realização de todos os cálculos desse trabalho.

Aos Professores Pedro Pessôa e Amaro Barreto, obrigada por participarem da minha qualificação. Suas observações e comentários certamente elevaram a qualidade do texto final. Ao Prof. Pedro: é uma honra tê-lo acompanhando minha trajetória desde o mestrado. Agradeço imensamente por todo seu apoio. Ao Prof. Amaro: muito obrigada por aceitar

novamente participar da minha banca para a defesa. Suas observações no texto da qualificação foram muito importantes!

O presente trabalho foi realizado com apoio do Conselho Nacional de Desenvolvimento Científico e Tecnológico (CNPq) - Processos 155733/2017-6 e 202126/2019-6 .

(in English)

To Professor Joachim Groß, for having me at his research group and providing all support I needed. It was an amazing experience and I will forever be grateful for the opportunity and all the things I have learned.

To Gernot Bauer, Daniel Markthaler, and Prof. Niels Hansen, for the great discussions and all the help with my research topic and its unfolding.

To Prof. Joachim Groß's research group, at ITT, for the welcoming environment and the support even during the pandemic. A special thank you to Elisete Pedrollo, you made my stay there much easier and I am very glad for your friendship - and I still miss our morning coffees! And to Dieter Höhn, who went above and beyond to make sure I was comfortable and well. Also, to Rolf Stierle, Matthias Fischer, and Timm Esper.

To Prof. Benoit Coasne, Prof. Niels Hansen, and Prof. Ioannis Economou, for accepting our invitation to be a part of the defense committee.

RESUMO

Hidrocarbonetos provenientes de reservatórios não-convencionais são encontrados confinados dentro de rochas porosas e esse confinamento altera as propriedades do fluido. Simulação molecular é uma ferramenta computacional que permite o estudo desses sistemas confinados e fornece informações muitas vezes de difícil obtenção experimentalmente. Focando em sistemas de gás natural confinado em nanoporos de calcita, avaliamos por simulações de dinâmica molecular o processo de difusão em misturas de hidrocarbonetos contendo metano. Nós determinamos o comportamento do coeficiente de auto-difusão em diferentes regiões do poro, observando que a anisotropia entre os componentes do tensor de auto-difusão é maior próximo à superfície, o que corrobora resultados anteriores obtidos pelo grupo para componentes puros. Para complementar os dados obtidos, avaliamos a influência do tamanho do poro: a anisotropia no centro do poro tende a diminuir para poros maiores que 10 nm. Notamos também uma dependência dos resultados com a área utilizada para a determinação dos coeficientes de auto-difusão. Quando um gradiente de temperatura é aplicado ao sistema, as interações fluido-parede não correspondem ao perfil de adsorção na condição isotérmica, sugerindo que a distribuição de densidade dentro do poro pode também depender do gradiente de temperatura. Um fenômeno interessante de difusão que possui caracterização experimental complexa é o transporte acoplado de massa e energia chamado termodifusão. Nós calculamos essa propriedade no centro do poro, a qual apresentou valor comparável ao sistema não confinado. Entretanto, reforçamos que para a descrição desse fenômeno em sistemas confinados ainda é necessária uma abordagem que desassocie os efeitos de superfície, confinamento e transporte no não-equilíbrio.

ABSTRACT

Hydrocarbons from unconventional reservoirs are found inside tight porous rocks that alter the fluid properties due to effects from the solid-fluid interactions. Molecular simulation is a reliable computational tool that allows the study of these confined systems and supplement the information unavailable, or very difficult to obtain through experiments. By focusing on a system of natural gas confined within calcite nanopores, we evaluate the diffusion process of hydrocarbon mixtures containing methane by molecular dynamics simulations. We determine the behavior of the self-diffusion coefficient in different regions of the pore, and observed that the anisotropy among the self-diffusion components at different directions is more pronounced near the surface, which corroborates previous results for pure components. To complement the results, we evaluated different pore sizes and saw that for pores greater than 10 nm the anisotropy on the center of the pore becomes smaller. We also noticed a dependency of the results on the region considered for the calculation of the self-diffusion coefficient. When we added a temperature gradient to the system, the fluid-wall interaction was different from the adsorption behavior at isothermal condition, suggesting that the density distribution could also depend on the temperature gradient. One interesting diffusion phenomenon with challenging experimental characterization is the coupled transport of heat and mass called thermal diffusion. We calculate this property within the pore and obtained a result comparable to the one for the system in bulk conditions. Nevertheless, we reinforce that the description of this transport phenomenon under confinement requires attention to properly disentangle the effect of the surface and of the confining geometry to get the true value of the non-equilibrium transport process.

List of Figures

List of Tables

Summary

1 Introduction

Fluids within nanoscale pores exhibit a different phase behavior and transport properties than the ones for unconfined systems, because of the breakdown of the continuum hypothesis as well as the influence of the wall and confinement effects (Barisik and Beskok, 2011; Falk et al., 2015; Zhang et al., 2017). Phenomena under confinement, such as fluid structure and composition of adsorbed phases, mapping of diffusion process, or determination of the pressure tensor inside a pore, can be studied with numerical methods based on statistical mechanics, such as molecular simulation.

As shown in Fig. 1.1, there are different levels of detail we can use to describe matter: *electronic*, *atomistic*, *mesoscale* and *continuum* (Gubbins et al., 2011). Classical molecular simulation is a family of atomistic methods, in which we consider that matter is constitute by discrete particles and they obey the laws of classical mechanics. Details about the electronic structure are lost, but we can model larger systems up to microseconds - compared to a few picoseconds when using electronic level methods. As the time scale increases, the atomic detail is lost. Nevertheless, one can use mesoscale methods (Brownian motion and

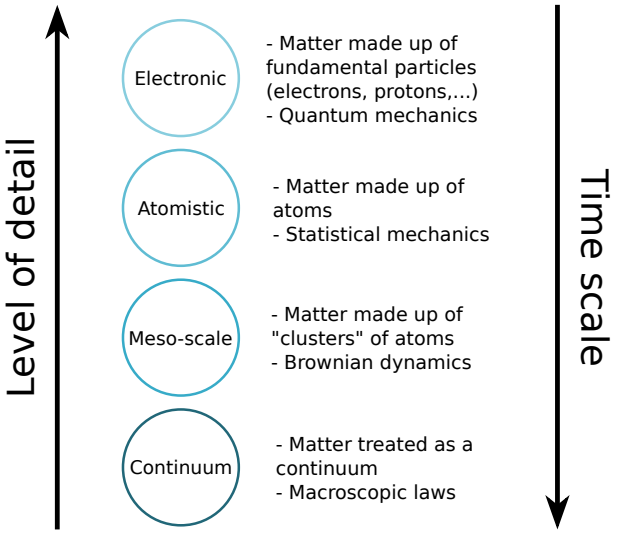

Figure 1.1: Levels of description of matter. A more detailed description implies an evaluation of the system for a smaller time scale.

dissipative particle dynamics - DPD) to connect data obtained from atomistic calculation and upscale molecular simulation results (Bousige et al., 2021).

An example of a confined system is natural gas from unconventional reservoirs. Natural gas is a mixture of hydrocarbons containing mainly methane (Ungerer et al., 2006) that can be found still trapped inside tight pores of its original source rocks. Fluid properties and interactions in confined environments have been widely studied using molecular simulation (Lee et al., 2016; Liu et al., 2017; Le et al., 2020; Santos et al., 2018; Yan et al., 2017; Liu et al., 2018; Wang and Huang, 2019; He et al., 2017). The molecular-level understanding of fluid behavior within nanopores contributes not only to enhance hydrocarbon recovery from these unconventional reservoirs, but also to carbon capture and storage (CCS) technologies (Bui et al., 2018; Ravipati et al., 2021).

The production flow of confined natural gas can be dominated by diffusion (Aguilera, 2016), which is complicated to predict for confined systems because of the influence of the confining geometry and interaction with the surface. Agrawal et al. (2021) reported an example of a counter-intuitive behavior inside silica nanopores: larger hydrocarbons expected to have a stronger interaction with the surface showed a faster self-diffusivity and lower relative density, while volatile and weakly bound fluids had elevated densities and slower self-diffusion.

A special case of diffusion is when it is caused by a thermal gradient, which is called thermal diffusion (or thermodiffusion). This is a coupling effect of temperature and chem-

ical potential gradients, and can have a considerable impact on the system. This is one among many factors that influence the composition of petroleum reservoirs - an important variable in field development planning (Montel et al., 2007; Baghooee et al., 2021). The macroscopically small magnitude of the effect makes it difficult to be measured experimentally and to disentangle from gravity and other external forces. Galliero et al. (2017) sent a microgravimetric experiment to the International Space Station to measure thermal diffusion of multicomponent mixtures of hydrocarbons, aiming to provide reliable data for species distribution inside oil reservoirs. The authors highlight that thermal diffusion seems to counteract the influence of gravitational segregation and reverse the density profile, confirming that thermal diffusion data are crucial to oil and gas industry processes. The confining media introduce an extra challenge that requires caution to evaluate the net effect of thermal diffusion on the system: we must consider the effect of fluid-wall interactions along with the coupled mass transport.

This work is devoted to study confined hydrocarbons using molecular simulation techniques to enlighten the diffusion phenomena occurring under confinement. We calculate the self-diffusion coefficients inside the pore and show how it changes with position, mixture composition, and pore size. Using non-equilibrium techniques, we apply a thermal gradient on the system to evaluate the adsorption behavior and assess the thermal diffusion effect at the central region of the pore.

2

Theoretical background

2.1 Molecular dynamics simulations

Classical Molecular dynamics (MD) simulation is a computational technique used to calculate equilibrium and transport properties of a classical many-body system based on statistical predictions of the system's average behavior (Allen and Tildesley, 2017). As Frenkel and Smit (2002) well described, MD simulations follow the same approach as a real experiment: we first prepare a sample by selecting a N particle system of interest, then the classical equations of motion are numerically integrated for this system until its macroscopically analogous properties no longer change (the system is equilibrated). At last, we can perform the desired measurements.

The system of interest is prepared by creating a simulation box containing the N particles inside a chosen volume V, as shown in Fig. 2.1. Software such as Playmol (Abreu, 2018) or Packmol (Martínez et al., 2009) can be used to randomly assign positions ($\mathbf{r}$) to all particles, creating an initial configuration. Particles initial velocities ($\mathbf{v}$) are assigned

according to Maxwell-Botzmann distribution function (McQuarrie, 2000).

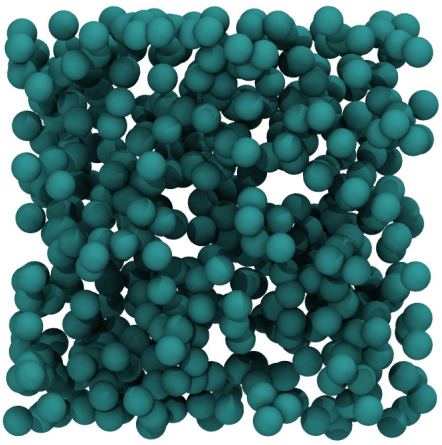

Figure 2.1: Initial configuration of a simulation box with N particles.

For the study of natural gas, our system consists of hydrocarbons confined within calcite nanopores. To describe hydrocarbons, we implicitly account for the hydrogen atoms. This is called a united-atom (UA) approach, in which the molecule is described by clusters of atoms (pseudoatoms) to gain computational performance. To represent the calcite crystal, we consider all five atoms from calcium carbonate ($CaCO_3$) explicitly to accurately reproduce the elastic properties of the material.

From the initial configuration, we can compute the forces acting on those particles using a model to describe the nonbonded potential interaction between them. The adopted interatomic potential is the pairwise-additive Lennard-Jones (LJ) (Eq. 2.2) (Allen and Tildesley, 2017), with r_{ij} the distance between the atoms i and j, ε_{ij} the depth of the potential energy well, σ_{ij} the size of the particles. For charged particles, we have to include an electrostatic potential to describe the long-range interactions. This is done by adding to the LJ potential a Coulombic charge-charge interaction (Eq. 2.3), where k_e is the Coulombic constant, and q the charge of the particles.

$$u_{\text{nonbonded}} = u_{\text{LJ}} + u_{\text{elect}} \tag{2.1}$$

$$u_{\text{LJ}}(r_{ij}) = 4\varepsilon_{ij}\left[\left(\frac{\sigma_{ij}}{r_{ij}}\right)^{12} - \left(\frac{\sigma_{ij}}{r_{ij}}\right)^{6}\right] = \frac{C_{12}}{{r_{ij}}^{12}} - \frac{C_6}{{r_{ij}}^{6}} \tag{2.2a}$$

$$C_{12} = 4\varepsilon_{ij}\sigma_{ij}^{12} \tag{2.2b}$$

$$C_6 = 4\varepsilon_{ij}\sigma_{ij}^{6} \tag{2.2c}$$

$$u_{\text{elect}}(r_{ij}) = k_e \frac{q_i q_j}{r_{ij}} \tag{2.3}$$

LJ parameters and particles charges were taken from traditional force fields in the literature, and the values used in this work are shown in Appendix A. These force fields are models parameterized to experimental data or derived from quantum mechanical calculations to describe the interatomic interactions that will determine the energy of a given configuration.

Interactions between unlike atoms can be estimated from combining rules such as Lorentz-Berthelot (Eq. 2.4) or geometrical averages (Eq. 2.5) when these values are unavailable. We applied the latter to our parameters following the combining rules applied by Xiao et al. (2011) when developing the force field for calcite.

Lorentz-Bethelot:

$$\sigma_{ij} = \frac{1}{2}\left(\sigma_{ii} + \sigma_{jj}\right) \tag{2.4a}$$

$$\varepsilon_{ij} = \left(\varepsilon_{ii}\varepsilon_{jj}\right)^{1/2} \tag{2.4b}$$

Geometrical combining rules:

$$\sigma_{ij} = \left(\sigma_{ii}\sigma_{jj}\right)^{1/2} \tag{2.5a}$$

$$\varepsilon_{ij} = \left(\varepsilon_{ii}\varepsilon_{jj}\right)^{1/2} \tag{2.5b}$$

$$C_{6ij} = \left(C_{6i}C_{6j}\right)^{1/2} \tag{2.5c}$$

$$C_{12ij} = \left(C_{12i}C_{12j}\right)^{1/2} \tag{2.5d}$$

For a molecular system, the total potential function includes bonded interactions (Eq. 2.6) (Allen and Tildesley, 2017). We might treat the chemical bonds and angles as classical

harmonic springs (Eq. 2.7-2.8) or as a rigid unit with fixed bond lengths and angles.

$$u_{\text{TOTAL}} = u_{\text{nonbonded}} + u_{\text{bonds}} + u_{\text{angles}} + u_{\text{torsions}} \tag{2.6}$$

$$u_{\text{bonds}} = \sum_{\text{bonds}} \frac{1}{2} k_r (r_{ij} - r_0)^2 \tag{2.7}$$

$$u_{\text{angles}} = \sum_{\text{angles}} \frac{1}{2} k_\theta (\theta_{ijk} - \theta_0)^2 \tag{2.8}$$

$$u_{\text{torsions}} = \sum_{\text{torsions}} \sum_{n} k_{\phi,n} [\cos(n\phi_{ijkl}) + 1] \tag{2.9}$$

Calculating the forces is always the most expensive step computational-wise of the simulation. To compensate this, it is desired to simulate the smallest system possible. Nevertheless, fewer particles means that more particles are near the simulation box borders, experiencing different forces from those in bulk. To avoid undesired surface effects, we can use periodic boundary conditions (PBC).

PBC consists of replicating the box throughout space to form an "infinite" lattice. During the simulation, a molecule moves in the original box as is shown in Fig 2.2 for a 2D system, and its periodic images in box A,B,C.. move exactly the same way, keeping the number density constant. The use of PBC usually has little effect on fluids away from phase transitions and when interactions are short-ranged (Allen and Tildesley, 2017).

Using the minimum image convention, we can compute the potential energy between a molecule and its neighbours, regardless of the particle being at the original box or one of its images (Fig. 2.3). To avoid calculating a large number of interactions, we apply a spherical cutoff (dashed circle on Fig. 2.3), setting the potential energy to 0 for $r_{ij} > r_c$, where r_c is the cutoff radius. This should be sufficiently large to ensure that it will be only a small perturbation, and no greater than half of the box size so particles will not interact with their own image.

Once the forces are calculated, the equations of motion can be integrated. Commonly used algorithms for it are the leap-frog (Eq. 2.10) or velocity-Verlet (Eq. 2.11) (Allen and Tildesley, 2017). The resulting time evolution of positions, $\mathbf{r}(t)$, and velocities, $\mathbf{v}(t)$, is called a system's *trajectory*.

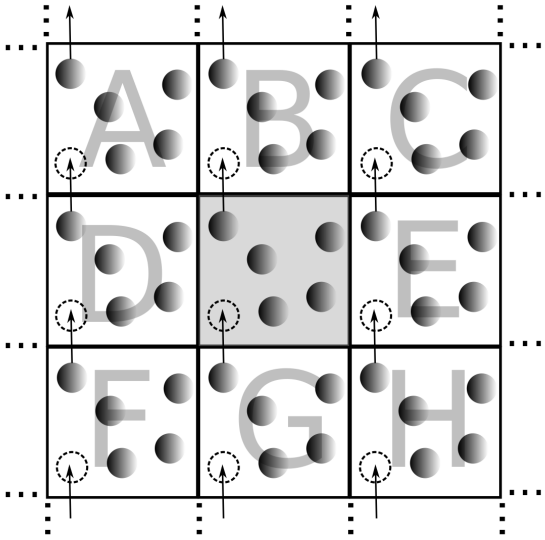

Figure 2.2: Periodic boundary conditions for a 2D system. Original box in gray and its images labeled with letters. Figure inspired by Fig. 1.13 from Allen and Tildesley (2017).

Leap-frog:

$$\mathbf{r}(t+\delta t) = \mathbf{r}(t) + \delta t \mathbf{v}\left(t + \frac{1}{2}\delta t\right) \tag{2.10a}$$

$$\mathbf{v}\left(t + \frac{1}{2}\delta t\right) = \mathbf{v}\left(t - \frac{1}{2}\delta t\right) + \delta t \mathbf{a}(t) \tag{2.10b}$$

$$\mathbf{v}(t) = \frac{1}{2}\left[\mathbf{v}\left(t + \frac{1}{2}\delta t\right) + \mathbf{v}(t - \frac{1}{2}\delta t)\right] \tag{2.10c}$$

Velocity-Verlet:

$$\mathbf{r}(t+\delta t) = \mathbf{r}(t) + \delta t \mathbf{v}(t) + \frac{1}{2}\delta t^2 \mathbf{a}(t) \tag{2.11a}$$

$$\mathbf{v}(t+\delta t) = \mathbf{v}(t) + \frac{1}{2}\delta t[\mathbf{a}(t) + \mathbf{a}(t+\delta t)] \tag{2.11b}$$

where $\mathbf{a}$ is the acceleration vector.

The *natural* ensemble to simulate systems within MD is the microcanonical, in which the number of particles, N, the volume, V, and the total energy, E, are constants. If we want to fix other variables such as temperature, T, or pressure, p, modifications to the

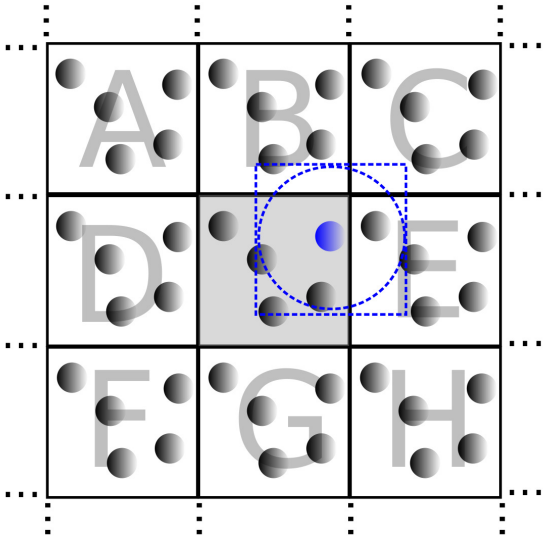

Figure 2.3: Representation of minimal image convention, where a particle (in blue) interacts with its neighbors regardless if they are from the original box. Dashed circle representing the cutoff radius that delimit the particles for which the pair-wise potential is calculated. Original box in gray and its images labeled with letters. Figure inspired by Fig. 1.16 from Allen and Tildesley (2017)

equations of motion should be introduced.

There are tools to control the system and perform a simulation at constant temperature, and the methods are referred to as thermostats. One of them is the Nosé-Hoover (Nosé, 1984; Hoover, 1985), which adds artificial coordinates and velocities to the equation of motion to allow a dynamic energy flow between a heat bath and the system, controlling its temperature. Stochastic methods such as the Andersen thermostat (Andersen, 1980) simulate a collision to a heat bath by changing the velocity of a randomly chosen particle, making the system jump to another energy state. This method requires no change in the dynamical algorithm, updating the momenta in a conservative way. The sudden change in velocity leads to a decorrelation that affects the system dynamics. For this reason, such a thermostat is not recommended for the study of transport properties (Frenkel and Smit, 2002). Bussi et al. (2007) proposed a modified velocity-rescaling thermostat, where the velocity of all particles are multiplied by a factor that changes the kinetic energy of the system based on its previous value. With a smoother evolution, dynamical properties were compatible with the literature, and with values extracted from NVE simulations.

To perform a simulation at constant pressure for homogeneous fluids, a change in the simulation box volume is required - which can be included as a dynamical variable. If the

system is inhomogenous, one may need to change the shape of the simulation box as well (Frenkel and Smit, 2002). Commonly used barostats are Berendsen (Berendsen et al., 1984) and Parrinello-Rahman (Parrinello and Rahman, 1981).

The analysis of the system trajectory consists of calculating a property and observing how it changes as a function of time. The most useful statistical quantities that can be calculated from the simulated data are averages, fluctuations, and time correlation functions (Eqs. 2.12 - 2.14) (Field, 2007).

Average:

$$\langle X \rangle = \frac{1}{n} \sum_{i=1}^{n} X_i \tag{2.12}$$

Fluctuations:

$$\langle (\delta X)^2 \rangle = \langle (X - \langle X \rangle)^2 \rangle = \langle X^2 \rangle - \langle X \rangle^2 \tag{2.13}$$

Correlation function:

$$\langle \delta X(t) \delta X(0) \rangle = \langle X(t) X(0) \rangle - \langle X \rangle^2 \tag{2.14}$$

where X is the property under consideration.

These quantities can be related to macroscopic data through statistical mechanics. Temperature and pressure can be determined by averages, heat capacities by fluctuations, and transport properties by time correlation functions. To account for the dependency of diffusion coefficients with the finite-size simulated system when periodic boundary conditions are applied, one should consider corrections such as the one proposed by Yeh and Hummer (2004) (Eq. 2.15). The analytical expression based on the hydrodynamic interactions, considering the shear viscosity (η) independent of system size, reads as follows:

$$D_\infty = D_{\mathrm{PBC}} + 2.837 \frac{k_{\mathrm{B}} T}{6 \pi \eta L_{\mathrm{box}}} \tag{2.15}$$

here, D_{PBC} is the diffusion value calculated from the simulation data using periodic boundary conditions, k_{B} is the Boltzmann constant, T the absolute temperature, and L_{box} the length of the cubic simulation box.

To correct for the perturbation caused by the truncated LJ potential with a cutoff, one needs to apply long-range corrections. These should be carefully applied to inhomogenous systems, since its properties change with position and the spherical symmetry is lost. The Ewald method (also applied to long-range forces) and a larger cut-off are possible approaches when available. We refer the reader to a recent publication from Nitzke et al. (2021) for more details on the long-range corrections for inhomogeneous fluids with a spherical interface.

2.2 Non-equilibrium methods

Time correlation functions represent the average response to naturally occurring fluctuations in the system properties (which are very small). Nevertheless, signal-to-noise ratio can be unfavourable at long times, which could affect the calculation of certain properties. Non-equilibrium molecular dynamics (NEMD) is an alternative that improves the efficiency with which transport coefficients are calculated. Here, this technique will be briefly introduced based on the monographs of Evans and Morriss (2008) - chapter 6, Kjelstrup and Bedeaux (2008) - chapter 22, and Allen and Tildesley (2017) - chapter 11.

In NEMD, classical equations of motion are numerically integrated for a system under a gradient in one of its intensive variables. Gradients can be applied by adding to the equations of motion a perturbation term ($\mathcal{F}$) dependent on momentum ($\mathbf{p}$) and/or positions ($\mathbf{r}$) of the particles (Eq. 2.16), or by setting different boundary conditions to the system.

$$\dot{\mathbf{r}} = \frac{p}{m} + \mathcal{F}(t) \tag{2.16a}$$

$$\dot{\mathbf{p}} = f + \mathcal{F}(t) \tag{2.16b}$$

The idea is that much larger fluctuations can be induced and transport properties such as viscosity, thermal conductivity, and diffusion are measured by creating a flux ($\mathbf{J}_\alpha$) in the system and relating systems linear response to the perturbation field to a transport

coefficient (Eq. 2.17) (Cummings and Evans, 1992).

$$\text{Transport property} = \lim_{\mathcal{F}\to 0} \lim_{t\to\infty} \frac{\mathbf{J}_\alpha}{\mathcal{F}} \tag{2.17}$$

2.2.1 Boundary driven NEMD

In the case of setting different boundary conditions to the system, we have the so-called boundary driven NEMD (BD-NEMD). For the simulation of unconfined systems using BD-NEMD, the simulation box is usually elongated as shown in Fig. 2.4. The reason is to give a substantial bulk region for measuring transport coefficients using unperturbed equations of motion, once the effect is restricted to the boundaries. These boundary regions have to be carefully selected to create a symmetry when applying periodic boundary conditions (PBC), avoiding the direct contact of regions with opposite effects, for example.

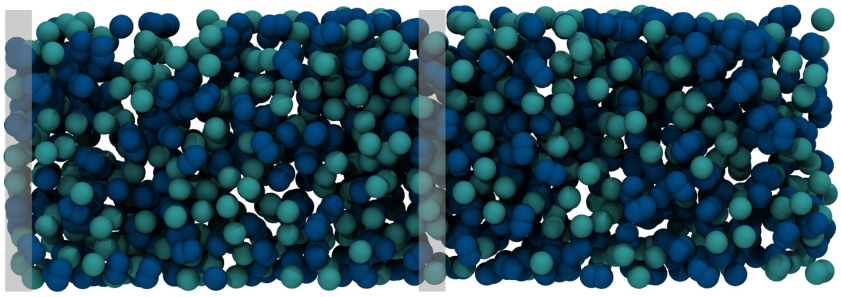

Figure 2.4: Elongated box for simulating unconfined systems using NEMD. Gray areas to represent the regions where the system is perturbed, respecting the symmetry requested for the use of PBC (see text).

Irreversibilities are introduced by controlling some variables in the desired region of the system. We can apply a gradient in chemical potential/concentration by particle swapping, or a temperature gradient by setting different temperatures to each region. The system reaches a steady-state once the flux $\mathbf{J}_\alpha$ becomes constant.

To monitor local properties after steady-state is reached, one can average over a layer with only a few particles for long time intervals to replace an average over many particles. This equivalence between time and ensemble averages is related to the ergodic hypothesis. The temperature profile, for example, can be calculated by determining the local temperature in each layer from the average kinetic energy according to the equipartition principle (Eq. 2.18). Figure 2.5 shows the resultant temperature profile of a non-equilibrium system

under a temperature gradient.

$$\frac{3}{2}Nk_{\mathrm{B}}T = \frac{1}{2}\sum_{i\in\text{layer}} m_i|\mathbf{v}_i|^2 \tag{2.18}$$

where N is the number of particles in the layer, k_{B} Boltzmann constant, T the absolute temperature, m_i the mass of each particle i, and $\mathbf{v}$ the velocity vector.

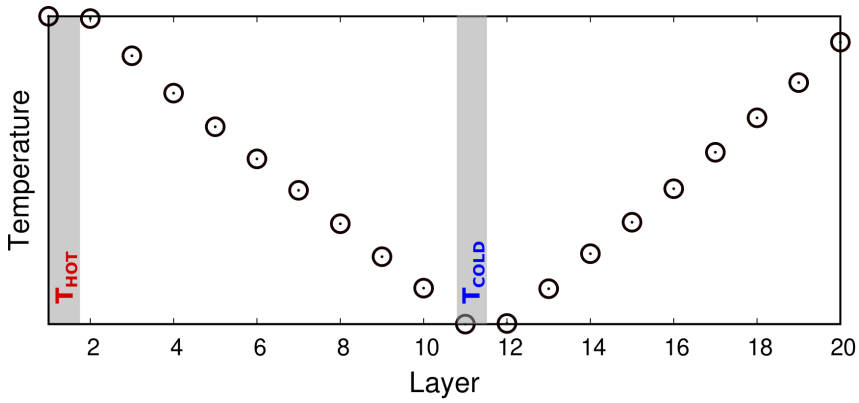

Figure 2.5: Temperature profile for a non-equilibrium system under a temperature gradient. Gray areas from Fig. 2.4 where set to different temperatures and Eq. 2.18 used to calculate the local temperature in each layer.

For confined systems, solid-fluid interactions can be measured by introducing perturbations on the confining walls. A temperature gradient can be established by thermostatting only the wall particles, and allowing a thermal gradient to develop in the fluid. In this work, we applied a dual-pore simulation box (Fig. 2.6) to avoid contact between walls with different temperatures. Since for confined systems the pore size is an important variable, the elongated box is no longer required.

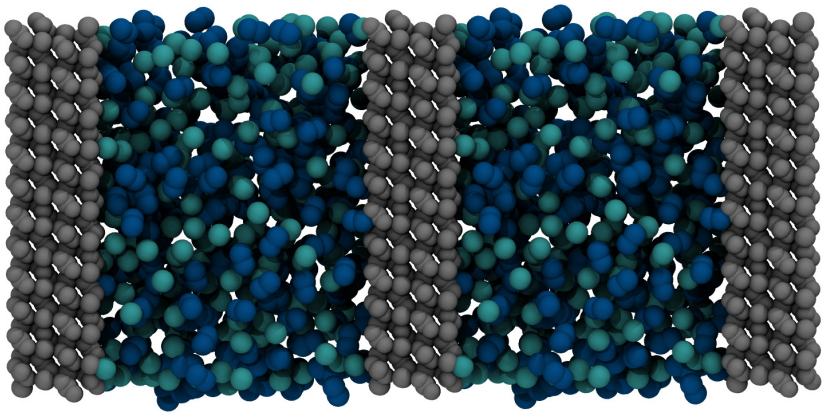

Figure 2.6: Dual-pore simulation box for BD-NEMD of confined systems. Perturbation is applied only to the walls (gray).

Properties can be calculated from slabs with only a few particles, but we must be careful to use methods that account for the confinement effect and the non-equilibrium condition.

How to choose between equilibrium and non-equilibrium methods? Equilibrium simulations allow the calculation of all transport coefficients from a single run, which is very interesting when the simulation is expensive to run due to a complicated molecular model, for example. Non-equilibrium simulations provide only one fundamental transport coefficient plus the cross-coupling coefficients with the applied perturbation (Evans and Morriss, 2008). Nevertheless, by simulating non-equilibrium systems, one can get molecular insight into systems behavior and visualize physical mechanisms that are important to the transport processes, as can be observed from our adsorption results on Chapter 5. NEMD is valuable technique for the analysis of heterogeneous systems, which have a difficult experimental characterization, being very useful to understand transport in porous media, and for micro/nanofluidics (Galliero, 2010; Bonella et al., 2017; Jackson et al., 2016).

2.3 Self-diffusion

Self-diffusion is the interdiffusion of same species particles, *i.e.*, the natural motion of molecules resulting from particle collisions (Santos et al., 2021). The self-diffusion can be expressed from the continuity equation (Eq. 2.19) and the corresponding Fick's law for a single particle (Eq. 2.20), where the interdiffusion D in this case would be the same as the self-diffusion (Hansen and McDonald, 2013). This yields the diffusion equation also known as Fick's second law (Eq. 2.21) (Crank, 1975), which is simply a microscopic mass balance.

$$\frac{\partial \rho(\mathbf{r},t)}{\partial t} + \nabla \cdot \mathbf{J}(\mathbf{r},t) = 0 \tag{2.19}$$

$$\mathbf{J}(\mathbf{r},t) = -D\nabla\rho(\mathbf{r},t) \tag{2.20}$$

$$\frac{\partial \rho(\mathbf{r},t)}{\partial t} = D\nabla^2\rho(\mathbf{r},t) \tag{2.21}$$

Einstein derived an expression (Eq. 2.22) that relates the motion of the particles with the macroscopic transport coefficient (Frenkel and Smit, 2002), giving the microscopic

interpretation of the self-diffusion coefficient, D.

$$D = \lim_{t \to +\infty} \frac{1}{2d} \frac{\partial \langle r^2(t) \rangle}{\partial t} \tag{2.22}$$

with r the particle position, and d the number of dimensions considered for the calculation of the coefficient.

This expression can be readily translated to a computer algorithm to calculate the self-diffusion from molecular dynamics simulations by measuring the distance $\Delta \mathbf{r}_i(t)$ that every particle i travelled in time t (that is, the mean-squared displacement - MSD), and averaging over the total number of particles N (Eq. 2.23).

$$\langle \Delta r^2(t) \rangle = \frac{1}{N} \sum_{i=1}^{N} \Delta \mathbf{r}_i(t)^2 \tag{2.23}$$

By plotting the result from Eq. 2.23 *versus* time, as shown in Fig. 2.7, the self-diffusion coefficient can be calculated from the slope of the curve.

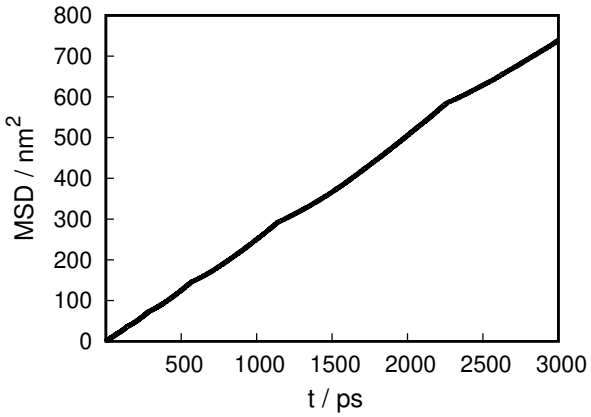

Figure 2.7: Average mean-squared displacement $\langle \Delta r^2(t) \rangle$ *versus* time for bulk methane at 375 K.

An equivalent alternative to Einstein's method is the Green-Kubo formulation (McQuarrie, 2000), in which the self-diffusion coefficient is calculated from the time integral of the velocity autocorrelation function (Eq. 2.24).

$$D = \frac{1}{d} \int_0^{\infty} \langle \mathbf{v}_i(t) \cdot \mathbf{v}_i(0) \rangle \mathrm{d}t \tag{2.24}$$

Self-diffusion coefficients of each component of a mixture can be related to mutual diffusion through Maxwell-Stefan (MS) relations (Fernández et al., 2005; Santos et al.,

2021). For binary mixtures, one possible approach is through Darken's equation, where the self-diffusion coefficient of each species, D_{A} and D_{B}, is related to MS diffusion coefficient ($Đ_{\mathrm{AB}}$) by species mole fraction x (Eq. 2.25).

$$Đ_{\mathrm{AB}} = D_{\mathrm{A}} x_{\mathrm{B}} + D_{\mathrm{B}} x_{\mathrm{A}} \tag{2.25}$$

To compare MS diffusion coefficients to experimental data, we must take into account the thermodynamic non-ideality of the mixture (Santos et al., 2021). For this reason, the thermodynamic factor, Γ, must be included (Eq. 2.26 - Krishna and Van Baten (2005)). This factor can be obtained from an equation of state or directly from the simulation using Kirkwood-Buff integrals (Kirkwood and Buff, 1951; Schnell et al., 2011; Dawass et al., 2019; Schnell et al., 2014).

$$D_{\mathrm{AB}} = \Gamma Đ_{\mathrm{AB}} \tag{2.26a}$$

$$\Gamma = 1 + x_{\mathrm{A}} \left(\frac{\partial \ln \gamma_{\mathrm{A}}}{\partial x_{\mathrm{A}}} \right)_{T,p} \tag{2.26b}$$

where D_{AB} is the mutual diffusion coefficient (from Fick relations) comparable to experimental measurements, and γ is the activity coefficient, with the partial derivative taken at constant temperature and pressure (Santos et al., 2021).

2.3.1 Confined systems

MD can also be used to calculate properties for inhomogeneous fluids, but the approaches for large-scale, bulk systems cannot be applied to fluids under confinement. These fluids are subjected to surface effects that cause an inherent inhomogeneity due to the solid-fluid interactions (Barisik and Beskok, 2011; Bhatia et al., 2011; Falk et al., 2015; Franco et al., 2016a).

In the case of an inhomogeneous fluid, the diffusion properties depend on the direction in which they are measured (Crank, 1975). When confined, the mean square displacement of the particles are bounded by the confining region, with different diffusion coefficients for different regions (Liu et al., 2004). The equilibrium spatial distribution of particles

is nonuniform, hence methods derived from the ordinary diffusion equation considering smooth spatial variations are unsuitable.

Instead of Fick's phenomenological equation, a more suitable approach would be methods based on the Smoluchowski equation (Eq. 2.27). This equation describes the time evolution of a particle's density and is a generalization of the diffusion equation (Eq. 2.21) for the case where there is an external force acting on the particles (Hansen and McDonald, 2013).

$$\frac{\partial p(\mathbf{r},t)}{\partial t} = -\boldsymbol{\nabla}\cdot\mathbf{J} = \boldsymbol{\nabla}\cdot\mathbf{D}e^{-\beta W(\mathbf{r})}\cdot\boldsymbol{\nabla}\left[e^{\beta W(\mathbf{r})}p(\mathbf{r},t)\right] \tag{2.27}$$

where $p(\mathbf{r},t)$ is the probability density function, $\mathbf{r}$ the position vector, $\mathbf{J}$ the particle flux through the boundaries, $\mathbf{D}$ the diffusion tensor, $\beta = 1/(k_{\mathrm{B}}T)$ (k_{B} being the Boltzmann constant, and T the absolute temperature), and $W(\mathbf{r})$ is the potential of the mean force related to the density profile.

The break of symmetry due to the presence of an interface can lead to anisotropies between the components of the diffusion tensor. For a slit pore (Fig. 2.8), where the inhomogeneity is only in one direction (here, z direction), one has components of the diffusion tensor parallel (x and y) and perpendicular (z) to the interface.

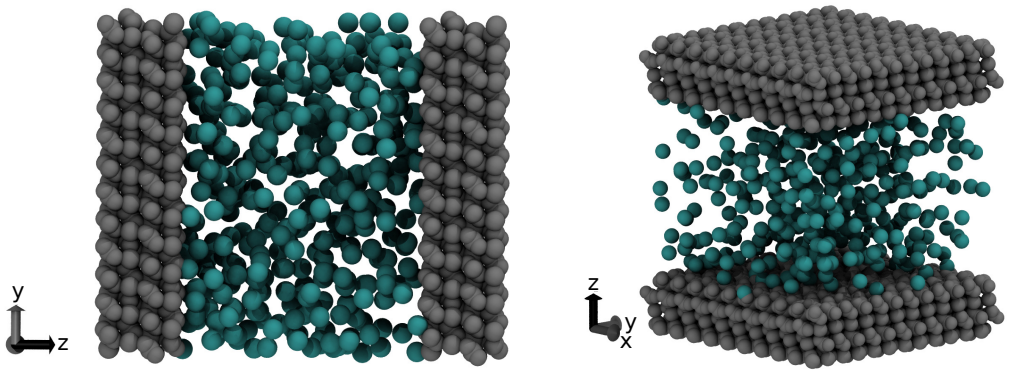

Figure 2.8: System confined in a slit pore geometry.

Parallel components

Liu et al. (2004) proposed a new methodology to calculate the parallel components of the diffusion tensor for an inhomogenous system. The position-dependency of the diffusion coefficient was addressed by dividing the system in thin layers (Ω) parallel to the interface

and applying the Smoluchowski equation to each layer. The diffusion coefficient is the same for each layer, but may change from layer to layer (especially close to the interface). Since at the parallel directions the system is unbounded, the Smoluchowski equation becomes Eq. 2.28.

$$\frac{\partial p(r,t)}{\partial t} = D_{\parallel}\frac{\partial^2 p(r,t)}{\partial r^2} \tag{2.28}$$

The mean square displacement is calculated as an extension of the Einstein formulation (Eq. 2.22) considering the survival probability of the particle inside of each layer. For that, one tags the particles initially inside the layer, and follows for how long they stay in that region - disregarding when these molecules re-enter the layer by removing its tag once it leaves. These values are calculated from the simulation trajectory as follows. First, the layer is chosen based on the density profile. For example, in Figure 2.9 the layer closer to the confining material was chosen, where the density is higher due to adsorption and surface interaction.

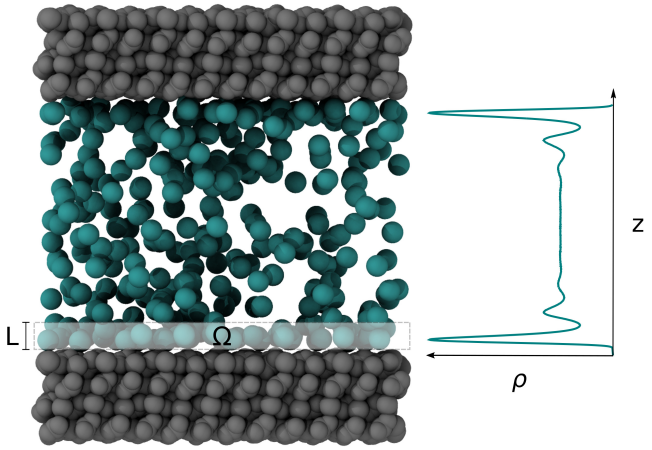

Figure 2.9: Layer Ω of width L chosen for the calculation of the parallel self-diffusion coefficients. On the right side, the equilibrium density profile of the system used as guide to determine the layer.

Then, the mean square displacement inside Ω is determined for the tagged particles through Eq. 2.29, considering multiple time origins, and averaging over the total number of particles initially inside the layer, $N(t_0)$.

$$\langle \Delta r^2(t) \rangle_{\Omega} = \frac{1}{\tau}\sum_{t_0=0}^{\tau-1}\frac{1}{N(t_0)}\sum_{i\in\Omega(t_0,t_0+t)}(r_i(t_0+t) - r_i(t_0))^2 \tag{2.29}$$

The survival probability is calculated as the ratio of the particles remaining in the layer over the number of particles initially there, as shown in Eq. 2.30.

$$P(t) = \frac{1}{\tau} \sum_{t_0=0}^{\tau-1} \frac{N(t_0, t_0 + t)}{N(t_0)} \tag{2.30}$$

with τ the number of time steps required for all the initial particles to leave the layer. From these calculations, we get profiles such as the ones from Fig. 2.10.

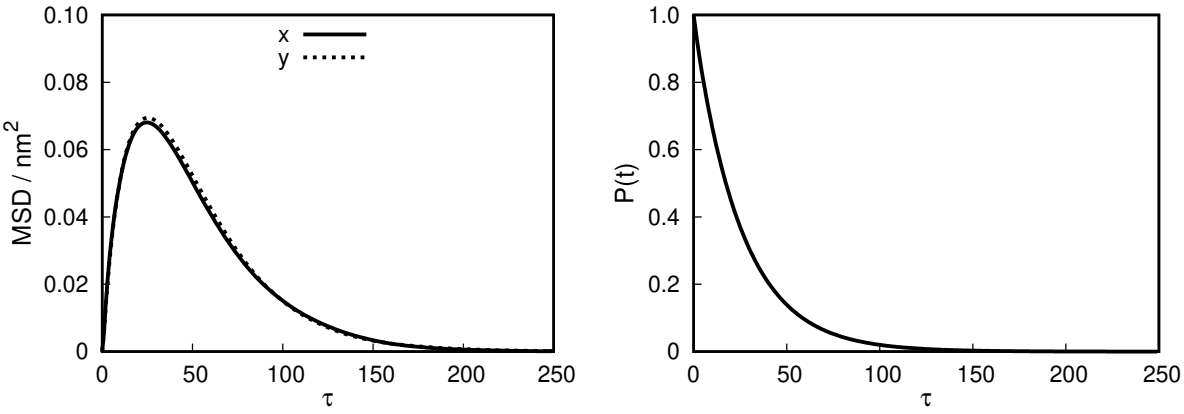

Figure 2.10: Mean square displacement and survival probability for the particles inside a layer of width $L = 0.35$ nm. Data for methane confined within a calcite slit pore at 375 K.

Finally, the parallel components of the self-diffusion tensor at each layer Ω are calculated from Eq. 2.31 as the slope of the mean square displacement over the survival probability *versus* time (Figure 2.11). For this calculation, we consider only a linear region, such as the interval $5 < t < 20$.

$$D_{\parallel} = \lim_{t \to \infty} \frac{\langle \Delta r^2(t) \rangle_{\Omega}}{2tP(t)} \tag{2.31}$$

The self-diffusion coefficient under confinement differs from bulk values and can be higher or lower depending on the confining material (Tsimpanogiannis et al., 2019). For statistical purposes, one can simulate the system using different initial configurations or simulate the same system for a longer time, divide the final trajectory into smaller ones, and calculate the self-diffusion coefficient for each one.

Simonnin et al. (2017) investigated the effect of the shape of the slit pore on the parallel self-diffusion coefficients calculated from MD simulations. They concluded that the use of elongated boxes (wide pores, with the length at z direction greater than 2.8

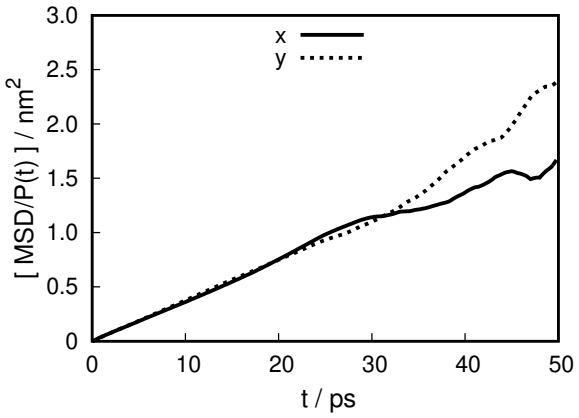

Figure 2.11: Ratio of mean square displacement and survival probability from Fig. 2.10 used for the calculation of $D_{\parallel}$.

times the length of x and y directions) introduced considerable finite-size effects. That shows that care should be taken when creating the initial configuration and analyzing the results.

Perpendicular component

Several methods to calculate the self-diffusion component normal to the interface based on the Schmoluchowski equation were proposed (Liu et al., 2004; Mittal et al., 2008). We use in this work the methodology developed by Franco et al. (2016b), who determine the coefficient from the integration of the survival probability after solving the Smoluchowski equation for a linear potential of the mean force.

The Smoluchowski equation for the perpendicular direction is given by:

$$\frac{\partial p(r,t)}{\partial t} = \frac{\partial}{\partial r}\left[D_{\perp} e^{-\beta W(r)} \frac{\partial}{\partial r}[e^{\beta W(r)} p(r,t)]\right] \tag{2.32}$$

By considering again a layer thin enough that the diffusion coefficient remains unchanged with position inside the layer, and hence is independent of r, Eq. 2.32 becomes Eq. 2.33.

$$\frac{\partial p(r,t)}{\partial t} = D_{\perp}\left[\frac{\partial^2 p(r,t)}{\partial r^2} + \frac{\partial}{\partial r}\left(p(r,t)\beta \frac{\partial W(r)}{\partial r}\right)\right] \tag{2.33}$$

To apply the variable separation method, one needs to assume that the solution is separable in terms of time and space (Eq. 2.34). This was assessed by the authors

comparing the analytical solution to numerical results with good agreement.

$$p(r,t) = R(r)T(t) \tag{2.34}$$

The layer reduced size also allows the assumption of a linear potential of the mean force, $W(r)$, (Eq. 2.35).

$$e^{-\beta W(r)} = \frac{\rho(r)}{\langle\rho\rangle} \tag{2.35a}$$

$$-\beta W(r) = \ln\left[\frac{\rho(r)}{\langle\rho\rangle}\right] = \omega r + \xi \tag{2.35b}$$

$$\ln\left[\frac{\rho(r)}{\rho*}\right] = \omega r + \xi' \tag{2.35c}$$

where ξ is the linear coefficient and $\xi' = \xi + \ln(\langle\rho\rangle/\rho^*)$, with $\rho(r)$ the density distribution, $\langle\rho\rangle$ the average density, and ρ^* a normalization parameter. Now, Eq. 2.33 may be rewritten as Eq. 2.36.

$$\frac{\partial p(r,t)}{\partial t} = D_\perp\left[\frac{\partial^2 p(r,t)}{\partial r^2} - \omega\frac{\partial p(r,t)}{\partial r}\right] \tag{2.36}$$

Defining the survival probability $P(t)$ as the integral of the probability density function inside the layer (Eq. 2.37) and the residence time, τ_r, as the integral of the survival probability (Eq. 2.38), one can get the expression for the perpendicular self-diffusion coefficient (Eq. 2.39).

$$P(t) = \int_0^L p(r,t)\mathrm{d}r \tag{2.37}$$

$$\tau_r = \int_0^{+\infty} P(t)\mathrm{d}t \tag{2.38}$$

$$D_\perp = \frac{L^2}{\alpha\tau_r} \tag{2.39}$$

with L being the width of the layer, and α a parameter related to the potential of mean

force. For a linear potential of mean force, α is given by Eq. 2.40.

$$\alpha^{-1} = 4\omega L \frac{(e^{\omega L}+1)}{(e^{\omega L}-1)} \sum_{j=0}^{+\infty} \left[(2j+1)^4\pi^4 + \frac{3\omega^2 L^2}{4}(2j+1)^2\pi^2 - \frac{\omega^4 L^4}{4} \right]^{-1} \tag{2.40}$$

For further details, the reader is referred to the original work (Franco et al., 2016b).

To calculate this coefficient from the simulation trajectory, we start by choosing a layer where the assumption of the linear potential of the mean force is valid. Fig. 2.12 exemplifies one of the possible regions.

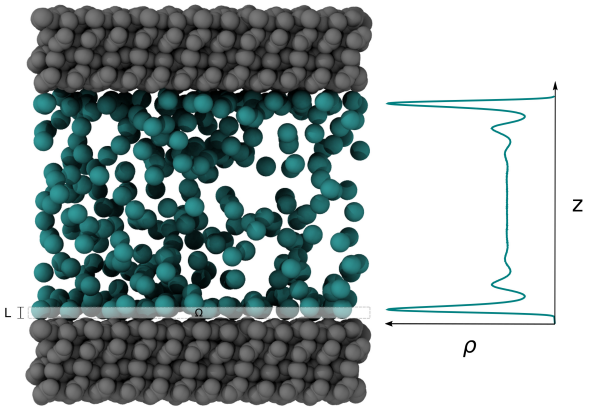

Figure 2.12: Layer Ω of width L chosen for the calculation of the perpendicular self-diffusion coefficient. On the right side, the equilibrium density profile of the system used as guide to determine the layer where the potential of mean force would be linear.

Then, survival probability is calculated for the particles inside Ω using Eq. 2.30 and also considering multiple time origins. Fig. 2.13 shows the resulting profile for the survival probability. Comparing with the profile for the parallel directions (Fig. 2.10), the average number of time steps τ that a particle stays inside Ω is much lower at the normal direction. That is a result of the smaller size of the layer and its height/width ratio.

Trapezoidal rule is used to integrate the survival probability and to calculate the residence time, τ_r. Then, α could be determined. The layer width L is already chosen from the density profile. The parameter ω related to the potential of mean force is obtained from Eq. 2.35c as the derivative of the density profile with the position (Eq. 2.41). To calculate this derivative from simulation data, we use the method of the least squares to do a regression analysis and obtain ω as the slope of the curve.

$$\omega = \frac{\partial \ln \rho(r)}{\partial r} \tag{2.41}$$

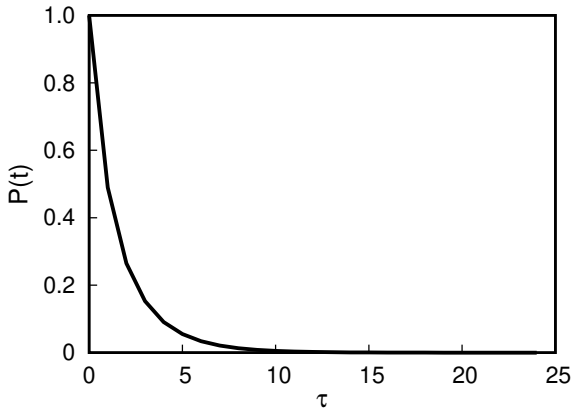

Figure 2.13: Survival probability for the particles at layer Ω from Fig. 2.12. Data for methane confined within calcite slit pore at 375 K. The layer width was $L = 0.15$ nm.

The sum from equation 2.40 is calculated from $j = 0$ to $j = 20$. As can be seen from Fig. 2.14, the sum quickly reaches a plateau.

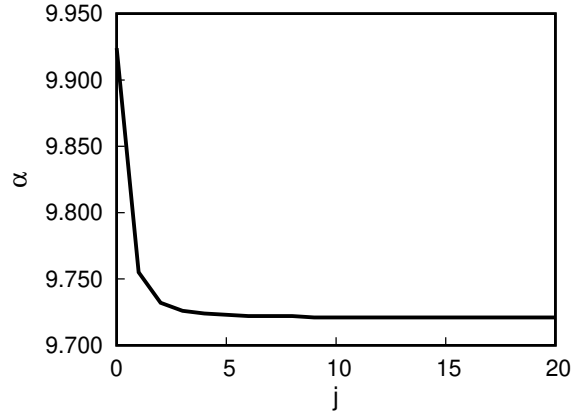

Figure 2.14: Evolution of α with j values of the sum term from Eq. 2.40. Data for the system of Fig. 2.13.

$D_\perp$ is, therefore, calculated from Eq. 2.39. This methodology can also be applied to bulk systems, where $\omega \to 0$ due to no position-dependent potential of mean force, and hence $\alpha = 12$ (Franco et al., 2016b).

2.4 Thermal diffusion

As previously mentioned, a temperature gradient can also lead to mass transport. This coupled effect is called thermal diffusion (de Groot and Mazur, 1984). From the phenomenological equations of non-equilibrium thermodynamics (Eq. 2.42), we assume a linear relation between forces and its conjugate vectorial fluxes (Evans and Morriss,

2008).

$$\mathbf{J}_i = \sum_j L_{ij}\mathbf{X}_j \tag{2.42}$$

L_{ij} are the phenomenological transport coefficients that relate forces $\mathbf{X}_j$ and fluxes $\mathbf{J}_i$, also known as the Onsager coefficients. When $i = j$, the coefficients can be related to single transport coefficients such as diffusion and thermal conductivity. When $i \neq j$, the coefficients describe coupling between fluxes and are called *coupling coefficients*. For the case of coupled mass and heat transport, we have the following relations (assuming no electrical current):

$$\mathbf{J}_\mathrm{q} = L_\mathrm{qq}\nabla\left(\frac{1}{T}\right) + L_{\mathrm{q}\mu}\left(-\frac{1}{T}\nabla\mu\right) \tag{2.43a}$$

$$\mathbf{J} = L_{\mu\mathrm{q}}\nabla\left(\frac{1}{T}\right) + L_{\mu\mu}\left(-\frac{1}{T}\nabla\mu\right) \tag{2.43b}$$

here, $\mathbf{J}_\mathrm{q}$ is the heat flux (defined as the energy flux excluding convection), $\mathbf{J}$ is the mass flux, T the temperature, and μ the chemical potential (Kjelstrup et al., 2017). The coupling coefficient $L_{\mu\mathrm{q}}$ relates the transport of mass to a temperature gradient, and is used to define the thermal diffusion coefficient, D_T.

To determine thermal diffusion from equilibrium MD simulations, an approach similar to Eq. 2.24 could be used by applying a cross-correlation function between heat and mass fluxes (Eq. 2.44) (Vogelsang et al., 1987). Extra care should be taken when evaluating the heat flux, $\mathbf{J}_\mathrm{q}$, remembering to subtract enthalpic contributions from the total energy flux.

$$D_T = \frac{1}{3Vk_\mathrm{B}T}\int_0^\infty \langle \mathbf{J}(0)\mathbf{J}_\mathrm{q}(t)\rangle \mathrm{d}t \tag{2.44}$$

The ratio of the thermal diffusion and the mutual diffusion coefficients is called the Soret coefficient, s_T. Assuming a binary mixture, after the system reached the steady-state - which means no more net mass flux, the Soret coefficient can be calculated as Eq. 2.45, with c_A the concentration of component A in mol·m^{-3} and r the direction of the transport (Kjelstrup et al., 2017). This coefficient usually has the magnitude of 10^{-3} to

10^{-5} K^{-1} for both gases and liquids mixtures (de Groot and Mazur, 1984).

$$s_T \equiv -\frac{1}{c_A}\left(\frac{\partial c_A/\partial r}{\partial T/\partial r}\right)_{J=0} = \frac{D_T}{D_{AB}} \tag{2.45}$$

We can calculate the Soret coefficient from non-equilibrium molecular dynamics simulations data by applying a temperature gradient to the system. Once the system reached a steady-state, and the concentration gradient is established, the Soret coefficient of a binary mixture can be determined from the concentration and temperature profiles, as shown in Eq. 2.46 (Furtado et al., 2015).

$$s_T = \frac{D_T}{D_{AB}} = \frac{1}{x_A x_B}\frac{\nabla x_A}{\nabla T} \tag{2.46}$$

with x the mole fractions of components A and B, calculated for each layer as previously described for the temperature (Fig. 2.5).

The content of this chapter was reprinted with adaptation from Spera, M. B. M and Franco, L. F. M. ***Surface and confinement effects on the self-diffusion coefficients for methane-ethane mixtures within calcite nanopores.*** *Fluid Phase Equilib. 522, 112740 (2020). https://doi.org/10.1016/j.fluid.2020.112740*

3

Surface and confinement effects on the self-diffusion coefficients for methane-ethane mixtures within calcite nanopores

The study of transport properties of unconventional oil reservoirs such as shale gas is crucial to optimize production, enhance oil extraction, and to decrease costs and environmental hazards. One important dynamical property of fluids is diffusion, which is necessary to determine the oil mobility and rate of oil production from the reservoir, and can be obtained through the self-diffusion coefficient. To obtain the transport properties of fluids under confinement, one must take into account the surface and the confinement effects. Moreover, approaches that consider the position-dependency and the nonlinear particle distribution are required. Applying methods based on probability density function, the self-diffusion components of methane-ethane mixtures confined within calcite nanopores were calculated, using molecular dynamics simulations. The anisotropy between xx, yy,

and zz components of the self-diffusion tensor has different effects depending on the position within the nanopore. A surface effect causes an anisotropic behavior between parallel self-diffusion coefficients for this mixture close to the calcite walls. And at the center of the pore, the confinement effect is manifested by lowering the value of the perpendicular self-diffusion coefficient when compared to the parallel ones. Mixture composition plays an important role, since a higher ethane content shows greater anisotropy between parallel components.

3.1 Introduction

Nanoconfinement changes fluid properties because of two main phenomena: the surface effect caused by the fluid-wall interactions, and the geometric constraints resulting from the confinement itself (Walton and Quirke, 1989; Mu and Malhotra, 1991; Alfi et al., 2017). The combination of these two effects impose an inhomogeneous fluid particle distribution within the confined media (Franco, 2019; Travalloni et al., 2014; Gelb et al., 1999; Tsimpanogiannis et al., 2019; Nygård, 2016). Predicting the surface and confinement effects is relevant for industrial applications such as separation processes (Travalloni et al., 2010b,a), heterogeneous catalysis (Polarz et al., 2010), general adsorption phenomena (Franco et al., 2017; Araújo and Franco, 2019; Otero et al., 2004; Sato et al., 2010), and also for unconventional oil extraction, for which the fluid is found confined within porous rocks.

The understanding of fluid transport in unconventional reservoirs is crucial to optimize the production, enhance extraction performance, avoid losses, and decrease costs and undesired environmental effects (Simonnin et al., 2018; Lee et al., 2016; Agrawal and Sharma, 2020). Interfacial forces and pore geometry have strong influence on the dynamics of the confined fluids (Rabbani et al., 2017; Setu et al., 2015), and the experimental challenges in probing confined media place simulations at the heart of what has been applied to investigate such nanosystems. Chen et al. (2015b) applied the Lattice Boltzmann Method to simulate the fluid flow and diffusion inside complex shale structures. Falk et al. (2015) used Molecular Dynamics simulations to show that the continuum hypothesis is unsuitable to describe hydrocarbon transport in nanoporous media due to adsorption.

Molecular simulation has been a powerful tool to investigate confined systems, with

great progress regarding the effect of confinement on fluid properties and characterization of confining surfaces for tight oil and gas reservoirs (Dysthe et al., 2002; Santos et al., 2018; Brasili et al., 2019; Striolo and Cole, 2017; Chen et al., 2015a; Patankar et al., 2016; Collell et al., 2015; Jin and Firoozabadi, 2015; Sharma et al., 2015; Mosher et al., 2013; Yuan et al., 2015). Regarding the diffusion process, Franco et al. (2016a) have shown that the parallel self-diffusion coefficients of pure methane, nitrogen, and carbon dioxide near calcite walls present an anisotropic behavior. Bui et al. (2017) confirmed these results, and reported that hydration and chemical composition of the pore can affect this phenomenon. Wu et al. (2017) have addressed the dependence of the self-diffusion values on the confining mineral, as well as Fazelabdolabadi and Alizadeh-Mojarad (2017). Wu and Firoozabadi (2018) claimed that the transport process affects the composition of the produced gas mixture due to selective adsorption - the fluid behavior at different compositions should be taken into account.

In this work, we analyze the surface and the confinement effect on self-diffusion data for methane-ethane mixtures confined within a calcite slit pore. Calcite is the most stable polymorph of calcium carbonate, and can be found as the most abundant mineral on some shale reservoirs (Addari and Satta, 2015; Rexer et al., 2014; Littke et al., 1988). We show the effect of the mixture composition and the position-dependency of the self-diffusion coefficients. The results were obtained with classical equilibrium Molecular Dynamics (MD) simulations, applying adequate methods that account for the effect of surface and confinement in different regions of the pore.

3.2 Computational details

3.2.1 MD simulations

Mixtures of methane and ethane were confined between two parallel plates of calcite, as shown in Figure 3.1. The calcite plane considered was $\{10\bar{1}4\}$ orthogonal to the z direction with xyz dimensions 4.990 nm x 4.856 nm x 1.212 nm. The pore size was fixed as $H = 3.5$ nm along the z axis. All simulated systems had overall density of 250 kg·m^{-3}, and the results shown here are for systems simulated at 375 K. Details about the phase behavior of the components in bulk conditions at this temperature with an accurate equation of state (PC-SAFT) can be found in Appendix B.

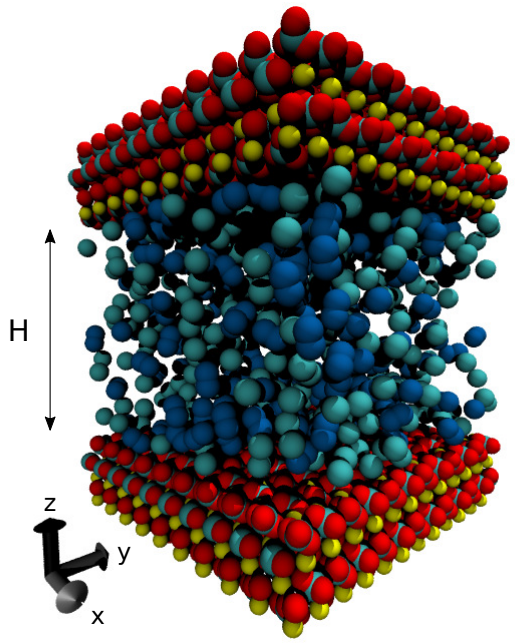

Figure 3.1: 3D plot of initial configuration: methane-ethane mixture confined inside calcite slit pore.

We performed MD simulations with GROMACS 5.0.2 (Abraham et al., 2015), using the Leap-Frog algorithm for the numerical integration of the equations of motion, with a time step of 2 fs. TraPPE force field (Martin and Siepmann, 1998) was applied to hydrocarbons, and Xiao et al. (2011) force field was applied to the calcite crystal, with a cutoff radius of 1.0 nm. Crossed parameters for fluid-wall interactions were calculated using geometrical combining rules. The Particle Mesh Ewald method (Darden et al., 1993) was used to calculate the electrostatic interactions, and a velocity-rescale thermostat (Bussi et al., 2007) was used to control the temperature of the system, with relaxation time $\tau_T = 1.0$ ps. Periodic boundary conditions were applied to all directions, and no tail corrections were applied due to the inhomogeneity of the systems (Franco et al., 2016b; Allen and Tildesley, 2017). Positions and velocities were stored every 0.2 ps.

Each system was equilibrated at the canonical ensemble for 20 ns followed by 50 ns of production time at the same ensemble. For statistical purposes, the trajectory was divided in 5 blocks of 10 ns each to calculate the standard deviations of self-diffusion coefficients.

3.2.2 Self-diffusion calculation

Self-diffusion is the average displacement of a molecule from its initial position in a system without a chemical potential gradient or external forces, being caused by thermal molecular motion. The self-diffusion coefficient is useful for estimating transport diffusion, an important dynamic property of fluids (Hopp et al., 2018; Kamala et al., 2004; Chempath et al., 2004; Keffer and Adhangale, 2004).

In the case of an inhomogeneous fluid, new methods to calculate the components of the self-diffusion tensor have been proposed (Liu et al., 2004; Franco et al., 2016b; Mittal et al., 2008), considering the break of symmetry due to the confining walls. At a confined environment, there is a non-uniform particle distribution, leading to different diffusion at different regions. We calculate the position-dependent components of the self-diffusion coefficient parallel to the walls following the method of Liu et al. (2004):

$$D_{||} = \lim_{t \to +\infty} \frac{\langle \Delta r^2(t) \rangle_\Omega}{2tP(t)} \tag{3.1}$$

where $\langle \Delta r(t)^2 \rangle_\Omega$ is the mean square displacement of the centers of mass, and the survival probability $P(t)$ is calculated as the ratio between the number of centers of mass that remain in the layer Ω between t_0 and t, $N(t_0, t_0 + t)$, and the number of centers of mass within layer Ω at t_0, $N(t_0)$, considering multiple time origins:

$$P(t) = \frac{1}{\tau} \sum_{t_0=0}^{\tau-1} \frac{N(t_0, t_0 + t)}{N(t_0)} \tag{3.2}$$

The perpendicular component is obtained following the method described by Franco et al. (2016b):

$$D_\perp = \frac{L^2}{\alpha \tau_r} \tag{3.3}$$

where L is the layer width, α is a parameter related to the potential mean force, and τ_r is the residence defined as (for further details, the reader is referred to Franco et al. (2016b)):

$$\tau_r = \lim_{t \to +\infty} \int_0^t P(t) \mathrm{d}t \tag{3.4}$$

All the aforementioned aproaches are based on the Smoluchowski equation (Equation 3.5), which describes the time evolution of the probability density, and is suitable for systems with a non-uniform spatial distribution at equilibrium (Hummer, 2005; Liu et al., 2004):

$$\frac{\partial p(\mathbf{r},t)}{\partial t} = -\boldsymbol{\nabla}\cdot\mathbf{J} = \boldsymbol{\nabla}\cdot\mathbf{D}e^{-\beta W(\mathbf{r})}\cdot\boldsymbol{\nabla}\left[e^{\beta W(\mathbf{r})}p(\mathbf{r},t)\right] \tag{3.5}$$

where $p(\mathbf{r},t)$ is the probability density function, $\mathbf{r}$ the position vector, $\mathbf{J}$ the particle flux through the boundaries, $\mathbf{D}$ the diffusion tensor, $\beta = 1/(k_{\mathrm{B}}T)$ (k_{B} being the Boltzmann constant, and T the absolute temperature), and $W(\mathbf{r})$ is the potential of the mean force.

We implemented both methods using C programming language to analyze the simulation trajectory. All post-processing codes were developed at this work.

3.3 Results and discussion

Diffusion under confinement greatly differs from diffusion in unconfined media. The diffusion near the walls is influenced by adsorption, which results in a larger density of molecules at the interface (Wang et al., 2016; Bocquet and Barrat, 1996; Keffer and Adhangale, 2004). The particle distribution for confined methane is presented in Figure 3.2, where the different areas, considered for calculation of the self-diffusion coefficients in this study, are highlighted.

Figure 3.3 shows the density profile of pure hydrocarbons confined within calcite walls at the same density and pore size as the mixtures. At the center of the pore, further from the walls, the effect of the confining surface, that restricts the movement on the direction of confinement, can be observed. The parallel self-diffusion coefficients have essentially the same value in this region, but the perpendicular self-diffusion coefficient is much lower. Close to the walls, a large density variation is observed due to the fluid-surface interactions, but at the center of the pore, the density is uniform. Therefore, the differences between the parallel and the perpendicular diffusion coefficients entail a pure confinement effect. The trace of the resulting self-diffusion tensor in this region, however, is comparable to the unconfined self-diffusion values. Franco et al. (2016a) have shown that, increasing the pore size, the differences between the parallel and perpendicular self-diffusion coefficients at the center of the pore decreases.

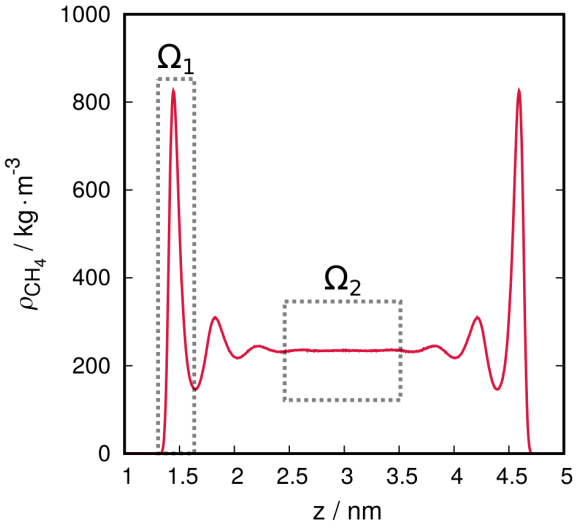

Figure 3.2: Density profile showing areas Ω_1 (wall) and Ω_2 (center) considered for calculation of the self-diffusion coefficients. Data for pure methane confined within calcite walls.

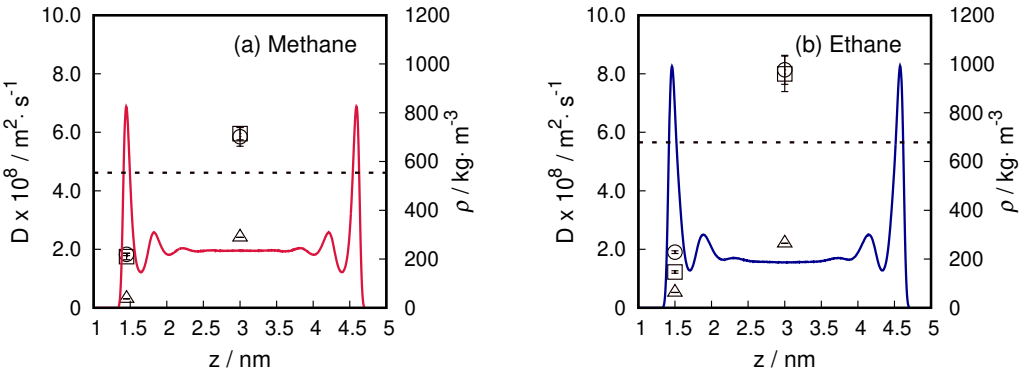

Figure 3.3: Position-dependent self-diffusion coefficients of pure components. D_{XX}: squares; D_{YY}: circles; $D_{\perp}$: triangles. The filled line shows the density profile inside the pore. The dashed line shows the unconfined self-diffusion average value calculated with Einstein's method at the same temperature and density, and corrected for finite-size effects (Yeh and Hummer, 2004).

Close to the walls, an anisotropic behavior between the parallel self-diffusion coefficients emerges, as one can see in Figure 3.3b. This anisotropy has been explained as a consequence of the surface effect, in particular, due to the structural arrangement of the calcite crystal and the first fluid adsorbed layer (Franco et al., 2016a). The question that is yet to be addressed is whether or not the same phenomena are observed for mixtures, and how the mixture composition affects such phenomena. Figure 3.4 shows the results for different regions of the pore for confined methane-ethane mixtures with

different compositions at 375 K, with a pore size of 3.5 nm.

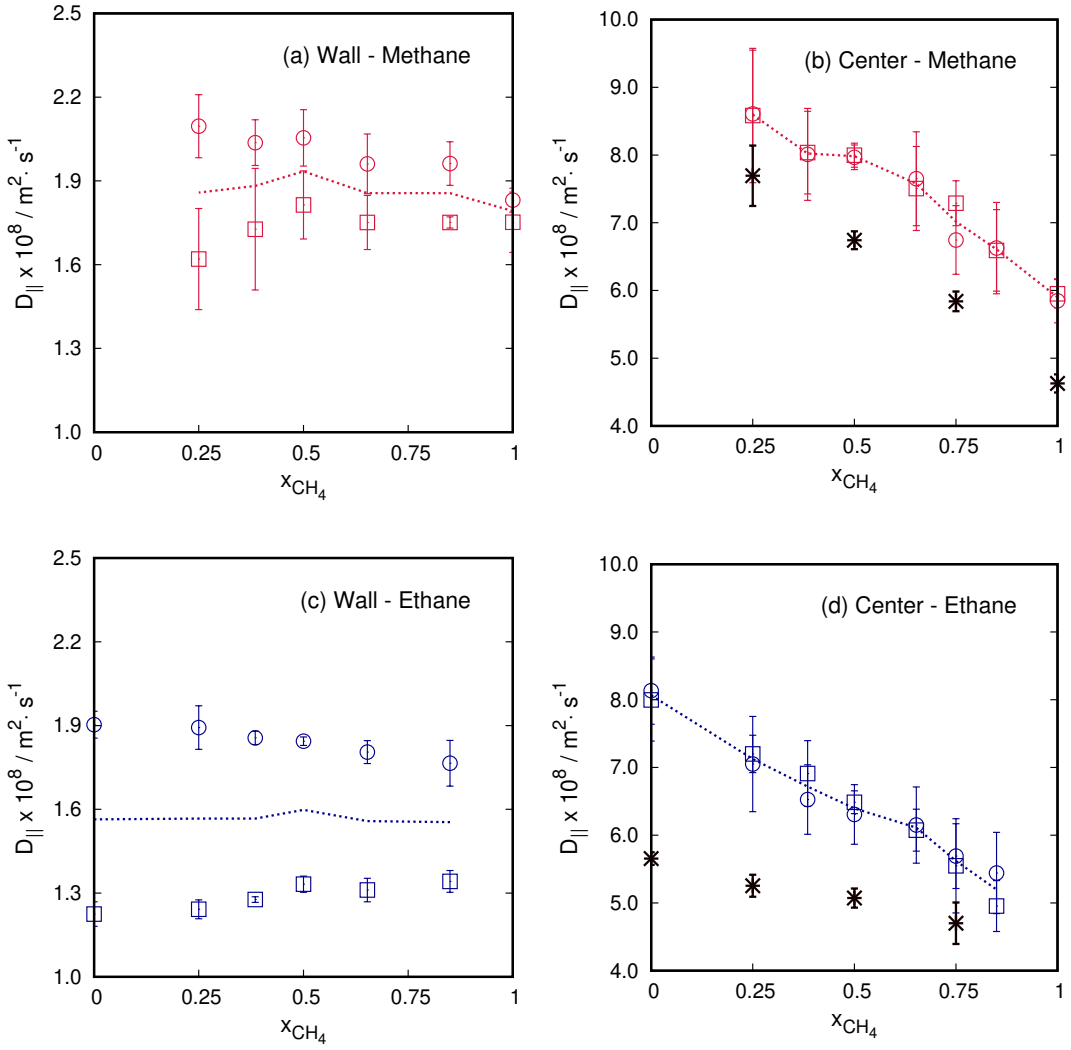

Figure 3.4: Effect of mixture composition on the parallel components of the self-diffusion for different regions of the pore. D_{XX}: squares; D_{YY}: circles. Black stars for the unconfined mixture, for which $D_{XX} = D_{YY}$. The dashed line is the arithmetic average between D_{XX} and D_{YY} of each components.

An anisotropic behavior between the parallel components of the self-diffusion tensor is observed near the walls regardless of the mixture composition, which implies that the same surface effect observed for the pure systems is found for adsorbed mixtures. The anisotropy is greater between ethane parallel self-diffusion components than between methane parallel self-diffusion components, and the difference between D_{XX} and D_{YY} also decreases increasing methane mole fraction. This implies that the presence of ethane alters methane self-diffusion, increasing the anisotropic behavior between methane parallel self-diffusion coefficients. Nevertheless, the average value of the parallel components near

the walls remains reasonably constant. At the center of the pore (Figure 3.4b,d), no anisotropic behavior between parallel components is observed, and the magnitude of self-diffusion coefficients is 3-4 times higher than near the walls. This is most probably related to the density variation within the pore. The total density is much larger close to the walls, decreasing particles mobility.

As for the perpendicular component, to calculate the α parameter from Equation 3.3, we assumed that the layer is sufficiently small so that the potential of the mean force can be considered linear. For that reason, the layer considered for this calculation near the wall was $\Omega_1/2$, i.e., a linear density profile. The calculation of the perpendicular self-diffusion coefficient is unfeasible for some systems using this method because the relaxation time of local density fluctuations may become faster than the time required for particles to diffuse, considering the evaluated small layer (Mittal et al., 2008). A possible solution is to increase the system size, but this has an enormous impact on the required computational effort. For the center of the pore, the whole length of Ω_2 can be used.

The values obtained for the perpendicular component near the walls were one order of magnitude smaller than the values of the parallel components (Figure 3.5a), and they seem to remain unaffected by changes in mixture composition. The slower motion of the molecules near the walls in the direction of confinement is due to layering, which creates a barrier for diffusion in z direction.

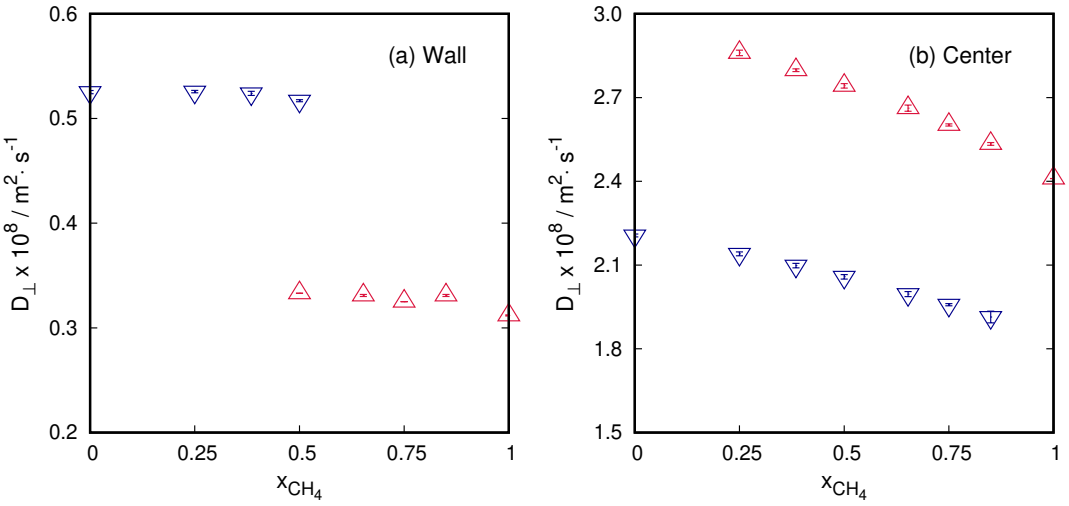

Figure 3.5: Composition dependency of the perpendicular coefficients of the self-diffusion tensor for different regions of the pore. Red triangles for methane and blue down-pointing triangles for ethane.

The presence of confining walls affects the diffusion at the center of the pore for small pore sizes. At the center of the pore (Figure 3.5b), the values of the perpendicular self-diffusion coefficients were about 3 times smaller than the parallel ones, following the same trend of decreasing with the increase of methane content. Franco et al. (2016a) have shown that bulk-like behavior is only observed for pure methane confined within calcite nanopores for pores larger than 15 nm.

Two interesting points emerge from the results. The first one, shown in Figure 3.5a, is that the diffusion of ethane is higher than that for methane. Nevertheless, the average local self-diffusion of methane is still higher. One possible explanation would be the preferential adsorption of ethane by the calcite crystals, resulting in a greater anisotropy between the parallel components and a smaller effect on the perpendicular direction to maintain the diffusion tensor trace.

The second point is the behavior of the self-diffusion with the increase of methane mole fraction. Keffer and Adhangale (2004) have studied the composition dependency of self-diffusion of an unconfined methane-ethane mixture, and have shown that the self-diffusion coefficients of both components increase with methane mole fraction, which is the opposite of what we have observed for the confined mixture. Pressure may be the answer for such a different behavior. Our systems were simulated at same mass density, temperature, and volume. This implies that the higher the methane content, the higher the number of molecules within the pore to keep the same mass density, which increases the pressure of the system. And, increasing pressure, the values of the self-diffusion coefficients of methane and ethane under confinement are decreased, as shown by Sharma et al. (2015), which corroborates our results.

3.4 Conclusion

We have studied the surface and the confinement effect on the self-diffusion coefficients of methane-ethane mixtures confined by calcite nanopores, using classical equilibrium molecular dynamics simulations.

Close to the calcite walls, the same anisotropic behavior previously observed for pure components was found for confined methane-ethane mixtures. This surface effect significantly affects the mobility of the adsorbed fluids in all directions. This means that

parallel self-diffusion coefficients are different in different directions, and achieve much higher values than the perpendicular self-diffusion coefficient.

At the center of the pore, the surface effect that causes the anisotropic behavior between parallel self-diffusion coefficients vanishes, and the confinement effect acts on the perpendicular self-diffusion coefficient. The mixture composition plays an important role in the dynamics at the center of the pore, and, increasing methane mole fraction, keeping the same density and temperature, all diagonal components values of self-diffusion tensor decrease, which is probably a consequence of the higher pressures.

The surface and the confinement effects are usually mixed terms in the literature, and, in fact, they are often coupled. Nevertheless, in this work, we have shown that, even for a tight nanopore (3.5 nm), they play different roles. The anisotropic behavior between the parallel self-diffusion coefficients close to the walls vanishes at the center of the pore, which means that the surface itself is sufficiently far from the center of the pore. But, at the same time, the proximity of the two walls is enough to cause an anisotropic behavior for the perpendicular self-diffusion coefficients, when compared to the parallel ones, and this is a direct consequence of the confinement effect. Because of these effects, the determination of each component of the self-diffusion tensor in confined media is necessary, and adequate methods to calculate such diffusion coefficients must be employed.

4

A deeper look into self-diffusion under confinement

In this chapter, some parameters that affect the calculation of the self-diffusion tensor and the behavior of diffusion under confinement are analyzed. We further discuss the method used to determine the perpendicular component, calculate the profile throughout the pore, and how pore size influences the self-diffusion tensor of a methane-ethane equimolar binary mixture. A possible alternative way to determine the perpendicular self-diffusion at the central region of the pore (constant density) is suggested.

4.1 Simulation details

Pure methane and ethane, as well as their equimolar mixture were studied. The fluids were confined between two parallel plates of calcite, as shown in Figure 4.1. The pore size was fixed as $H = 3.5$ nm along the z axis, unless otherwise specified. All systems

were simulated at 375 K and had overall density of 250 kg·m^{-3}. Further details of the simulation procedure can be found in Chapter 3 (section 3.2.1).

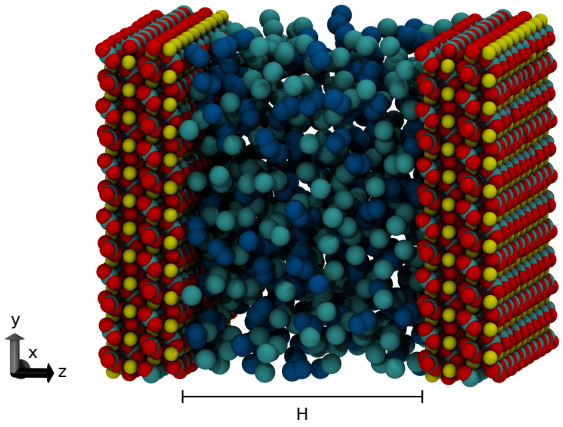

Figure 4.1: 3D plot of initial configuration: methane-ethane mixture confined inside calcite slit pore.

4.2 Perpendicular component

For the calculation of the perpendicular component of the self-diffusion tensor, we used the methodology proposed by Franco et al. (2016b) (Eq. 4.1) - further described in section 2.3.1. This requires the determination of a layer of width L where the density profile is linear, and in this section we will evaluate the effect the choice of the layer interval has on the results.

$$D_{\perp} = \frac{L^2}{\alpha \tau_r} \tag{4.1}$$

where α is the parameter related to the potential of mean force and τ_r the residence time.

We will consider the higher density peak for this analysis, for which a small variation of the boundary values can highly impact the average density of the layer and hence the self-diffusion component. As an example, Fig. 4.2 shows the density profile of pure methane confined inside a calcite slit pore of aperture 3.5 nm at 375 K. Highlighted, the region from 1.33 nm to 1.39 nm, corresponding to the beginning of the first density peak on the left side. The local density goes from zero to higher than 200 kg·m^{-3} within this small 0.06 nm range.

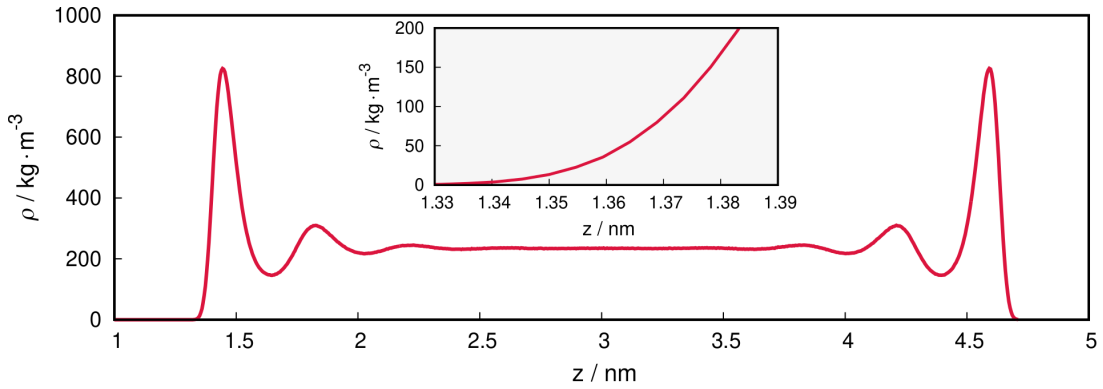

Figure 4.2: Density profile of pure methane confined within a calcite slit pore of 3.5 nm at 250 kg·m^{-3} and 375 K. The inset plot shows a zoom view of the beginning of the first high density peak.

Now, we will see how the parameters for the perpendicular component of the self-diffusion change depending on the region considered. By changing the lowest boundary value of the region (z_{min}) and keeping the end boundary the same (the top of the peak), we follow how the α parameter from Eq. 4.1 behaves and how it reflects on the value of the perpendicular self-diffusion, $D_\perp$ (Fig. 4.3). The expression to calculate α is once again shown in Eq. 4.2. The value of α was obtained considering the perpendicular self-diffusion coefficient constant within the layer [0,L], and its full derivation can be found in the original work (Franco et al., 2016b).

$$\alpha^{-1} = 4\omega L \frac{(e^{\omega L}+1)}{(e^{\omega L}-1)} \sum_{j=0}^{+\infty} \left[(2j+1)^4\pi^4 + \frac{3\omega^2 L^2}{4}(2j+1)^2\pi^2 - \frac{\omega^4 L^4}{4} \right]^{-1} \tag{4.2}$$

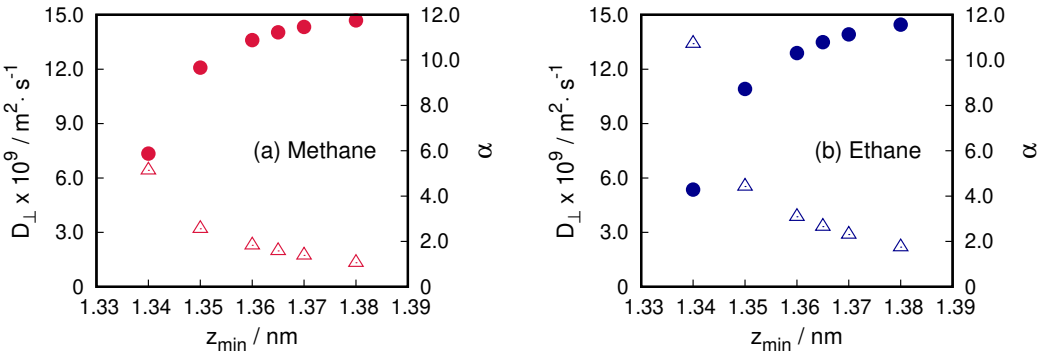

Figure 4.3: Impact of the initial boundary value of the region Ω on the calculation of the perpendicular self-diffusion: triangles (△) for $D_\perp$ and filled circles (●) for α. The values were calculated for pure components confined within calcite slit pores of 3.5 nm at 375 K.

As we increase the lower boundary value for the layer, the value of α gets closer to 12. As it has been proven in the original article (Franco et al., 2016b), $\alpha = 12$ for homogeneous systems, *i. e.*, systems with a constant density profile within the selected layer. Depending on the chosen lower value for the boundary, we have a different $D_{\perp}$. This is a direct consequence of the layer average density: for higher densities, we get lower diffusion coefficients, as can be seen on Table 4.1. As we increase the value of $z_{\min}$, the average density of the selected layer increases, and hence the perpendicular self-diffusion coefficient decreases. Nevertheless, despite the observed variations, by choosing the same $z_{\min}$ for the parallel and perpendicular components, it is still possible to see the anisotropy between $D_{||}$ and $D_{\perp}$, with the latter always having a smaller magnitude, which validates our previous results and conclusions.

Table 4.1: Perpendicular self-diffusion dependency on layer size and density.

	$z_{\min}$ (nm)	L^2 (nm^2)	ω (nm^-1)	ρ ($kg{\cdot}m^{-3}$)	$D_{\perp} \times 10^9$ ($m^2{\cdot}s^{-1}$)
Methane	1.340	0.0110	48.275	386.13	6.42
	1.350	0.0090	38.363	442.34	3.20
	1.360	0.0072	32.633	487.36	2.29
	1.365	0.0064	30.003	512.07	1.98
	1.370	0.0056	27.517	538.11	1.73
	1.380	0.0042	22.754	593.24	1.33
Ethane	1.340	0.0139	46.301	439.79	13.41
	1.350	0.0117	38.009	498.38	5.53
	1.360	0.0096	33.092	545.08	3.86
	1.365	0.0086	30.753	570.83	3.32
	1.370	0.0077	28.514	598.14	2.88
	1.380	0.0061	24.226	656.83	2.19

4.3 Profile throughout the pore

The presence of the walls influence fluid properties, and we have shown in Chapter 3 that different regions of the pore have different self-diffusion coefficients. A more thorough analysis of the values for the self-diffusion coefficient inside a calcite slit pore 3.5 nm wide can be found on Fig. 4.4 for pure components and on Fig. 4.5 for each component of their equimolar binary mixture.

For this calculation, the first half of the pore was divided into five layers - the other half is symmetrical. The first three layers contained density peaks, the fourth was between the

last density peak and the center of the pore, which was the fifth region. The values chosen for our systems are on Table 4.2, remembering that for the perpendicular component only the linear density region inside each layer was considered.

Table 4.2: Values of z (nm) used to determine the layer for the calculation of the self-diffusion tensor.

Layer	**Methane**		**Ethane**	
	z_{min}	z_{max}	z_{min}	z_{max}
1	1.35	1.65	1.35	1.70
2	1.65	2.10	1.70	2.12
3	2.10	2.45	2.12	2.45
4	2.45	2.75	2.45	2.75
5	2.75	3.25	2.75	3.25

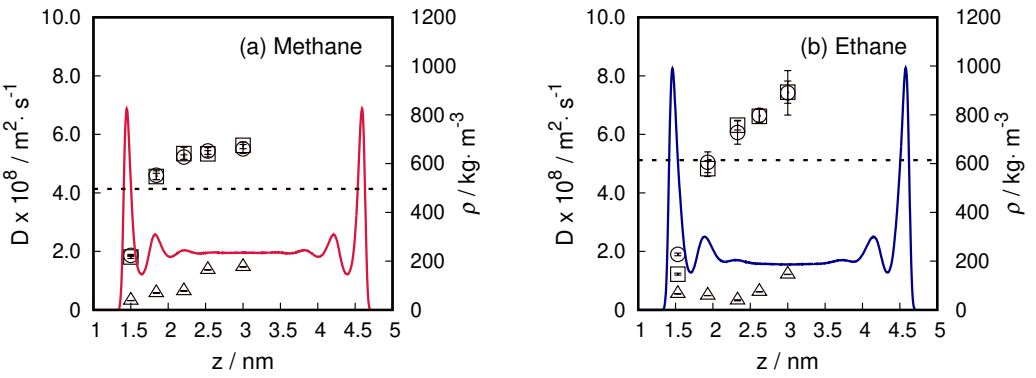

Figure 4.4: Evolution of the self-diffusion components throughout the pore for pure methane and ethane at 250 kg·m^{-3} and 375 K. Squares (□) for D_{XX}, circles (○) for D_{YY}, and triangles (△) for $D_{\perp}$. Dashed line for bulk value uncorrected for finite-size effects.

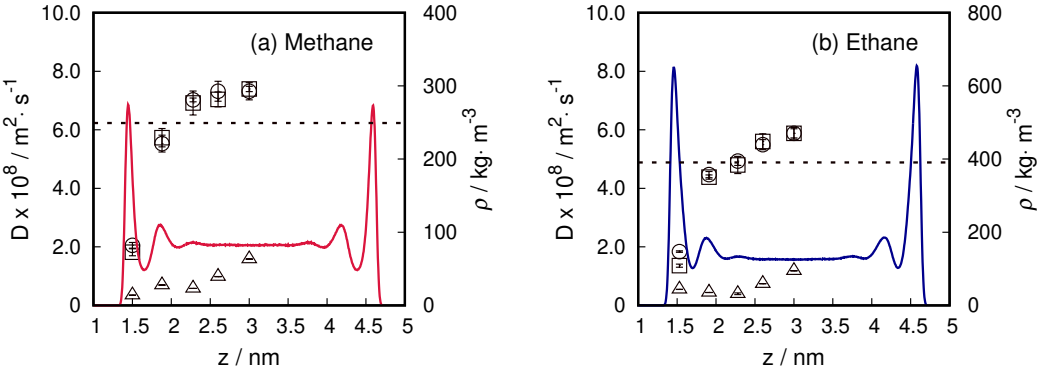

Figure 4.5: Evolution of the self-diffusion components throughout the pore for methane and ethane in a equimolar binary mixture with global density of 250 kg·m^{-3} at 375 K. Squares (□) for D_{XX}, circles (○) for D_{YY}, and triangles (△) for $D_{\perp}$. Dashed line for the bulk value uncorrected for finite-size effects.

The anisotropy between parallel components (D_{XX} and D_{YY}) observed near the walls vanishes the farther the fluid is from the surface. To clearly see the difference near the walls for methane, the reader is referred to Fig. 3.4a, once the broad scale required to include the values at the center of the pore on Fig. 4.5 may not allow to see this information on detail. The confinement effect, however, still causes a difference between the parallel and perpendicular components.

There is an increase on the self-diffusion values towards the central region of the pore, with the trace divided by three approaching the value for the unconfined fluid (dashed line). We calculated the self-diffusion of bulk fluids using Einstein's method (mean square displacement) and did not apply finite-size effects corrections.

4.4 Pore size

To further assess the self-diffusion behavior, we now look at slit pores with different distance between the surfaces. Simonnin et al. (2017) reported that slit pores with a width/height ratio greater than 2.8 present considerable finite-size effects. Following their suggestion, and based on the xy width of our calcite crystal, we considered pore sizes from 3.5 up to 12.5 nm.

The layer chosen was equivalent to 15% of the pore size, centered at the center of the pore. The results for each component of the equimolar binary mixture are shown in Fig. 4.6. The effect of confinement decreases as the pore size increases, but locally there is still an anisotropy between parallel and perpendicular components. Nevertheless, the trace of self-diffusion tensor divided by three is close to the value calculated through Einstein's method for the unconfined fluid.

If instead of considering such a narrow layer to evaluate the local diffusion, we consider the whole region where the density is constant (ρ_{const}), the perpendicular component behaves differently: the confinement effect is smaller and the tensor trace divided by three is closer to bulk values calculated from mean square displacement and corrected for finite-size effects.

Table 4.3 summarizes the regions chosen for each pore and gives an overview of the average local density at each layer, calculated as shown in Eq. 4.3.

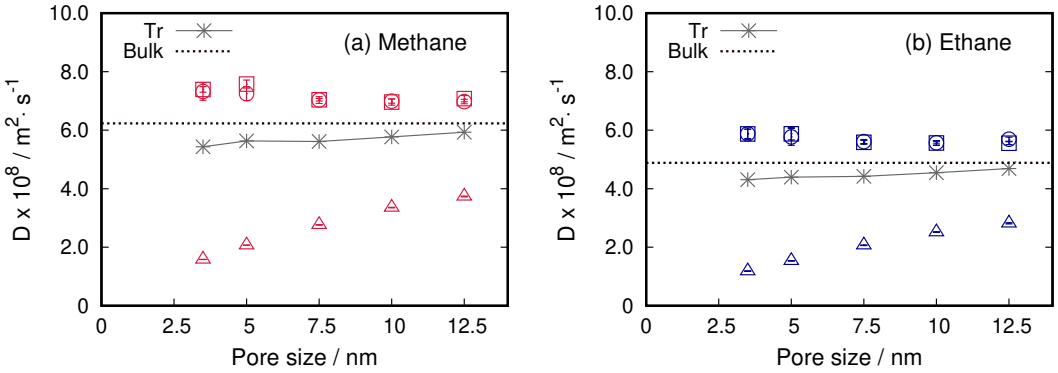

Figure 4.6: Self-diffusion coefficient calculated at the center of the pore for different pore sizes. Squares (□) for D_{XX}, circles (○) for D_{YY}, triangles (△) for $D_{\perp}$, and stars (∗) for the trace of the diffusion tensor divided by three. Dashed line for the bulk value uncorrected for finite-size effects.

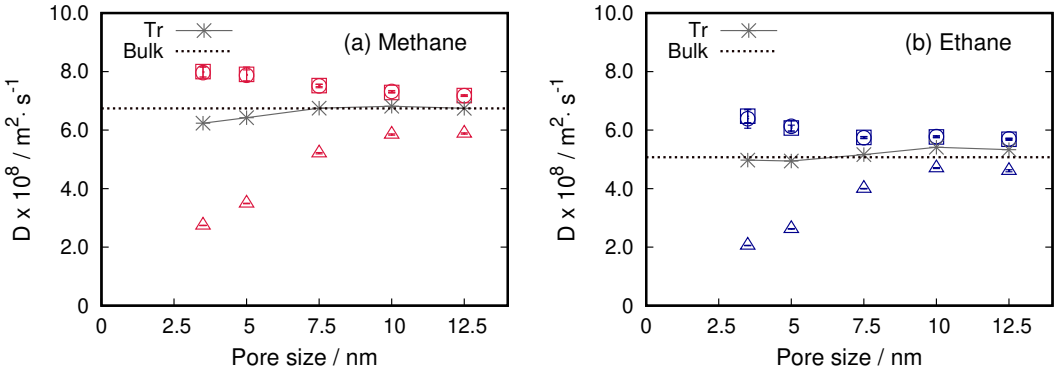

Figure 4.7: Self-diffusion coefficient calculated for the central region at a constant density for different pore sizes. Squares (□) for D_{XX}, circles (○) for D_{YY}, triangles (△) for $D_{\perp}$, and stars (∗) for the trace of the diffusion tensor divided by three. Dashed line for the bulk value corrected for finite-size effects.

$$\text{molecules/nm} = \frac{(\text{methane molecules} + \text{ethane molecules})_{\text{layer}}}{z_{\max} - z_{\min}} \tag{4.3}$$

Table 4.3: Values of z (nm) and average density of the layer for the calculation of the self-diffusion tensor at the center of the pore.

Pore size (nm)	15% (Fig. 4.6)			ρ_{const} (Fig. 4.7)		
	$z_{\min}$	$z_{\max}$	molecules/nm	$z_{\min}$	$z_{\max}$	molecules/nm
3.5	2.75	3.25	134	2.50	3.50	114
5.0	3.35	4.05	141	3.00	4.50	142
7.5	4.46	5.53	149	3.00	7.00	148
10.0	5.45	6.95	152	3.00	9.00	152
12.5	6.56	8.44	153	3.00	11.00	153

From the results shown on Fig. 7, one may conjecture that, to calculate the components of the self-diffusion tensor for the central region of the pore with a constant density, a simpler approach would be to calculate the self-diffusion for the unconfined system (bulk), and subtract the parallel components from there. Once the trace of the diffusion tensor divided by three is comparable to the bulk value, and the parallel components D_{XX} and D_{YY} have the same value, the following expression could give the perpendicular component:

$$D_{\perp} = 3 \times D_{\mathrm{bulk}} - 2 \times D_{||} \tag{4.4}$$

where $D_{||}$ could be D_{XX} or D_{YY}, calculated with the method proposed by Liu et al. (2004) using the survival probability.

The values obtained using Eq. 4.4 gave better predictions for the cases where the trace divided by three was closer to the calculated bulk self-diffusion: for the systems considered here, pores larger than 7.5 nm for methane and smaller than 7.5 nm for ethane (see Fig. 4.7). Nevertheless, this approach could be a valuable way to evaluate the confinement effect at the central region of the pore by assessing the difference between parallel and perpendicular self-diffusion.

The content of this chapter was reprinted with adaptations from Spera, M. B. M and Franco, L. F. M. ***The effect of thermal gradients on adsorption.*** *Fuel. 295, 120553 (2021). https://doi.org/10.1016/j.fuel.2021.120553*

5

The effects of thermal gradients on adsorption

Molecular simulations of confined hydrocarbons have significantly contributed to advances in the study of energy systems, such as natural gas, to reduce environmental impacts and green-house gas emissions. Adsorption and structural properties of confined media impact all production steps from gas recovery to its storage. To understand the possible changes on adsorption behavior caused by the geothermal gradient to which the tight hydrocarbon reservoirs are subjected, we apply non-equilibrium molecular dynamics to simulate methane, n-pentane, and their binary mixture confined between calcite nanopores. We impose a temperature gradient perpendicular to the surface by using the calcite crystals as thermal walls to emulate the geothermal gradient. Surface-fluid interactions are modified by the presence of the gradient, and the adsorption behavior unexpectedly differs from the one at local temperature isothermal conditions. We, therefore, show by means of molecular dynamics simulations that the density profile is not only dependent on temperature, but it also depends on the local temperature gradient. We also calculate the orientation of n-pentane molecules inside the pore, and report its capillary condensation at subcritical

conditions in a dual-pore simulation. We expect these results to improve the knowledge of the coupling between confinement and thermal gradients.

5.1 Introduction

Energy resources that reduces carbon emissions and environmental impacts have an increasing demand (Sunny et al., 2020). Confined hydrocarbons such as natural gas emerged as a bridge to start reducing environmental impacts (Bhattacharjee et al., 2020; Wang et al., 2019). The journey towards an efficient and economically viable production requires investments in research and technologies that allow a deeper knowledge of the system for optimal production and processes design.

Molecular simulations contribute to technical and scientific advances for the understanding of geological characteristics of unconventional reservoir as well as thermophysical and transport properties of the fluid confined within these complex and heterogeneous systems (Striolo and Cole, 2017; Zheng et al., 2019; Dysthe et al., 2002; Collell et al., 2015; Jin and Firoozabadi, 2015; Sharma et al., 2015; Mosher et al., 2013; Yuan et al., 2015). Knowledge of properties such as the adsorption behavior and the fluid structure inside the pore are important to the performance of recovery, purification, transport, and storage of confined hydrocarbons (Li et al., 2017; Wang et al., 2015; Song et al., 2020; Severson and Snurr, 2007; Zhang et al., 2021a; Yu et al., 2020; Herdes et al., 2018).

The study of lighter hydrocarbons is of great interest in this scenario. Methane is the main constituent of natural gas (Trusler and Zarari, 1992; Ansari et al., 2020; Du et al., 2021), and also an important component for sustainable energy as a precursor of hydrogen production, and as part of carbon capture and storage processes (Luo et al., 2014; Bui et al., 2018). Wu et al. (2017) simulated methane-ethane confined mixtures inside a single nanopore connected to a gas bath to evaluate adsorption isotherms and gas recovery. Their results indicate that surface adsorption contributes significantly to the fluid storage within the pores. Higher hydrocarbons are also present in natural gas and are important for other fuel sources. Pentane, for example, is a component of liquefied petroleum gas, besides being used as a working fluid for geothermal power plants (Scholz et al., 2020). Dong et al. (2016) have evaluated the phase equilibria of confined methane, n-butane, n-pentane, and n-hexane and have shown how the phase behavior of confined

fluids is influenced by the adsoption profile and by shifts of the critical properties due to confinement, affecting gas/oil ratio.

One of the main constituents of several unconventional reservoirs are carbonate rocks (Addari and Satta, 2015; Littke et al., 1988; Rexer et al., 2014). Calcite is their most stable polymorph, and studies have shown that structural, dynamical, and electrochemical properties of fluids behave differently when confined within this mineral (Zhang et al., 2021b; Zhao et al., 2019; Koleini et al., 2018; Fazelabdolabadi and Alizadeh-Mojarad, 2017; Chen et al., 2015a; Brasili et al., 2019; Ali et al., 2020; Santos et al., 2019; Zhao et al., 2020). There is an anisotropy between the components of the self-diffusion tensor for pure fluids and mixtures (Franco et al., 2016a; Bui et al., 2017; Spera and Franco, 2020), wettability changes (Silvestri et al., 2019; Al-Anssari et al., 2018; Mohammed and Gadikota, 2020), and structural properties such as the adsorption profile and conformation of the molecules are influenced by the calcite walls (Santos et al., 2018; Mohammed and Gadikota, 2019a,b).

Considering that the geological system is subjected to a geothermal gradient (Montel et al., 2007), evaluating oil and gas reservoirs under non-equilibrium conditions is necessary to better understand its behavior and obtain optimal production with minimal environmental impact. Non-equilibrium molecular dynamics (NEMD) have been used to simulate systems with a pressure gradient to evaluate the effect of mass flow under confinement (Wang et al., 2016), and the transport through membranes (Chen et al., 2017; Muscatello et al., 2016). Here, we apply NEMD to simulate methane, *n*-pentane, and their binary mixture and see the effect a thermal gradient on the systems confined between calcite parallel walls. Aware of the importance of fluid-solid interfaces for the properties of confined fluids (Krishnan et al., 2016; Huang et al., 2019; Bhowmik et al., 2017), we report some counter-intuitive adsorption behavior on the presence of a temperature gradient and the effect it has on the arrangement of *n*-pentane molecules close to the crystal walls. From these results, we may conjecture that the density profile within the pore depends on both the temperature and the local temperature gradient. This information can improve the description of initial reservoir conditions and gas/oil ratio, for example, leading to more accurate production forecasts and more reliable reservoir simulations.

5.2 Simulation details

Methane and n-pentane were confined within a slit pore of calcite, with calcite $\{10\bar{1}4\}$ plane orthogonal to the z direction. Calcite xyz dimensions were 4.990 nm x 4.856 nm x 1.212 nm, and the pore size was fixed as $H = 3.5$ nm along the z axis. The overall density of the simulated systems were close to sorbed shale gas density (Aguilera, 2016). Details are described in Table 5.1.

Table 5.1: Density (ρ), number of molecules (N), and total number of united-atoms (UA_{TOT}) of each simulated system.

	ρ / kg·m^{-3}	N_{MET}	N_{PENT}	N_{TOT}	UA_{TOT}	ρ / UA·nm^{-3}
Methane	344	1095	0	1095	1095	12.9
	562	1790	0	1790	1790	21.1
***n*-Pentane**	344	0	243	243	1215	14.3
	562	0	398	398	1990	23.5
Mixture	562	326	326	652	1956	23.1

Molecular dynamics (MD) simulations were performed with GROMACS 5.0.2 (Abraham et al., 2015) using the Leap-Frog algorithm with a time step of 2 fs. We applied TraPPE force field (Martin and Siepmann, 1998) to hydrocarbons and Xiao et al. (2011) force field to the calcite crystal, with a cutoff radius of 1.0 nm. Fluid-wall interactions parameters were calculated using geometrical combining rules. Particle Mesh Ewald method (Darden et al., 1993) was used to calculate the electrostatic interactions and a velocity-rescale thermostat (Bussi et al., 2007) was applied to control the temperature of the system, with relaxation time $\tau_{\mathrm{T}} = 1.0$ ps. Positions and velocities were stored every 0.2 ps. Periodic boundary conditions were applied at all directions, with no tail corrections due to the inhomogeneity of the systems (Franco et al., 2016b; Allen and Tildesley, 2017).

Isothermal systems were simulated with equilibrium molecular dynamics (EMD) in the NVT ensemble with 20 ns of equilibration and 50 ns of production time. Non-isothermal systems were simulated with boundary-driven non-equilibrium molecular dynamics (BD-NEMD) (Artola and Rousseau, 2013; Hafskjold, 2017), with calcite acting as thermal walls creating a temperature gradient perpendicular to the interface. The systems were equilibrated in the NVT ensemble at 375 K for 20 ns, a common temperature in oil/gas reservoirs (Franco et al., 2016a; Santos et al., 2018). Then, we applied different temperatures to the calcite walls: 425 K (*hot* side) and 325 K (*cold* side), imposing a huge temperature gradient. A typical value for the geothermal gradient is around 0.03 K/m

(Montel et al., 2007), but it is a common practice when simulating non-equilibrium systems to impose a much larger gradient to amplify the fluctuations and gain molecular and statistical insight (Galliero et al., 2017; Xu et al., 2006). Although our simulated system had a temperature gradient of 10^{10} K/m, it is still in the linear response regime regarding the heat flux (Kjelstrup et al., 2008).

The fluid thermostat was turned off allowing the temperature gradient to establish during 50 ns of equilibration, followed by 50 ns of production time. The temperature profile was obtained along the z direction by splitting the simulation box into 100 slabs, and calculating the average local temperature from the kinetic energy of the particles inside each slab. To apply periodic boundary conditions at all directions, we created a dual-pore simulation box avoiding contact between the *hot* and *cold* walls, as shown in Figure 5.1.

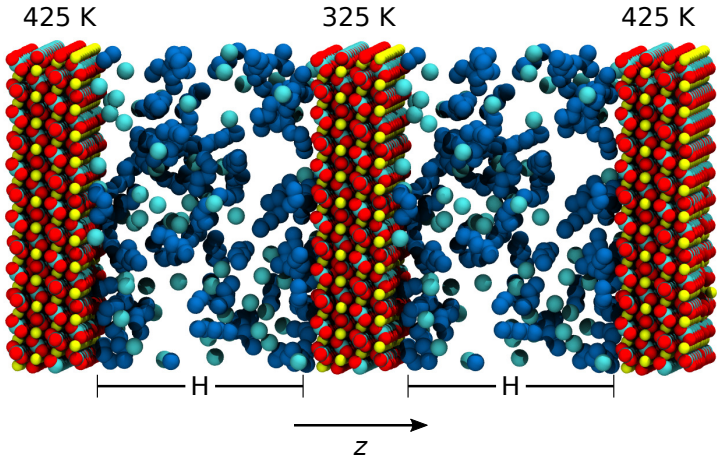

Figure 5.1: Initial configuration: methane (cyan) - *n*-pentane (dark blue) mixture confined within a calcite slit pore using a dual-pore simulation box.

5.3 Results and discussion

5.3.1 Adsorption profile

Confined fluids have marked adsorption peaks near the walls due to surface-fluid attractive interactions (Gelb et al., 1999; Franco, 2019). Density profiles were obtained from the first pore of the simulation box (left - Figure 5.1). The second pore is completely symmetric, and hence its profiles are omitted here.

Figure 5.2 shows the density distribution of methane confined with an overall density

of $\rho = 562$ kg·m^{-3}. The isothermal behavior, represented by the dashed lines, illustrates the temperature dependence of the adsorption near the walls and the fluid distribution throughout the pore. Highlighted, the peaks near the calcite walls show the counter-intuitive behavior after a temperature gradient was applied (filled line): closer to the *hot* wall, the average temperature of the fluid is near 400 K, but the adsorption peak corresponds to the one at 425 K. Closer to the *cold* wall, at a temperature around 350 K, the adsorption peak corresponds to the expected one between 325 K and 375 K.

n-Pentane had a similar behavior at the *cold* side but an even more pronounced effect at the *hot* side, with an adsorption peak at 400 K smaller than at 425 K (Figure 5.3). The high molar density of methane could have compensated the thermal gradient effect on the adsorption resulting in a less pronounced difference. Although having the same overall mass density, the number of molecules were different between methane and *n*-pentane (Table 5.1).

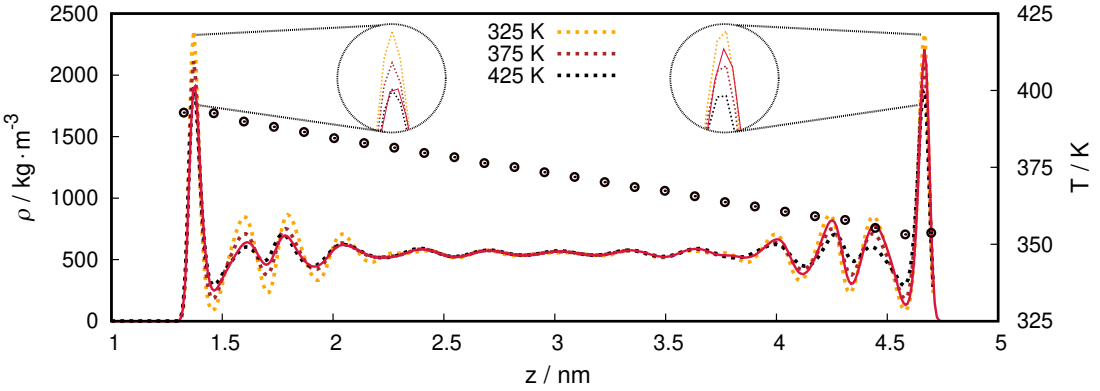

Figure 5.2: Density profile of pure methane ($\rho = 562$ kg·m^{-3}) at the isothermal condition (dashed lines) and after a temperature gradient was applied (red line). Black dots for the average temperature of each slab of the pore, displayed on the right axis.

The standard deviation of the temperature was around 1 K, while the density profiles are averages from the entire production run (50 ns). With these results, we may conjecture that the density profile, $\rho(z)$, depends not only on the temperature, but also on the local thermal gradient. Therefore, at non-equilibrium conditions, one may write that:

$$\rho = \rho(z, T, \nabla T) \tag{5.1}$$

where ∇T is the temperature gradient.

Although the temperature gradient is still in the linear regime regarding the heat flux, the additional perturbation caused by the presence of the walls could affect the

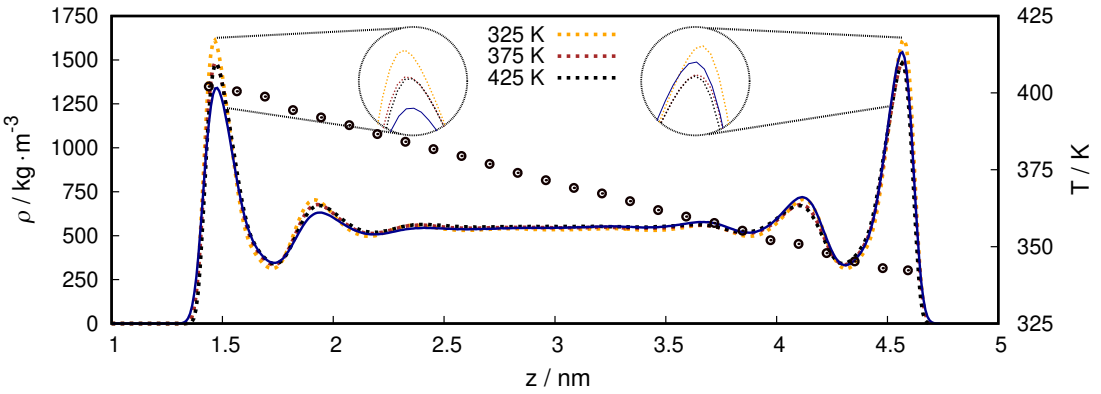

Figure 5.3: Density profile of pure n-pentane ($\rho = 562$ kg·m^{-3}) at the isothermal condition (dashed lines) and after a temperature gradient was applied (blue line). Black dots for the average temperature of each slab of the pore, displayed on the right axis.

linear response - and that could be reflected on the adsorption behavior observed. An investigation of the chemical potential within the pore, applying the test particle method from Widom (1963) for example, could give an insight on the system's thermodynamic state. Nevertheless, for dense systems such as the ones studied here with high adsorbed density peaks close to the walls, the insertion of particles requires more robust algorithms lest the statistics on the estimation of the chemical potential is compromised (Allen and Tildesley, 2017). This topic certainly requires further investigation.

To assess the mixture behavior, we simulated an equimolar methane-n-pentane binary mixture with the same mass density as the pure components ($\rho = 562$ kg·m^{-3}). We obtained a similar adsorption profile, with the counter-intuitive effect present on the *hot* side, but absent on the *cold* side (Figure 5.4). This could be due to the preference of the compounds to accumulate on the colder region, as it is observed in thermal diffusion calculation. We discuss this topic further on Chapter 6.

5.3.2 Structural parameters

From the density profiles at isothermal conditions, one can see that an increase in the temperature diminishes the layer definitions throughout the pore (noticeable in Figure 5.2). Higher temperatures allow molecules to distribute more freely, as shown by Severson and Snurr (2007). To further evaluate fluid arrangement and the thermal effect on its structure, we calculated the order parameter for n-pentane molecules using Equation 5.2

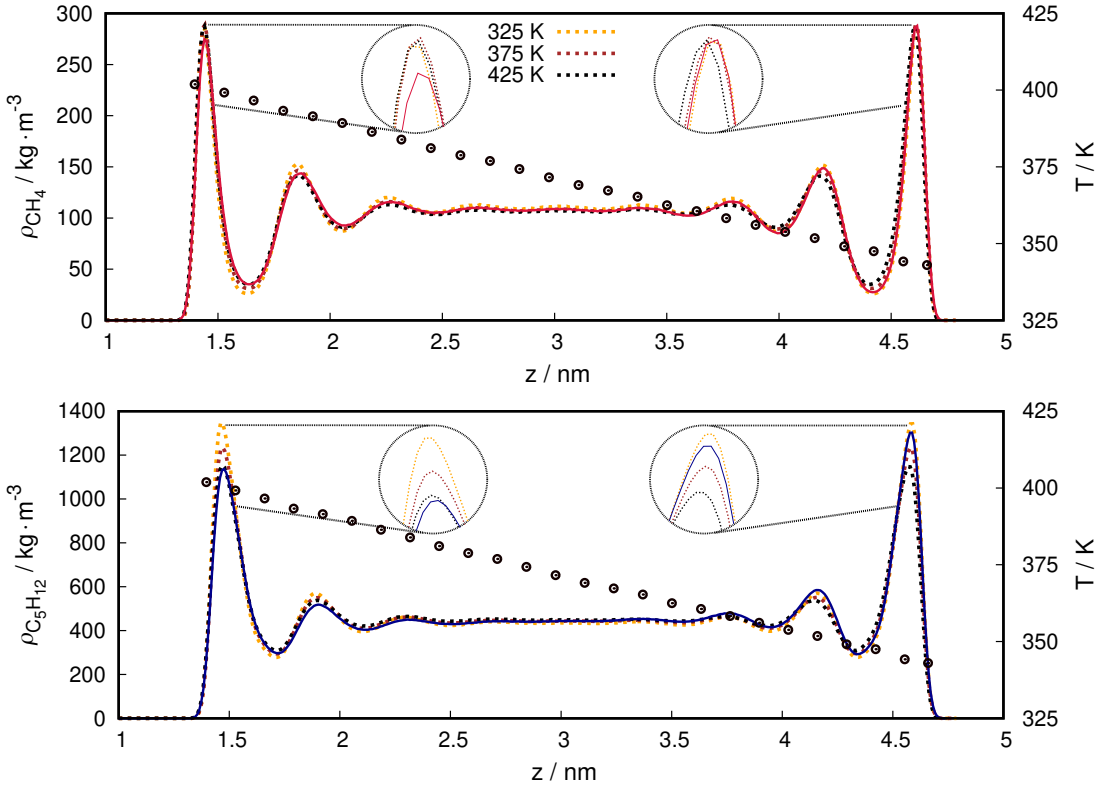

Figure 5.4: Density profile of methane (red) and n-pentane (blue) in a equimolar mixture with $\rho = 562$ kg·m^{-3} at the isothermal condition (dashed lines) and after a temperature gradient was applied (filled lines). Black dots for the average temperature of each slab of the pore, displayed on the right axis.

(Severson and Snurr, 2007).

$$S = \frac{3\langle \cos^2 \alpha \rangle - 1}{2} \tag{5.2}$$

where $S = 1$ means that all molecules are perpendicular to the wall, $S = -0.5$ means they are parallel to the walls, $S = 0$ means that there is no preferential orientation, and α is the angle between the end-to-end vector of n-pentane and the z axis (which is orthogonal to the crystal surface).

In more populated regions, n-pentane has a parallel orientation to the walls (Figure 5.5). This is expected due to fluid-wall interactions, and explains why more molecules could be on that area, since lying flat on the surface allows a higher packing. The next layer has a more perpendicular tendency, with values near 0.3 for the order parameter. Another peak with parallel preferential orientation appears on the adjacent layer, following the inverse of the density profile. The layers decrease in density and order by distancing the walls, until molecules become randomly oriented at the center of the pore, with $S \approx 0$.

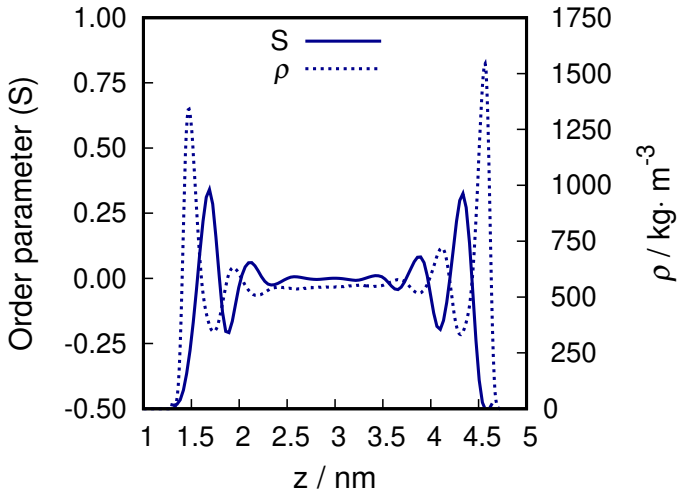

Figure 5.5: Order parameter (Eq. 5.2) and density profile of pure n-pentane confined within a calcite slit pore in the presence of a temperature gradient. Filled line for order parameter (left axis) and dashed line for density profile (right axis).

Layering and ordering of molecules are important for properties such as viscosity and diffusion of the fluid, and can used in technical applications such as thermal processes for improving oil and gas recovery (Wang et al., 2015, 2016; Diaz et al., 2017). A temperature gradient would make the fluid slightly less ordered when compared to the isothermal condition, as seen in Figure 5.6. The orientation of n-pentane molecules in the binary mixture was similar to pure n-pentane.

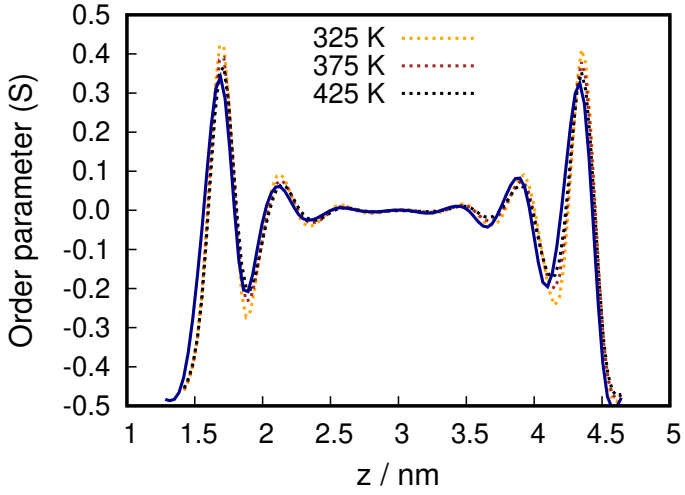

Figure 5.6: Order parameter (Eq. 5.2) of pure n-pentane confined within a calcite slit pore. Filled line for results after a temperature gradient was applied and dashed lines for isothermal conditions.

5.3.3 Pore filling

The effect of the overall density and number of particles can be analyzed by simulating the same systems with a lower mass density to check if the crowded pore undertook the thermal effect. Methane was simulated at $\rho = 344$ kg·m^{-3} and the results on Figure 5.7 show that for a less populated pore, the effect on the *hot* side was indeed more pronounced, with the adsorption peak at 400 K smaller than the isothermal peak at 425 K.

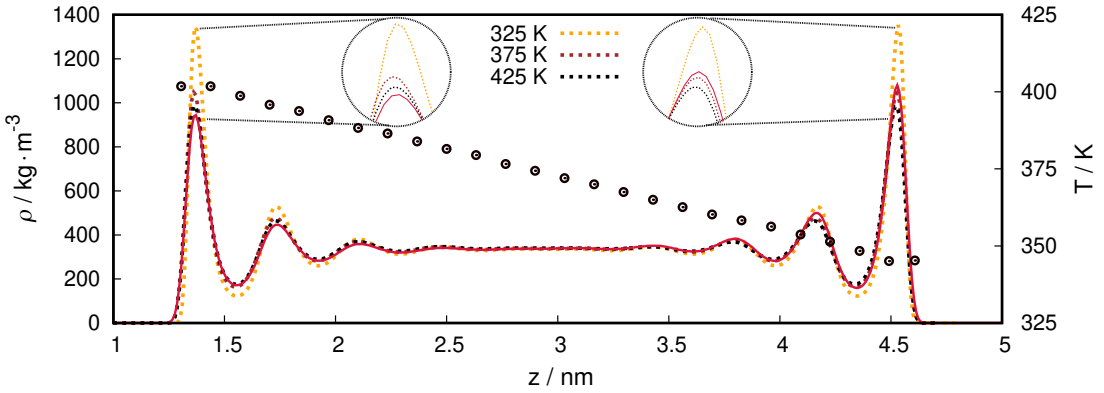

Figure 5.7: Density profile of pure methane ($\rho = 344$ kg·m^{-3}) at the isothermal condition (dashed lines) and after a temperature gradient was applied (red line). Black dots for the average temperature at each slab, displayed on the right axis.

Capillary condensation

n-Pentane was also isothermally simulated at a lower density, but the conditions imposed to the system were subcritical for pentane, and hence a different behavior at each side of the dual-pore was observed (Figure 5.8).

At the very beginning of the simulation, the system collapses into a configuration where one side has an overall density closer to bulk liquid phase, which is 535 kg·m^{-3} according to NIST (Linstrom and W.G. Mallard, 2018), and the other side closer to the vapor phase density, which is 16.9 kg·m^{-3} according to NIST (Linstrom and W.G. Mallard, 2018) - see Figure 5.9. Similar curves were obtained at 325 K, 375 K, and for non-equilibrium conditions. The calcite wall in the middle acted as a piston for the system to adjust its pore volumes, indicating that under specific conditions we could have capillary condensation inside heterogeneous nanopores, with systems with different phase behavior and properties in equilibrium with each other. At 425 K, a less defined density profile was observed that could indicate conditions close to a critical point.

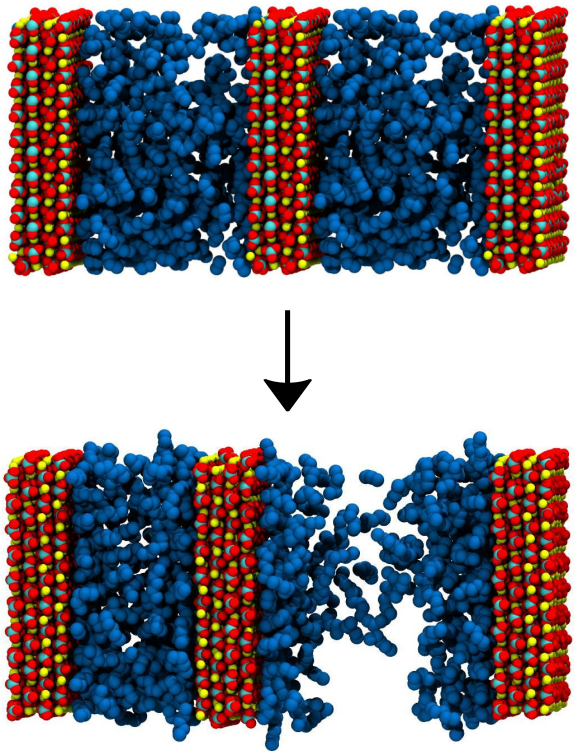

Figure 5.8: Pure n-pentane confined inside calcite slit pore with density $\rho = 344$ kg·m^{-3}. Initial (top) and final (bottom) configuration after isothermal simulation at 375 K.

This means that, in principle, we could determine the phase equilibria for confined systems via molecular dynamics simulations using more complex and realistic configurations for the confining walls. Phase behavior of fluids confined inside tight pores differ from bulk, with changes in critical temperature and critical density (Barsotti et al., 2016, 2018, 2020; Salahshoor et al., 2018; Gao et al., 2018; Liu and Zhang, 2019; Li et al., 2020). Confinement effects play an important role and are dependent on pore size (Sedghi and Piri, 2018). Jin et al. (2017) simulated the behavior of methane inside multiple cylindrical pores using gauge-GCMC (Jin and Nasrabadi, 2016). When simulating pores with multiple sizes, the phase behavior was uncorrelated with pore size: a double-pore of sizes 4 nm / 10 nm showed essentially the same phase envelope that a single 8 nm pore.

In the canonical ensemble, in which we fix number of particles, temperature, and volume, only the total volume of the dual-pore system is controlled, so the calcite crystal, initially at the center of the dual-pore simulation box, is allowed to move, and the final size of each pore differs at different isothermal subcritical runs. Therefore, it seems very impractical to pursue a route to determine the phase envelope applying molecular dynamics simulations for these systems, although it is interesting to see that the capillary

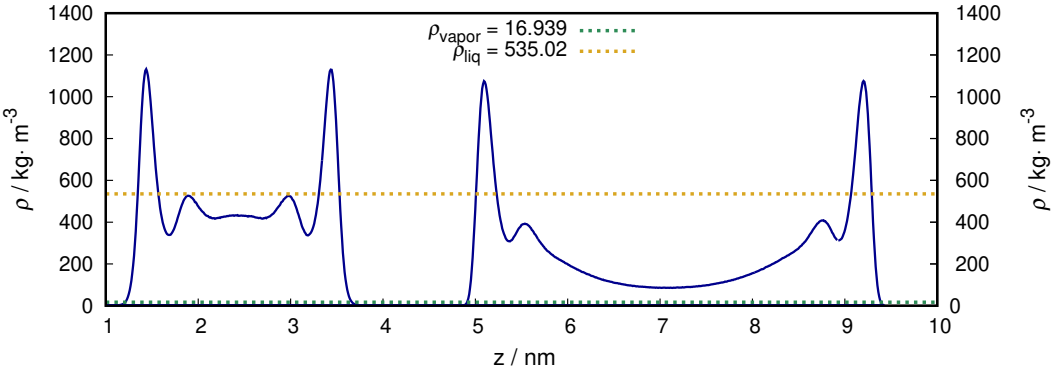

Figure 5.9: Density profile of pure n-pentane (ρ = 344 kg·m^{-3}) at 375 K (isothermal). Dashed lines indicate NIST (Linstrom and W.G. Mallard, 2018) values of vapor and liquid density for bulk n-pentane a 375 K (vapor-liquid equilibrium).

condensation can be directly observed with molecular dynamics simulations, as a phase equilibrium between two pores with different densities.

5.4 Conclusion

Adsorption and structural parameters are important for the performance of operations involving confined hydrocarbons. We have simulated methane and n-pentane confined within calcite slit pores subjected to a thermal gradient to evaluate the effect of the non-equilibrium condition on the fluid-wall interaction.

Using the calcite as thermal walls, the temperature gradient was perpendicular to the interface. Near the *hot* side, we observed that even the fluid having a local temperature of $\approx$ 400 K, its behavior did not correspond to the isothermal condition at the same temperature: the adsorption peak was equal or lower than at 425 K. This effect was more pronounced for lower densities, suggesting the highly filled pore was able to compensate the thermal effects. These results suggest a new conjecture: the density profile depends on both the temperature and the temperature gradient. This unexpected result may have a major impact on the calculation of adsorption in non-isothermal reservoirs.

Configuration information for n-pentane systems was provided through the order parameter, which showed a preferential parallel orientation closer to the walls correlated to the density profile. The system was slightly less ordered in the presence of the thermal gradient, for both the pure component and for n-pentane within a binary mixture with methane. The simulated temperature conditions were subcritical for n-pentane, which, at

lower densities, splits into two distinct phases, one at each pore of the dual-pore simulation box. This is a clear manifestation of the capillary condensation phenomenon naturally emerging from molecular dynamics simulations.

Much progress has been made, but properties of confined systems are still an exciting field with several mechanisms not fully understood. The effect of temperature gradients, and its coupling with confinement effect and other transport/phenomenological properties, require further investigations to relate the macroscopic behavior to microscopic features. We hope this work contributes as a step forward in this research field.

6

Thermal diffusion under confinement

To complement the information on the adsorption profile of methane-n-pentane near calcite walls, we determine the self-diffusion tensor from equilibrium molecular dynamics data, and evaluate the Soret coefficient from non-equilibrium molecular dynamics results. For the high density system considered, the self-diffusion at the center of the pore was affected by confinement effects, but the magnitude of the Soret at the central region was the expected one for bulk systems.

6.1 Introduction

A mixture subjected to a temperature gradient will show a relative concentration gradient between the components, which is a coupled phenomenon called thermal diffusion (de Groot and Mazur, 1984; Artola and Rousseau, 2007). This effect is present in a wide range of situations, from the separation of isotopes (Furry et al., 1939) and petroleum industry (Furtado et al., 2015; Simon et al., 1998), to daily examples such as the preference of dust to accumulate near the cold window instead of on the hot radiator (Kjelstrup et al.,

2017).

Regarding the oil and gas industry, thermal diffusion is known to change the distribution of species inside hydrocarbon reservoir, impacting on the precision of reservoir simulation, field plan development, and drainage plans (Galliero et al., 2016; Dysthe et al., 1998; Galliéro et al., 2003). Geological characteristics such as rock composition and porosity, together with Earth's geothermal heat flux, can create temperature gradients from different directions and cause significant effects on species distribution (Esposito et al., 2017; Nasrabadi et al., 2006). A famous example of the extent of the temperature effect is the Yufutsu field in Japan, where due to thermal diffusion and gravitational segregation the heavier compounds are found on top of the light components inside the reservoir (Ghorayeb et al., 2003).

Thermal diffusion has been investigated under confinement applying a temperature gradient parallel to the walls (Galliero et al., 2017; Pourali and Maghari, 2014; Hannaoui et al., 2013; Colombani et al., 2002). It was reported that although the separation effect also occurs under confinement, the effect on the magnitude of thermal diffusion is usually negligible. Galliéro et al. (2006) proposed three main effects that could disturb the thermal diffusion of a confined fluid: the influence of the confining geometry on fluid dynamics; modifications on the thermal field of the liquid due to thermal conductivity of the solid; and changes on the particle distribution caused by selective wall adsorption.

A temperature gradient perpendicular to the confinement will lead to a density profile rearrangement from the thermal effect, but also due to the direct influence of the walls. Colombani et al. (2003) suggested the adsorption phenomena as the leading cause of deviations between the thermal diffusion coefficients in homogenous and inhomogenous media, which indicates that the adsorption behavior should not be overlooked.

To assess the thermal diffusion for our system of hydrocarbons confined within calcite nanopores, we calculate the Soret coefficient for a confined methane-n-pentane mixture from NEMD results, applying a temperature gradient perpendicular to the direction of confinement. The calcite walls act as thermal walls, and the temperature gradient that is established is a result of thermal transfer between the wall and the fluid. We evaluate the central region of the pore as a first approach to see the effect a geothermal gradient would have on such system.

6.2 Simulation details

A methane-n-pentane equimolar mixture confined within a slit pore of calcite was simulated using a dual-pore simulation box to evaluate its thermal diffusion under confinement (Fig. 6.1). The mixture had an overall density of 562 kg·m^{-3}, and the walls were set to $T_{\mathrm{HOT}} = 425$ K and $T_{\mathrm{COLD}} = 325$ K, with a resulting temperature gradient of ≈ 20 K/nm. As previously mentioned, a very large thermal gradient is commonly applied in non-equilibrium molecular simulation and still in the linear response regime (Galliero et al., 2017). Further details about the temperature gradient, simulation procedure, and system configuration can be found in section 5.2. We show the results for the first pore on the left side, since the pore on the right side has a mirrored behavior.

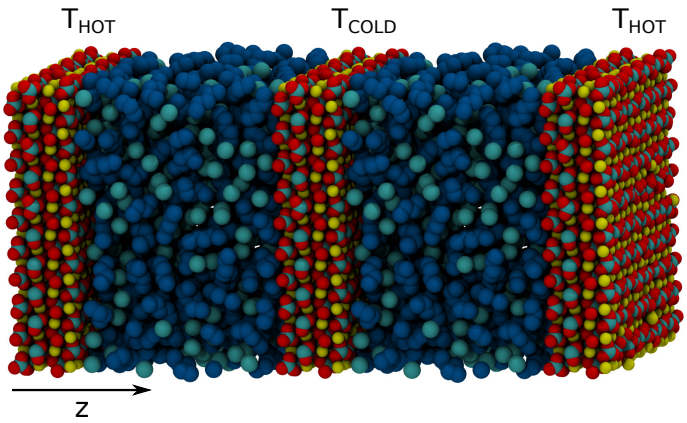

Figure 6.1: Initial configuration of methane-n-pentane mixture within calcite slit pores of 3.5 nm each (at the z direction).

6.3 Self-diffusion

The first transport property of this system to be evaluated is the self-diffusion profile, using the methodology from Liu et al. (2004) and Franco et al. (2016b) to calculate each component of the tensor for the high density regions and at the center of the pore (from 2.5 to 3.5 nm). The result is shown in Fig. 6.2.

The difference between the self-diffusion at the parallel and perpendicular directions is also present for this system at all regions of the pore. The determination of the perpendicular self-diffusion at the high density region of n-pentane was unfeasible because the relaxation time of local density fluctuations is faster than the time required for particles to diffuse, considering the small layer evaluated and the size of the n-pentane molecules.

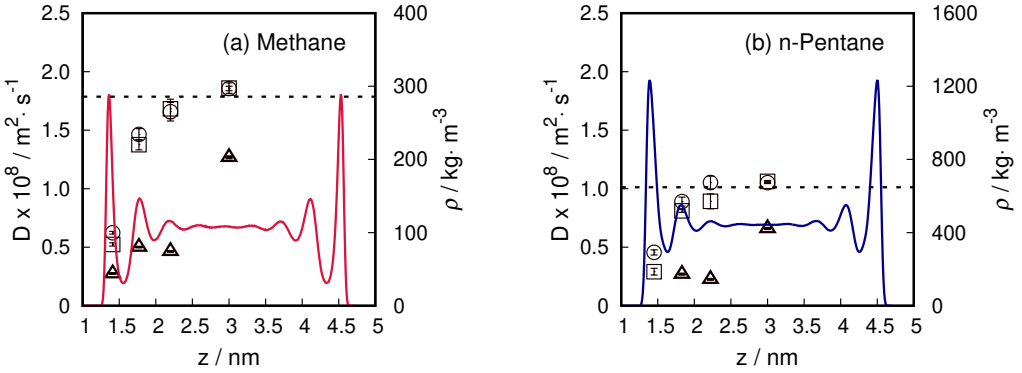

Figure 6.2: Self-diffusion profile for each component of methane-*n*-pentane equimolar mixture confined inside a calcite slit pore at 375 K and 562 kg·m^{-3}. Squares (□) for D_{XX}, circles (○) for D_{YY}, and triangles (△) for $D_{\perp}$. Dashed line for bulk value uncorrected for finite-size effects.

The high density results in anisotropy between the parallel components even for the layers away from the walls. This effect vanishes at the center of the pore, as was previously shown for a methane-ethane mixture (Fig. 4.5). Since the pore is very crowded, a slight oscillating profile still remains at the central region, as can be seen in Fig. 6.3. Nevertheless, the approach we proposed to calculate the perpendicular self-diffusion using Eq. 4.4 would still give reasonable results if applied to the region without high density peaks (here, from 2.5 to 3.5 nm).

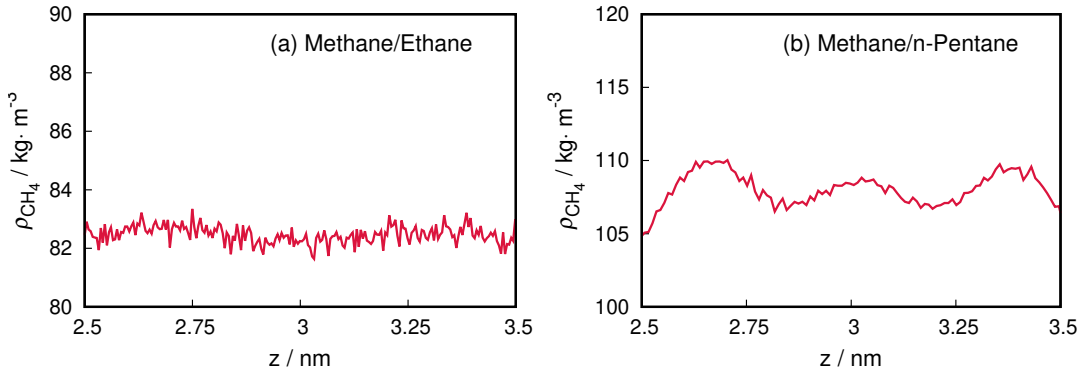

Figure 6.3: Surface effect at the center of the pore: methane density profile for (a) methane-ethane equimolar mixture at a global density of 250 kg·m^{-3} and (b) methane-*n*-pentane equimolar mixture at a global density of 562 kg·m^{-3}. Both mixtures confined inside a calcite slit pore of 3.5 nm wide at 375 K.

6.4 Soret coefficient

Fig. 6.4 shows the total density profile of methane and n-pentane at the isothermal condition. A symmetrical behavior around the center of the pore (at $z \approx 3$ nm) can be clearly seen.

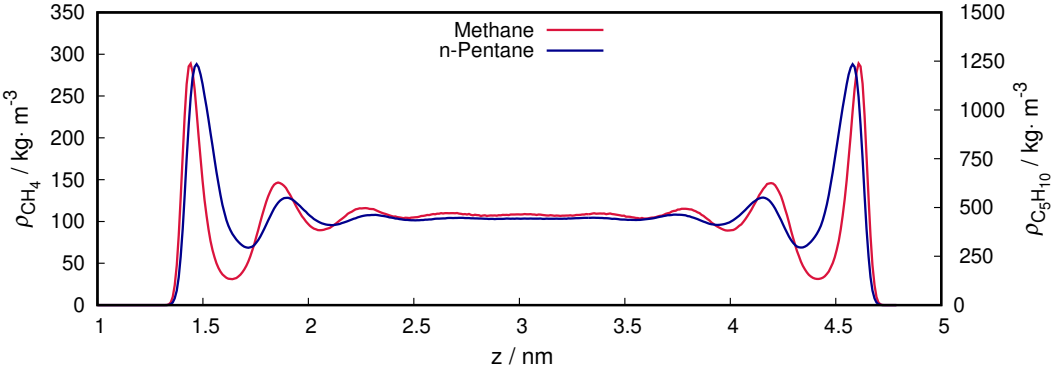

Figure 6.4: Density profile for each component of the confined mixture in a comparative scale. Methane (red) values on the left axis and n-pentane (blue) values on the right axis. Data for 375 K.

Once a temperature gradient is applied on the system, the density profile changes, with a higher n-pentane density near the colder calcite wall (Fig. 6.5). The change on the adsorption near the walls is due to the influence of the local temperature, and we have shown on Chapter 5 that a thermal gradient can affect this behavior.

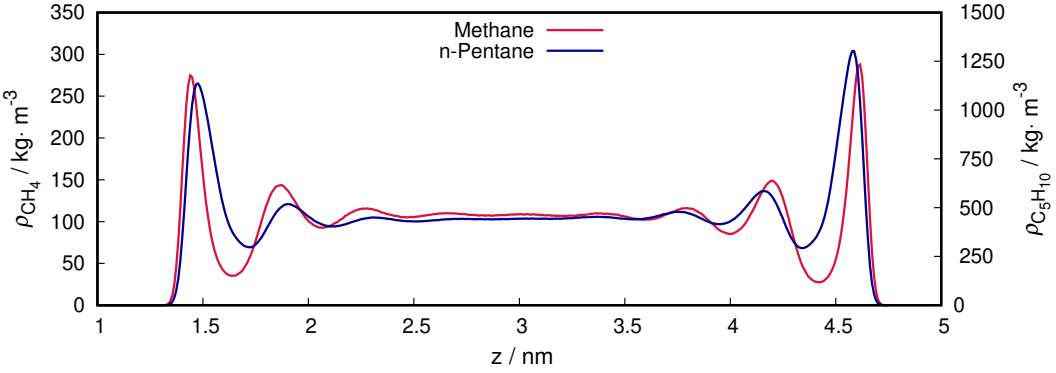

Figure 6.5: Density profile for each component of the confined mixture after a temperature gradient was applied. Methane (red) values on the left axis and n-Pentane (blue) values on the right axis.

From Fig. 6.4 and 6.5 one could conclude that n-pentane shifted to the colder region, since the density peak on the right was higher than for methane. It is also possible to see a slight increase on n-pentane density from the hot to the cold side.

The mole fraction profile of n-pentane (Fig. 6.6) shows that it oscillates throughout the pore, with influence of the walls. The central region (2.5 - 3.5 nm) has a lower effect of the surface, as it was seen for the self-diffusion, so we suggest to evaluate the Soret coefficient at this region to disentangle the effect of confinement from the adsorption behavior.

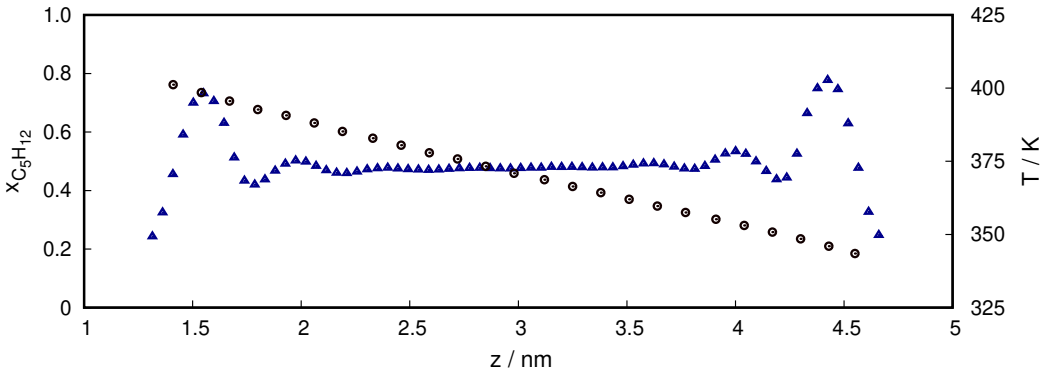

Figure 6.6: n-Pentane mole fraction (blue triangles) for an equimolar binary mixture with methane confined within a calcite pore 3.5 wide. Black circles for the average temperature of each layer inside the pore. Standard deviation for the temperature was ≈ 1 K.

In Fig. 6.7, the mole fractions still oscillates at the center of the pore. This could indicate a reminiscent influence of the walls or higher correlation distance due to the high density, as previously mentioned for the self-diffusion. Nevertheless, calculating the Soret coefficient for this region using the average molar gradient we get:

$$s_T = -\frac{1}{x_\mathrm{A} x_\mathrm{B}} \frac{\nabla x_\mathrm{A}}{\nabla T} = 2.2 \times 10^{-3} \mathrm{K}^{-1} \tag{6.1}$$

with $A = \mathrm{C_5H_{12}}$ and $B = \mathrm{CH_4}$, following the convention where the heaviest component is component A and $s_T > 0$ when the heaviest component enriches on the coldest side (Artola and Rousseau, 2013).

We simulated methane-n-pentane unconfined mixture under the same temperature and density conditions, using BD-NEMD with thermal regions as described in section 2.2.1. The computed Soret coefficient was $(1.7 \pm 0.7) \times 10^{-3}$ K^{-1}. This value can serve as reference, but the comparison with bulk system is not straightforward due to the influence of the walls and the nonuniform particle distribution. From Chapter 5, we could see that, even for pure components, there is a migration of particles to the colder side - affecting the density profile and the symmetry around the center of the pore. Here, we observed

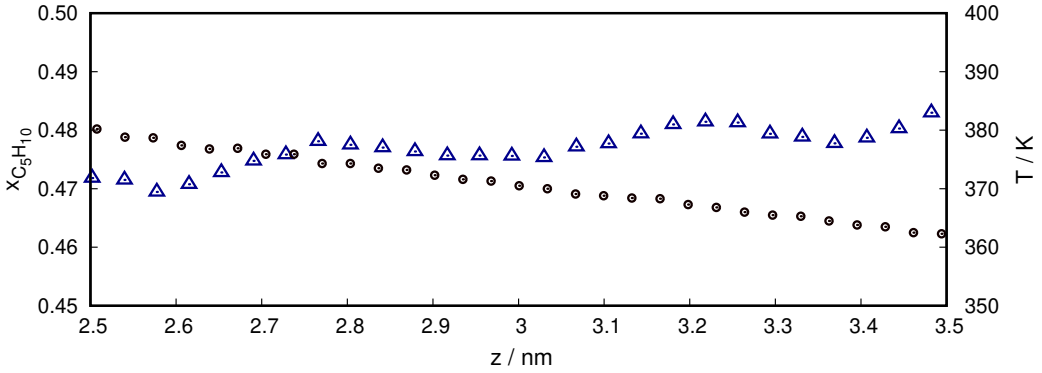

Figure 6.7: Mole fraction of n-pentane on the central region of the pore and temperature profile.

that the density difference between hot and cold sides was greater for n-pentane, creating a mole fraction gradient. This indicates that there is thermal diffusion at the direction of confinement, and could help explain the results from Chapter 5, where the adsorption peak did not correspond to the isothermal condition at the local temperature.

To the moment, however, we are unable to determine the contribution of each effect close to the confining material, and disentangle surface, confinement, and thermal effects to fully explain the observed behavior. Since near the walls adsorption and surface effects add to the confinement effect, we know that applying Eq. 6.1 to the whole pore or to different regions, as it was done for self-diffusion, will not give thermal diffusion measurements. This would require further investigation on thermal transport mechanism under confinement, evaluation of the parameters involved on the simulation of thermal diffusion, and running enough simulations to get a broader sense of errors and standard deviations. Nevertheless, we hope this first assessment helps future investigations on thermal diffusion under confinement.

7 Conclusions

In this work, we studied the diffusion process of hydrocarbon mixtures confined inside calcite slit pores using molecular simulation. The methodology proposed by Franco et al. (2016b) was tested for mixtures, finding that the anisotropy between the components of the self-diffusion tensor previously observed for pure components (Franco et al., 2016a) are still present for mixtures when the fluid is close to the confining material. In fact, heavier components had greater anisotropy for the parallel self-diffusion and their presence in a mixture with methane increased the anisotropy of methane parallel components.

The methodology used to calculate the perpendicular self-diffusion was assessed, and we showed how the choice of parameters can influence the results. With this in mind, it is suggested that the same layer boundary values are considered for the calculation of $D_{||}$ and $D_{\perp}$, to correctly evaluate the results.

At the center of the pore, the difference between the self-diffusion at x and y directions vanishes, and there is only a confinement effect restricting the mobility of particles at the z direction. This confinement effect decreases as the pore size is increased.

For the central region of the pore, there is a "bulk-like" behavior with a more uniform density profile, and we observed that the trace of the self-diffusion tensor remained constant for different pore sizes. This allowed us to propose an alternative method to calculate the perpendicular self-diffusion and determine the presence of a confinement effect: subtract the parallel self-diffusion coefficients from the value calculated for bulk systems.

An interesting case of diffusion is when it is caused by a temperature gradient. To evaluate this phenomenon for hydrocarbons confined within calcite, we used non-equilibrium techniques and applied a thermal gradient to the system perpendicular to the confinement direction. First, the adsorption behavior was studied. A counter-intuitive result suggested that the density profile may also depend on the local temperature gradient, since under non-equilibrium conditions the adsorption peak did not correspond to the expected one at the local temperature.

Finally, the thermal diffusion at the direction of confined was calculated via the Soret coefficient for one hydrocarbon binary mixture, confirming that a concentration gradient is established at the direction of confinement - and hence we have thermal diffusion. Nevertheless, we were only able to estimate it at the center of the pore, since near the walls there is influence of surface interaction and adsorption, and so far we are unsure how to disentangle all effects and calculate the "true" thermal diffusion.

The molecular insight obtained from this work regarding the diffusion of hydrocarbon mixtures within tight pores of calcite can help to guide reservoir simulation. In particular, simulations for enhanced oil recovery processes by analysing fluid interaction with the confining material. Another advantage is to provide parameters/trends that can be upscaled to model fluid flow using mesoscale techniques, e.g. Lattice-Boltzmann or computational fluid dynamics (CFD). Other applications can also benefit from the diffusion methodology explored, such as nanofluidics and energy storage devices, which must take into account the diffusion at different directions.

8

Suggestions for future work

This work was devoted to investigate diffusion processes in confined materials using molecular dynamics. We developed all the simulation setup and post-processing codes, which are already available to the members of our research group. Some possible topics we think it would be interest to evaluate on this subject would be:

- The first straightforward suggestion is to evaluate the diffusion for other geometries. That would require considering the Smoluchowski equation in different coordinates;
- Evaluate finite-size effects on the self-diffusion calculated through the method proposed by Franco et al. (2016b);
- Focusing on oil and gas systems or even on CCS, it would be interesting to simulate hydrocarbon mixtures containing CO_2 and/or water to see the influence these components have on the self-diffusion profile. We thank Prof. Ioannis Economou for this suggestion;
- Apply different temperatures/temperature gradients to check if the counter-intuitive

adsorption behavior noticed for the non-equilibrium condition is temperature dependent. We thank Prof. Pedro Pessôa for the insights on this matter;

- Thermal diffusion and the Soret coefficient can be a challenging topic to determine through simulation. We suggest further investigating the parameters for bulk systems before trying to extrapolate them to confined media. Perhaps investigating a possible relation between thermal diffusion and the residual entropy. We thank Prof. Joachim Groß for the discussions on this topic;

- It is still required to check if the methodology for the calculation of self-diffusion holds for non-equilibrium conditions. It would also be interest to see if the potential of the mean force from the Smoluchowski equation could be tailored to account for the presence of a temperature gradient, alongside with the influence of the walls. This could allow the calculation of thermal diffusion, but requires theoretical development as it was done by Franco et al. (2016b);

- Once the thermal diffusion is better understood, simulate confined systems in non-equilibrium systematically to obtain average values and their standard deviations of the Soret at the center of the pore;

- Investigate a way to decouple the effects occurring near the surface.

The study of confining systems is a challenging and exciting field, with a lot of open questions and particularities due to specific fluid-wall interactions. Regarding transport properties, the methodologies we used are not the only ones available, but the ones we considered adequate for the system/scale/properties we desired to investigate. We hope this work will help guiding future researchers on their quest for understanding confining fluid properties.

References

M. J. Abraham, T. Murtola, R. Schulz, S. Páll, J. C. Smith, B. Hess, and E. Lindahl. GROMACS: High performance molecular simulations through multi-level parallelism from laptops to supercomputers. *SoftwareX*, 1:19–25, 2015.

C. Abreu. Playmol. `https://github.com/atoms-ufrj/playmol`, 2018.

D. Addari and A. Satta. Influence of $HCOO^-$ on calcite growth from first-principles. *J. Phys. Chem. C*, 119:19780–19788, 2015.

S. Agrawal, M. Elmehlawy, and M. P. Hoepfner. Effect of confinement on the density and diffusivity of organic molecules in single-digit nanopores relative to bulk fluid behavior. *J. Phys. Chem. C*, 2021.

V. Agrawal and S. Sharma. Are we modeling the properties of unconventional shales correctly? *Fuel*, 267:117316, 2020.

R. Aguilera. Shale gas reservoirs: Theoretical, practical and research issues. *Petroleum Research*, 1:10–26, 2016.

C. G. Aimoli, E. J. Maginn, and C. R. Abreu. Force field comparison and thermodynamic property calculation of supercritical co2 and ch4 using molecular dynamics simulations. *Fluid Phase Equilibria*, 368:80–90, 2014a.

C. G. Aimoli, E. J. Maginn, and C. R. Abreu. Transport properties of carbon dioxide and methane from molecular dynamics simulations. *The Journal of chemical physics*, 141(13):134101, 2014b.

C. G. Aimoli, D. P. de Carvalho, P. A. Pessoa Filho, E. J. Maginn, and C. R. Abreu. Thermodynamic properties and fluid phase equilibrium of natural gas containing CO2 and H2O at extreme pressures typically found in pre-salt reservoirs. *J. Nat. Gas Sci. Eng.*, 79:103337, 2020. doi: 10.1016/j.jngse.2020.103337.

S. Al-Anssari, M. Arif, S. Wang, A. Barifcani, M. Lebedev, and S. Iglauer. Wettability of nanofluid-modified oil-wet calcite at reservoir conditions. *Fuel*, 211:405–414, 2018.

M. Alfi, H. Nasrabadi, and D. Banerjee. Effect of confinement on bubble point temperature shift of hydrocarbon mixtures: Experimental investigation using nanofluidic devices. In *SPE Annual Technical Conference and Exhibition*, pages 1–12. Society of Petroleum Engineers, 2017.

A. Ali, T. T. B. Le, A. Striolo, and D. R. Cole. Salt effects on the structure and dynamics of interfacial water on calcite probed by equilibrium molecular dynamics simulations. *J. Phys. Chem. C*, 124:24822–24836, 2020.

M. P. Allen and D. J. Tildesley. *Computer simulation of liquids*. Oxford university press, 2 edition, 2017.

H. C. Andersen. Molecular dynamics simulations at constant pressure and/or temperature. *J. Chem. Phys.*, 72:2384–2393, 1980.

H. Ansari, L. Joss, J. Hwang, J. M. Trusler, G. Maitland, and R. Pini. Supercritical adsorption in micro-and meso-porous carbons and its utilisation for textural characterisation. *Micropor. Mesopor. Mat.*, 308:110537, 2020.

I. S. Araújo and L. F. M. Franco. A model to predict adsorption of mixtures coupled with SAFT-VR Mie equation of state. *Fluid Phase Equilibr.*, 496:61–68, 2019.

P.-A. Artola and B. Rousseau. Microscopic interpretation of a pure chemical contribution to the soret effect. *Phys. Rev. Lett.*, 98:125901, 2007.

P.-A. Artola and B. Rousseau. Thermal diffusion in simple liquid mixtures: what have we learnt from molecular dynamics simulations? *Mol. Phys.*, 111:3394–3403, 2013.

H. Baghooee, F. Montel, G. Galliero, W. Yan, and A. Shapiro. A new approach to thermal segregation in petroleum reservoirs: Algorithm and case studies. *J. Petrol. Sci. Eng.*, page 108367, 2021.

M. Barisik and A. Beskok. Equilibrium molecular dynamics studies on nanoscale-confined fluids. *Microfluid. Nanofluid.*, 11:269–282, 2011.

E. Barsotti, S. P. Tan, S. Saraji, M. Piri, and J.-H. Chen. A review on capillary condensation in nanoporous media: Implications for hydrocarbon recovery from tight reservoirs. *Fuel*, 184:344–361, 2016.

E. Barsotti, S. P. Tan, M. Piri, and J.-H. Chen. Phenomenological study of confined criticality: Insights from the capillary condensation of propane, n-butane, and n-pentane in nanopores. *Langmuir*, 34:4473–4483, 2018.

E. Barsotti, E. Lowry, M. Piri, and J.-H. Chen. Using capillary condensation and evaporation isotherms to investigate confined fluid phase behavior in shales. In *E3S Web of Conferences*, volume 146, page 05003. EDP Sciences, 2020.

H. J. Berendsen, J. v. Postma, W. F. van Gunsteren, A. DiNola, and J. R. Haak. Molecular dynamics with coupling to an external bath. *J. Chem. Phys.*, 81:3684–3690, 1984.

S. K. Bhatia, M. R. Bonilla, and D. Nicholson. Molecular transport in nanopores: a theoretical perspective. *Phys. Chem. Chem. Phys.*, 13(34):15350–15383, 2011.

G. Bhattacharjee, M. N. Goh, S. E. Arumuganainar, Y. Zhang, and P. Linga. Ultra-rapid uptake and the highly stable storage of methane as combustible ice. *Energy Environ. Sci.*, 13:4946–4961, 2020.

R. Bhowmik, R. J. Berry, M. F. Durstock, and B. J. Leever. Prediction of the wetting behavior of active and hole-transport layers for printed flexible electronic devices using molecular dynamics simulations. *ACS Appl. Mater. Interfaces*, 9:19269–19277, 2017.

L. Bocquet and J.-L. Barrat. Hydrodynamic properties of confined fluids. *J. Phys. Condens. Matter*, 8(47):9297, 1996.

S. Bonella, M. Ferrario, and G. Ciccotti. Thermal diffusion in binary mixtures: Transient behavior and transport coefficients from equilibrium and nonequilibrium molecular dynamics. *Langmuir*, 33:11281–11290, 2017.

C. Bousige, P. Levitz, and B. Coasne. Bridging scales in disordered porous media by mapping molecular dynamics onto intermittent brownian motion. *Nat. Commun.*, 12: 1–11, 2021.

J. Brasili, K. Fox, D. Badamo, G. Berghe, R. Khanal, and R. Singh. Molecular dynamics simulation of shale gas confined inside slit-like calcite [104] nanopore. *Mol. Sim.*, 45(2): 104–110, 2019.

M. Bui, C. S. Adjiman, A. Bardow, E. J. Anthony, A. Boston, S. Brown, P. S. Fennell, S. Fuss, A. Galindo, L. A. Hackett, et al. Carbon capture and storage (ccs): the way forward. *Energy Environ. Sci.*, 11:1062–1176, 2018.

T. Bui, A. Phan, D. R. Cole, and A. Striolo. Transport mechanism of guest methane in water-filled nanopores. *J. Phys. Chem. C*, 121:15675–15686, 2017.

G. Bussi, D. Donadio, and M. Parrinello. Canonical sampling through velocity rescaling. *J. Chem. Phys.*, 126(1):014101, 2007.

W. G. Chapman, K. E. Gubbins, G. Jackson, and M. Radosz. New reference equation of state for associating liquids. *Ind. Eng. Chem. Res.*, 29:1709–1721, 1990.

S. Chempath, R. Krishna, and R. Q. Snurr. Nonequilibrium molecular dynamics simulations of diffusion of binary mixtures containing short n-alkanes in faujasite. *J. Phys. Chem. B*, 108(35):13481–13491, 2004.

B. Chen, H. Jiang, X. Liu, and X. Hu. Molecular insight into water desalination across multilayer graphene oxide membranes. *ACS Appl. Mater. Interfaces*, 9:22826–22836, 2017.

H. Chen, A. Z. Panagiotopoulos, and E. P. Giannelis. Atomistic molecular dynamics simulations of carbohydrate–calcite interactions in concentrated brine. *Langmuir*, 31 (8):2407–2413, 2015a.

L. Chen, L. Zhang, Q. Kang, H. S. Viswanathan, J. Yao, and W. Tao. Nanoscale simulation of shale transport properties using the lattice Boltzmann method: permeability and diffusivity. *Sci. Rep.*, 5:1–8, 2015b.

M. Cismondi. Phase envelopes for reservoir fluids with asphaltene onset lines: An integral computation strategy for complex combinations of two-and three-phase behaviors. *Energy Fuels*, pages 2742–2748, 2018.

J. Collell, G. Galliero, R. Vermorel, P. Ungerer, M. Yiannourakou, F. Montel, and M. Pujol. Transport of multicomponent hydrocarbon mixtures in shale organic matter by molecular simulations. *J. Phys. Chem. C*, 119(39):22587–22595, 2015.

J. Colombani, G. Galliéro, B. Duguay, J.-P. Caltagirone, F. Montel, and P. A. Bopp. A molecular dynamics study of thermal diffusion in a porous medium. *Physical Chemistry Chemical Physics*, 4:313–321, 2002.

J. Colombani, G. Galliéro, B. Duguay, J.-P. Caltagirone, F. Montel, and P. A. Bopp. Molecular dynamics study of thermal diffusion in a binary mixture of alkanes trapped in a slit pore. *Philos. Mag.*, 83:2087–2095, 2003.

J. Crank. *The mathematics of diffusion.* Oxford University Press, 1975.

P. T. Cummings and D. J. Evans. Nonequilibrium molecular dynamics approaches to transport properties and non-newtonian fluid rheology. *Ind. Eng. Chem. Res.*, 31: 1237–1252, 1992.

W. Damm, A. Frontera, J. Tirado-Rives, and W. L. Jorgensen. Opls all-atom force field for carbohydrates. *Journal of computational chemistry*, 18(16):1955–1970, 1997.

T. Darden, D. York, and L. Pedersen. Particle mesh ewald: An $N{\cdot}\log(N)$ method for ewald sums in large systems. *J. Chem. Phys.*, 98(12):10089–10092, 1993.

N. Dawass, P. Krüger, S. K. Schnell, J.-M. Simon, and T. J. Vlugt. Kirkwood-buff integrals from molecular simulation. *Fluid Phase Equilib.*, 486:21–36, 2019.

S. R. de Groot and P. Mazur. *Non-equilibrium Thermodynamics*. Dover Publications, 1984.

M. E. Diaz, M. D. Savage, and R. L. Cerro. The effect of temperature on contact angles and wetting transitions for n-alkanes on ptfe. *J. Colloid Interface Sci.*, 503:159–167, 2017.

X. Dong, H. Liu, J. Hou, K. Wu, and Z. Chen. Phase equilibria of confined fluids in nanopores of tight and shale rocks considering the effect of capillary pressure and adsorption film. *Ind. Eng. Chem. Res.*, 55:798–811, 2016.

X. Du, Y. Cheng, Z. Liu, H. Yin, T. Wu, L. Huo, and C. Shu. Co2 and ch4 adsorption on different rank coals: A thermodynamics study of surface potential, gibbs free energy change and entropy loss. *Fuel*, 283:118886, 2021.

M. C. Duarte, J. C. Doblas, M. Gomez, and G. F. Montoya. Modelling the phase behavior of alkane mixtures in wide ranges of conditions: New parameterization and predictive correlations of binary interactions for the rkpr eos. *Fluid Phase Equilib.*, 403:49–59, 2015.

D. Dysthe, A. Fuchs, and B. Rousseau. Prediction of fluid mixture transport properties by molecular dynamics. *Int. J. Thermophys.*, 19:437–448, 1998.

D. K. Dysthe, F. Renard, F. Porcheron, and B. Rousseau. Fluid in mineral interfaces: molecular simulations of structure and diffusion. *Geophys. Res. Lett.*, 29:13, 2002.

M. O. M. Eric W. Lemmon and D. G. Friend. Thermophysical properties of fluid systems. In P. Linstrom and W. Mallard, editors, *NIST Chemistry WebBook - NIST Standard Reference Database*, number 69. National Institute of Standards and Technology, Gaithersburg MD, 20899, 2021.

R. O. Esposito, P. H. R. Alijó, J. A. Scilipoti, and F. W. Tavares. *Compositional grading in oil and gas reservoirs*. Gulf Professional Publishing, 2017.

D. J. Evans and G. Morriss. *Statistical Mechanics of Nonequilibrium Liquids*. Cambridge Univ. Press, 2008.

K. Falk, B. Coasne, R. Pellenq, F.-J. Ulm, and L. Bocquet. Subcontinuum mass transport of condensed hydrocarbons in nanoporous media. *Nat. Commun.*, 6:6949, 2015.

B. Fazelabdolabadi and A. Alizadeh-Mojarad. A molecular dynamics investigation into the adsorption behavior inside {001} kaolinite and {1014} calcite nano-scale channels: the case with confined hydrocarbon liquid, acid gases, and water. *Appl. Nanosci.*, 7: 155–165, 2017.

G. Fernández, J. Vrabec, and H. Hasse. Self-diffusion and binary maxwell–stefan diffusion coefficients of quadrupolar real fluids from molecular simulation. *Int. J. Thermophys.*, 26:1389–1407, 2005.

M. J. Field. *A Practical Introduction to the Simulation of Molecular Systems*. Cambridge University Press, 2007.

L. F. M. Franco. On the structure of a confined ideal gas: A statistical mechanical description with an external field. *Fluid Phase Equilibr.*, 489:99–103, 2019.

L. F. M. Franco, M. Castier, and I. G. Economou. Anisotropic parallel self-diffusion coefficients near the calcite surface: A molecular dynamics study. *J. Chem. Phys.*, 145: 084702, 2016a.

L. F. M. Franco, M. Castier, and I. G. Economou. Diffusion in homogeneous and in inhomogeneous media: a new unified approach. *J. Chem. Theory Comput.*, 12:5247–5255, 2016b.

L. F. M. Franco, I. G. Economou, and M. Castier. Statistical mechanical model for adsorption coupled with SAFT-VR Mie equation of state. *Langmuir*, 33:11291–11298, 2017.

D. Frenkel and B. Smit. *Understanding molecular simulation: From algorithms to applications*. Academic Press, 2002.

W. Furry, R. C. Jones, and L. Onsager. On the theory of isotope separation by thermal diffusion. *Phys. Rev.*, 55:1083, 1939.

F. Furtado, A. Silveira, C. Abreu, and F. Tavares. Non-equilibrium molecular dynamics used to obtain soret coefficients of binary hydrocarbon mixtures. *Braz. J. Chem. Eng.*, 32:683–698, 2015.

G. Galliero. Lennard-jones fluid-fluid interfaces under shear. *Phys. Rev. E*, 81:056306, 2010.

G. Galliéro, B. Duguay, J.-P. Caltagirone, and F. Montel. Thermal diffusion sensitivity to the molecular parameters of a binary equimolar mixture, a non-equilibrium molecular dynamics approach. *Fluid Phase Equilib.*, 208:171–188, 2003.

G. Galliéro, J. Colombani, P. A. Bopp, B. Duguay, J.-P. Caltagirone, and F. Montel. Thermal diffusion in micropores by molecular dynamics computer simulations. *Physica A*, 361:494–510, 2006.

G. Galliero, H. Bataller, F. Croccolo, R. Vermorel, P.-A. Artola, B. Rousseau, V. Vesovic, M. Bou-Ali, J. M. O. De Zárate, S. Xu, et al. Impact of thermodiffusion on the initial vertical distribution of species in hydrocarbon reservoirs. *Microgravity Sci. Technol.*, 28:79–86, 2016.

G. Galliero, H. Bataller, J.-P. Bazile, J. Diaz, F. Croccolo, H. Hoang, R. Vermorel, P.-A. Artola, B. Rousseau, V. Vesovic, M. M. Bou-Ali, de Zárete José MO, S. Xu, K. Zhang, F. Montel, A. Verga, and O. Minster. Thermodiffusion in multicomponent n-alkane mixtures. *NPJ Microgravity*, 3:20, 2017.

Z. Gao, N. Giovambattista, and O. Sahin. Phase diagram of water confined by graphene. *Sci. Rep.*, 8:1–11, 2018.

L. D. Gelb, K. E. Gubbins, R. Radhakrishnan, and M. Sliwinska-Bartkowiak. Phase separation in confined systems. *Rep. Prog. Phys.*, 62(12):1573, 1999.

K. Ghorayeb, A. Firoozabadi, T. Anraku, et al. Interpretation of the unusual fluid distribution in the yufutsu gas-condensate field. *SPE journal*, 8:114–123, 2003.

J. Gross. An equation-of-state contribution for polar components: Quadrupolar molecules. *AIChE J.*, 51:2556–2568, 2005.

J. Gross and G. Sadowski. Perturbed-Chain SAFT: An Equation of State Based on a Perturbation Theory for Chain Molecules. *Ind. Eng. Chem. Res.*, 40:1244–1260, 2001.

J. Gross and J. Vrabec. An equation-of-state contribution for polar components: dipolar molecules. *AIChE J.*, 52(3):1194–1204, 2006.

K. E. Gubbins, Y.-C. Liu, J. D. Moore, and J. C. Palmer. The role of molecular modeling in confined systems: impact and prospects. *Phys. Chem. Chem. Phys.*, 13:58–85, 2011.

B. Hafskjold. Non-equilibrium molecular dynamics simulations of the transient ludwig-soret effect in a binary lennard-jones/spline mixture. *Eur. Phys. J. E*, 40:4, 2017.

S. J. Han, H. M. Lin, and K. C. Chao. Vapor-liquid equilibrium of molecular fluid mixtures by equation of state. *Chem. Eng. Sci.*, 43:2327–2367, 1988.

R. Hannaoui, G. Galliero, H. Hoang, and C. Boned. Influence of confinement on thermodiffusion. *J. Chem. Phys.*, 139:114704, 2013.

J.-P. Hansen and I. R. McDonald. *Theory of simple liquids: with applications to soft matter*. Academic Press, 2013.

S. He, J. C. Palmer, and G. Qin. A non-equilibrium molecular dynamics study of methane transport in clay nano-pores. *Microporous and Mesoporous Materials*, 249:88–96, 2017.

C. Herdes, C. Petit, A. Mejía, and E. A. Muller. Combined experimental, theoretical, and molecular simulation approach for the description of the fluid-phase behavior of hydrocarbon mixtures within shale rocks. *Energy Fuels*, 32(5):5750–5762, 2018.

W. G. Hoover. Canonical dynamics: Equilibrium phase-space distributions. *Phys. Rev. A*, 31:1695, 1985.

M. Hopp, J. Mele, and J. Gross. Self-diffusion coefficients from entropy scaling using the PCP-SAFT equation of state. *Ind. Eng. Chem. Res.*, 57(38):12942–12950, 2018.

D. Huang, T. Zhang, G. Xiong, L. Xu, Z. Qu, E. Lee, and T. Luo. Tuning water slip behavior in nanochannels using self-assembled monolayers. *ACS Appl. Mater. Interfaces*, 11:32481–32488, 2019.

G. Hummer. Position-dependent diffusion coefficients and free energies from Bayesian analysis of equilibrium and replica molecular dynamics simulations. *New J. Phys.*, 7 (1):34, 2005.

N. Jackson, J. M. Rubi, and F. Bresme. Non-equilibrium molecular dynamics simulations of the thermal transport properties of lennard-jones fluids using configurational temperatures. *Mol. Sim.*, 42:1214–1222, 2016.

B. Jin and H. Nasrabadi. Phase behavior of multi-component hydrocarbon systems in nano-pores using gauge-gcmc molecular simulation. *Fluid Phase Equilib.*, 425:324–334, 2016.

B. Jin, R. Bi, and H. Nasrabadi. Molecular simulation of the pore size distribution effect on phase behavior of methane confined in nanopores. *Fluid Phase Equilib.*, 452:94–102, 2017.

Z. Jin and A. Firoozabadi. Flow of methane in shale nanopores at low and high pressure by molecular dynamics simulations. *J. Chem. Phys.*, 143(10):104315, 2015.

W. L. Jorgensen, J. D. Madura, and C. J. Swenson. Optimized intermolecular potential functions for liquid hydrocarbons. *J. Am. Chem. Soc.*, 106:6638–6646, 1984.

C. R. Kamala, K. G. Ayappa, and S. Yashonath. Distinct diffusion in binary mixtures confined in slit graphite pores. *J. Phys. Chem. B*, 108(14):4411–4421, 2004.

D. J. Keffer and P. Adhangale. The composition dependence of self and transport diffusivities from molecular dynamics simulations. *Chem. Eng. J.*, 100(1-3):51–69, 2004.

J. G. Kirkwood and F. P. Buff. The statistical mechanical theory of solutions. i. *J. Chem. Phys.*, 19:774–777, 1951.

S. Kjelstrup and D. Bedeaux. *Non-equilibrium Thermodynamics Of Heterogeneous Systems*, volume 16. World Scientific, 2008.

S. Kjelstrup, D. Bedeaux, I. Inzoli, and J.-M. Simon. Criteria for validity of thermodynamic equations from non-equilibrium molecular dynamics simulations. *Energy*, 33: 1185–1196, 2008.

S. Kjelstrup, D. Bedeaux, E. Johannessen, and J. Gross. *Non-equilibrium thermodynamics for engineers*. World Scientific, 2017.

M. M. Koleini, M. F. Mehraban, and S. Ayatollahi. Effects of low salinity water on calcite/brine interface: A molecular dynamics simulation study. *Colloids Surf. A: Physicochem. Eng. Asp.*, 537:61–68, 2018.

R. Krishna and J. Van Baten. The darken relation for multicomponent diffusion in liquid mixtures of linear alkanes: an investigation using molecular dynamics (md) simulations. *Ind. Eng. Chem. Res.*, 44:6939–6947, 2005.

N. A. Krishnan, B. Wang, G. Falzone, Y. Le Pape, N. Neithalath, L. Pilon, M. Bauchy, and G. Sant. Confined water in layered silicates: the origin of anomalous thermal expansion behavior in calcium-silicate-hydrates. *ACS Appl. Mater. Interfaces*, 8:35621–35627, 2016.

T. T. B. Le, A. Striolo, and D. R. Cole. Supercritical co2 effects on calcite wettability: A molecular perspective. *J. Phys. Chem. C*, 124:18532–18543, 2020.

T. Lee, L. Bocquet, and B. Coasne. Activated desorption at heterogeneous interfaces and long-time kinetics of hydrocarbon recovery from nanoporous media. *Nat. Commun.*, 7: 1–10, 2016.

J. Li, S. Lu, L. Xie, J. Zhang, H. Xue, P. Zhang, and S. Tian. Modeling of hydrocarbon adsorption on continental oil shale: A case study on n-alkane. *Fuel*, 206:603–613, 2017.

J. Li, Q. Rao, Y. Xia, M. Hoepfner, and M. D. Deo. Confinement-mediated phase behavior of hydrocarbon fluids: Insights from monte carlo simulations. *Langmuir*, 2020.

P. Linstrom and E. W.G. Mallard. *NIST Chemistry WebBook, NIST Standard Reference Database Number 69*, volume 20899. National Institute of Standards and Technology, Gaithersburg MD, 2018.

R. Littke, D. R. Baker, and D. Leythaeuser. Microscopic and sedimentologic evidence for the generation and migration of hydrocarbons in toarcian source rocks of different maturities. In *Organic Geochemistry In Petroleum Exploration*, pages 549–559. Elsevier, 1988.

B. Liu, C. Wang, J. Zhang, S. Xiao, Z. Zhang, Y. Shen, B. Sun, and J. He. Displacement mechanism of oil in shale inorganic nanopores by supercritical carbon dioxide from molecular dynamics simulations. *Energy & Fuels*, 31(1):738–746, 2017.

B. Liu, C. Qi, T. Mai, J. Zhang, K. Zhan, Z. Zhang, and J. He. Competitive adsorption and diffusion of ch4/co2 binary mixture within shale organic nanochannels. *Journal of Natural Gas Science and Engineering*, 53:329–336, 2018.

P. Liu, E. Harder, and B. J. Berne. On the calculation of diffusion coefficients in confined fluids and interfaces with an application to the liquid- vapor interface of water. *J. Phys. Chem. B*, 108(21):6595–6602, 2004.

X. Liu and D. Zhang. A review of phase behavior simulation of hydrocarbons in confined space: Implications for shale oil and shale gas. *J. Nat. Gas Sci. Eng.*, 68:102901, 2019.

S. Luo, L. Zeng, D. Xu, M. Kathe, E. Chung, N. Deshpande, L. Qin, A. Majumder, T.-L. Hsieh, A. Tong, et al. Shale gas-to-syngas chemical looping process for stable shale gas conversion to high purity syngas with a h 2: Co ratio of 2: 1. *Energy Environ. Sci.*, 7: 4104–4117, 2014.

M. G. Martin and J. I. Siepmann. Transferable potentials for phase equilibria. 1. United-atom description of n-alkanes. *J. Phys. Chem. B*, 102(14):2569–2577, 1998.

L. Martínez, R. Andrade, E. G. Birgin, and J. M. Martínez. Packmol: a package for building initial configurations for molecular dynamics simulations. *J. Comput. Chem.*, 30:2157–2164, 2009.

D. A. McQuarrie. *Statistical mechanics*. University Science Books, 2000.

J. Mittal, T. M. Truskett, J. R. Errington, and G. Hummer. Layering and position-dependent diffusive dynamics of confined fluids. *Phys. Rev. Lett.*, 100(14):145901, 2008.

S. Mohammed and G. Gadikota. The influence of co2 on the structure of confined asphaltenes in calcite nanopores. *Fuel*, 236:769–777, 2019a.

S. Mohammed and G. Gadikota. The role of calcite and silica interfaces on the aggregation and transport of asphaltenes in confinement. *J. Mol. Liq.*, 274:792–800, 2019b.

S. Mohammed and G. Gadikota. Dynamic wettability alteration of calcite, silica and illite surfaces in subsurface environments: a case study of asphaltene self-assembly at solid interfaces. *Appl. Surf. Sci.*, 505:144516, 2020.

F. Montel, J. Bickert, A. Lagisquet, and G. Galliéro. Initial state of petroleum reservoirs: A comprehensive approach. *J. Pet. Sci. Eng.*, 58:391–402, 2007.

K. Mosher, J. He, Y. Liu, E. Rupp, and J. Wilcox. Molecular simulation of methane adsorption in micro-and mesoporous carbons with applications to coal and gas shale systems. *Int. J. Coal Geol.*, 109:36–44, 2013.

R. Mu and V. M. Malhotra. Effects of surface and physical confinement on the phase transitions of cyclohexane in porous silica. *Phys. Rev. B*, 44:4296, 1991.

J. Muscatello, F. Jaeger, O. K. Matar, and E. A. Mueller. Optimizing water transport through graphene-based membranes: insights from nonequilibrium molecular dynamics. *ACS Appl. Mater. Interfaces*, 8:12330–12336, 2016.

H. Nasrabadi, K. Ghorayeb, A. Firoozabadi, et al. Two-phase multicomponent diffusion and convection for reservoir initialization. *SPE Reserv. Eng.*, 9:530–542, 2006.

I. Nitzke, K. Fackeldey, and J. Vrabec. Long range corrections for inhomogeneous fluids containing a droplet or a bubble. *Molecular Simulation*, pages 1–14, 2021.

S. Nosé. A unified formulation of the constant temperature molecular dynamics methods. *J. Chem. Phys.*, 81:511–519, 1984.

K. Nygård. Local structure and density fluctuations in confined fluids. *Curr. Opin. Colloid In.*, 22:30–34, 2016.

R. Otero, F. Hümmelink, F. Sato, S. B. Legoas, P. Thostrup, E. Lægsgaard, I. Stensgaard, D. S. Galvão, and F. Besenbacher. Lock-and-key effect in the surface diffusion of large organic molecules probed by stm. *Nat. Mater.*, 3:779–782, 2004.

M. Parrinello and A. Rahman. Polymorphic transitions in single crystals: A new molecular dynamics method. *J. Appl. Phys.*, 52:7182–7190, 1981.

S. Patankar, S. Gautam, G. Rother, A. Podlesnyak, G. Ehlers, T. Liu, D. R. Cole, and D. L. Tomasko. Role of confinement on adsorption and dynamics of ethane and an ethane-CO2 mixture in mesoporous CPG silica. *J. Phys. Chem. C*, 120(9):4843–4853, 2016.

A. Pavese, M. Catti, G. Price, and R. Jackson. Interatomic potentials for caco 3 polymorphs (calcite and aragonite), fitted to elastic and vibrational data. *Physics and chemistry of minerals*, 19(2):80–87, 1992.

K. S. Pedersen, H. P. Hjermstad, et al. Modeling of compositional variation with depth for five north sea reservoirs. In *SPE Annual Technical Conference and Exhibition*. Society of Petroleum Engineers, 2015.

S. Polarz, B. Völker, and F. Jeremias. Metathesis catalysts in confining reaction fields—confinement effects vs. surface effects. *Dalton Trans.*, 39:577–584, 2010.

M. Pourali and A. Maghari. Non-equilibrium molecular dynamics simulation of thermal conductivity and thermal diffusion of binary mixtures confined in a nanochannel. *Chem. Phys.*, 444:30–38, 2014.

H. S. Rabbani, V. Joekar-Niasar, T. Pak, and N. Shokri. New insights on the complex dynamics of two-phase flow in porous media under intermediate-wet conditions. *Sci. Rep.*, 7:1–7, 2017.

P. Raiteri, J. D. Gale, D. Quigley, and P. M. Rodger. Derivation of an accurate force-field for simulating the growth of calcium carbonate from aqueous solution: A new model for the calcite- water interface. *The Journal of Physical Chemistry C*, 114(13):5997–6010, 2010.

S. Ravipati, M. S. Santos, I. G. Economou, A. Galindo, G. Jackson, and A. J. Haslam. Monte carlo molecular simulation study of carbon dioxide sequestration into dry and wet calcite pores containing methane. *Energy & Fuels*, 2021.

T. F. Rexer, E. J. Mathia, A. C. Aplin, and K. M. Thomas. High-pressure methane adsorption and characterization of pores in posidonia shales and isolated kerogens. *Energy Fuels*, 28:2886–2901, 2014.

B. Sage, H. Reamer, R. Olds, and W. Lacey. Phase equilibria in hydrocarbon systems. *Ind. Eng. Chem.*, 34:1108–1117, 1942.

S. Salahshoor, M. Fahes, and C. Teodoriu. A review on the effect of confinement on phase behavior in tight formations. *J. Nat. Gas Sci. Eng.*, 51:89–103, 2018.

M. S. Santos, L. F. M. Franco, M. Castier, and I. G. Economou. Molecular dynamics simulation of n-alkanes and CO_2 confined by calcite nanopores. *Energy Fuels*, 32:1934–1941, 2018.

M. S. Santos, M. Castier, and I. G. Economou. Molecular dynamics simulation of electrolyte solutions confined by calcite mesopores. *Fluid Phase Equilib.*, 487:24–32, 2019.

T. J. Santos, F. W. Tavares, and C. R. Abreu. Fick diffusion coefficients via molecular dynamics: an alternative approach in the fourier domain. *J. Mol. Liq.*, 329:115460, 2021.

F. Sato, S. B. Legoas, R. Otero, F. Hümmelink, P. Thostrup, E. Lægsgaard, I. Stensgaard, F. Besenbacher, and D. S. Galvão. Adsorption configuration effects on the surface diffusion of large organic molecules: The case of violet Lander. *J. Chem. Phys.*, 133: 224702, 2010.

S. K. Schnell, X. Liu, J.-M. Simon, A. Bardow, D. Bedeaux, T. J. Vlugt, and S. Kjelstrup. Calculating thermodynamic properties from fluctuations at small scales. *J. Phys. Chem. B*, 115:10911–10918, 2011.

S. K. Schnell, R. Skorpa, D. Bedeaux, S. Kjelstrup, T. J. Vlugt, and J.-M. Simon. Partial molar enthalpies and reaction enthalpies from equilibrium molecular dynamics simulation. *J. Chem. Phys.*, 141:144501, 2014.

C. W. Scholz, Y. Sanchez-Vicente, T. Tananilgul, M. Thol, J. M. Trusler, and M. Richter. Speeds of sound in n-pentane at temperatures from 233.50 to 473.15 k at pressures up to 390 mpa. *J. Chem. Eng. Data*, 65:3679–3689, 2020.

M. Sedghi and M. Piri. Capillary condensation and capillary pressure of methane in carbon nanopores: Molecular dynamics simulations of nanoconfinement effects. *Fluid Phase Equilib.*, 459:196–207, 2018.

S. A. Setu, R. P. A. Dullens, A. Hernández-Machado, I. Pagonabarraga, D. G. A. L. Aarts, and R. Ledesma-Aguilar. Superconfinement tailors fluid flow at microscales. *Nat. Commun.*, 6:7297, 2015.

B. L. Severson and R. Q. Snurr. Monte carlo simulation of n-alkane adsorption isotherms in carbon slit pores. *J Chem. Phys.*, 126:134708, 2007.

A. Sharma, S. Namsani, and J. K. Singh. Molecular simulation of shale gas adsorption and diffusion in inorganic nanopores. *Mol. Sim.*, 41(5-6):414–422, 2015.

A. Silvestri, E. Ataman, A. Budi, S. Stipp, J. D. Gale, and P. Raiteri. Wetting properties of the co2–water–calcite system via molecular simulations: Shape and size effects. *Langmuir*, 35:16669–16678, 2019.

J.-M. Simon, D. Dysthe, A. Fuchs, and B. Rousseau. Thermal diffusion in alkane binary mixtures: A molecular dynamics approach. *Fluid Phase Equilib.*, 150:151–159, 1998.

P. Simonnin, B. Noetinger, C. Nieto-Draghi, V. Marry, and B. Rotenberg. Diffusion under confinement: hydrodynamic finite-size effects in simulation. *J. Chem. Theory Comput.*, 13:2881–2889, 2017.

P. Simonnin, V. Marry, B. Noetinger, C. Nieto-Draghi, and B. Rotenberg. Mineral-and ion-specific effects at clay-water interfaces: Structure, diffusion, and hydrodynamics. *J. Phys. Chem. C*, 122:18484–18492, 2018.

Z. Song, Y. Song, J. Guo, Z. Zhang, and J. Hou. Adsorption induced critical shifts of confined fluids in shale nanopores. *Chem. Eng. J.*, 385:123837, 2020.

M. B. M. Spera and L. F. M. Franco. Surface and confinement effects on the self-diffusion coefficients for methane-ethane mixtures within calcite nanopores. *Fluid Phase Equilib.*, page 112740, 2020.

A. Striolo and D. R. Cole. Understanding shale gas: Recent progress and remaining challenges. *Energy Fuels*, 31:10300–10310, 2017.

N. Sunny, N. Mac Dowell, and N. Shah. What is needed to deliver carbon-neutral heat using hydrogen and ccs? *Energy Environ. Sci.*, 13:4204–4224, 2020.

S. P. Tan and M. Piri. Equation-of-state modeling of associating-fluids phase equilibria in nanopores. *Fluid Phase Equilib.*, 405:157–166, 2015a.

S. P. Tan and M. Piri. Equation-of-state modeling of confined-fluid phase equilibria in nanopores. *Fluid Phase Equilib.*, 393:48–63, 2015b.

S. P. Tan, H. Adidharma, and M. Radosz. Recent advances and applications of statistical associating fluid theory. *Ind. Eng. Chem. Res.*, 47:8063–8082, 2008.

X. Tang and J. Gross. Modeling the phase equilibria of hydrogen sulfide and carbon dioxide in mixture with hydrocarbons and water using the PCP-SAFT equation of state. *Fluid Phase Equilib.*, 293:11–21, 2010.

N. G. Tassin, V. A. Mascietti, and M. Cismondi. Phase behavior of multicomponent alkane mixtures and evaluation of predictive capacity for the pr and rkpr eos's. *Fluid Phase Equilib.*, 480:53–65, 2019a.

N. G. Tassin, S. B. Rodríguez Reartes, and M. Cismondi. New Correlations for Prediction of High-Pressure Phase Equilibria of n-Alkane Mixtures with the RKPR EoS: Back from the Use of l ij (Repulsive) Interaction Parameters. *J. Chem. Eng. Data*, 64:2093–2109, 2019b.

L. Travalloni, M. Castier, F. W. Tavares, and S. I. Sandler. Critical behavior of pure confined fluids from an extension of the van der Waals equation of state. *J. Supercrit. Fluids*, 55:455–461, 2010a.

L. Travalloni, M. Castier, F. W. Tavares, and S. I. Sandler. Thermodynamic modeling of confined fluids using an extension of the generalized van der Waals theory. *Chem. Eng. Sci.*, 65:3088–3099, 2010b.

L. Travalloni, M. Castier, and F. W. Tavares. Phase equilibrium of fluids confined in porous media from an extended Peng-Robinson equation of state. *Fluid Phase Equilibr.*, 362:335–341, 2014.

J. Trusler and M. Zarari. The speed of sound and derived thermodynamic properties of methane at temperatures between 275 k and 375 k and pressures up to 10 mpa. *J. Chem. Thermodynamics*, 24:973–991, 1992.

I. N. Tsimpanogiannis, O. A. Moultos, L. F. M. Franco, M. B. d. M. Spera, M. Erdős, and I. G. Economou. Self-diffusion coefficient of bulk and confined water: a critical review of classical molecular simulation studies. *Mol. Sim.*, 45(4-5):425–453, 2019.

P. Ungerer, B. Tavitian, and A. Boutin. *Applications of molecular simulation in the oil and gas industry: Monte Carlo methods*. Editions Technip, 2005.

P. Ungerer, V. Lachet, and B. Tavitian. Applications of molecular simulation in oil and gas production and processing. *Oil Gas Sci. Technol. - Rev. IFP Energies nouvelles*, 61:387–403, 2006.

P. Ungerer, C. Nieto-Draghi, V. Lachet, A. Wender, A. Di Lella, A. Boutin, B. Rousseau, and A. H. Fuchs. Molecular simulation applied to fluid properties in the oil and gas industry. *Mol. Sim.*, 33:287–304, 2007.

R. Vogelsang, C. Hoheisel, G. Paolini, and G. Ciccotti. Soret coefficient of isotopic lennard-jones mixtures and the ar-kr system as determined by equilibrium molecular-dynamics calculations. *Phys. Rev. A*, 36:3964, 1987.

J. Vrabec and J. Gross. Vapor-liquid equilibria simulation and an equation of state contribution for dipole-quadrupole interactions. *J. Phys. Chem. B*, 112:51–60, 2007.

J. P. R. B. Walton and N. P. R. B. Quirke. Capillary condensation: a molecular simulation study. *Mol. Sim.*, 2:361–391, 1989.

H. Wang, Z. Qu, Y. Yin, J. Bai, and B. Yu. Review of molecular simulation method for gas adsorption/desorption and diffusion in shale matrix. *J. Therm. Sci.*, 28:1–16, 2019.

Q. Wang and L. Huang. Molecular insight into competitive adsorption of methane and carbon dioxide in montmorillonite: Effect of clay structure and water content. *Fuel*, 239:32–43, 2019.

S. Wang, Q. Feng, F. Javadpour, T. Xia, and Z. Li. Oil adsorption in shale nanopores and its effect on recoverable oil-in-place. *Int. J. Coal Geol.*, 147:9–24, 2015.

S. Wang, F. Javadpour, and Q. Feng. Molecular dynamics simulations of oil transport through inorganic nanopores in shale. *Fuel*, 171:74–86, 2016.

I. Wichterle and R. Kobayashi. Vapor-liquid equilibrium of methane-ethane system at low temperatures and high pressures. *J. Chem. Eng. Data*, 17:9–12, 1972.

B. Widom. Some topics in the theory of fluids. *The Journal of Chemical Physics*, 39(11): 2808–2812, 1963.

H. Wu, Y. He, and R. Qiao. Recovery of multicomponent shale gas from single nanopores. *Energy Fuels*, 31(8):7932–7940, 2017.

T. Wu and A. Firoozabadi. Molecular simulations of binary gas mixture transport and separation in slit nanopores. *J. Phys. Chem. C*, 122:20727–20735, 2018.

S. Xiao, S. A. Edwards, and F. Gräter. A new transferable forcefield for simulating the mechanics of CaCO3 crystals. *J. Phys. Chem. C*, 115(41):20067–20075, 2011.

J. Xu, S. Kjelstrup, and D. Bedeaux. Molecular dynamics simulations of a chemical reaction; conditions for local equilibrium in a temperature gradient. *Phys. Chem. Chem. Phys.*, 8:2017–2027, 2006.

Y. Yan, C. Li, Z. Dong, T. Fang, B. Sun, and J. Zhang. Enhanced oil recovery mechanism of co2 water-alternating-gas injection in silica nanochannel. *Fuel*, 190:253–259, 2017.

I.-C. Yeh and G. Hummer. System-size dependence of diffusion coefficients and viscosities from molecular dynamics simulations with periodic boundary conditions. *J. Phys. Chem. B*, 108:15873–15879, 2004.

X. Yu, J. Li, Z. Chen, K. Wu, L. Zhang, G. Hui, and M. Yang. Molecular dynamics computations of brine-co2/ch4-shale contact angles: Implications for co2 sequestration and enhanced gas recovery. *Fuel*, 280:118590, 2020.

Q. Yuan, X. Zhu, K. Lin, and Y.-P. Zhao. Molecular dynamics simulations of the enhanced recovery of confined methane with carbon dioxide. *Phys. Chem. Chem. Phys.*, 17:31887–31893, 2015.

J. Zhang, C. Wei, C. Zhao, T. Zhang, G. Lu, and M. Zou. Effects of nano-pore and macromolecule structure of coal samples on energy parameters variation during methane adsorption under different temperature and pressure. *Fuel*, 289:119804, 2021a.

W. Zhang, Q. Feng, S. Wang, X. Xing, and Z. Jin. Co2-regulated octane flow in calcite nanopores from molecular perspectives. *Fuel*, 286:119299, 2021b.

Y. Zhang, H. R. Lashgari, Y. Di, and K. Sepehrnoori. Capillary pressure effect on phase behavior of co2/hydrocarbons in unconventional reservoirs. *Fuel*, 197:575–582, 2017.

J. Zhao, G. Yao, S. B. Ramisetti, R. B. Hammond, and D. Wen. Molecular dynamics investigation of substrate wettability alteration and oil transport in a calcite nanopore. *Fuel*, 239:1149–1161, 2019.

J. Zhao, G. Yao, and D. Wen. Salinity-dependent alterations of static and dynamic contact angles in oil/brine/calcite systems: A molecular dynamics simulation study. *Fuel*, 272: 117615, 2020.

X. Zheng, B. Zhang, H. Sanei, H. Bao, Z. Meng, C. Wang, and K. Li. Pore structure characteristics and its effect on shale gas adsorption and desorption behavior. *Mar. Pet. Geol.*, 100:165–178, 2019.

Appendices

A

Force field parameters

To model hydrocarbons, we used the the Transferable Potential for Phase Equilibria (TraPPE) force field developed by Martin and Siepmann (1998). Unlike fully atomistic representations, such as the OPLS-AA force field from Damm et al. (1997), TraPPE force field implicitly account for hydrogen atoms by using an United-Atom approach. Although information about the interaction of the hydrogen with the carbonate from calcite can be lost, we gain computational power. It is a well established force field and accurately describes equilibrium and transport properties of hydrocarbons, as is shown by Aimoli and co-workers (Aimoli et al., 2014a,b, 2020). Calcite crystals were described by the force field proposed by Xiao et al. (2011). This force field is one of the possible descriptions of calcite crystals, among force fields proposed by Pavese et al. (1992) and Raiteri et al. (2010), for example. The advantages of Xiao et al. (2011) force field for our studies are that it captures the elastic properties of the calcite crystal and is transferable for similar minerals. Also, it was developed based on the Lennard-Jones potential, which is the same potential used for TraPPE force field.

A.1 Bonded parameters

Bond lengths between hydrocarbon pseudoatoms are fixed as 1.54 Å, and C−O bonds from the carbonate molecule are fixed as 1.18 Å. Bond angles are described as harmonic potentials, as shown in Eq. 2.8. The equilibrium angle θ for hydrocarbons is set to 114° and for O−C−O is 120°, with force constants $k_\theta = 519.625$ kJ·mol^{-1}·rad^{-2} for

hydrocarbons and $k_\theta = 1852$ kJ·mol^{-1}·rad^{-2} for calcite. These values are taken from the previously mentioned force fields. Regarding torsion potential, the motions of dihedral angles, ϕ, for hydrocarbons is described by Eq. A.1 (Jorgensen et al., 1984; Martin and Siepmann, 1998).

$$u_{\text{torsions}} = c_1[1 + \cos\phi] + c_2[1 - \cos(2\phi)] + c3[1 + \cos(3\phi)] \tag{A.1}$$

with $c_1/k_\text{B} = 335.03$ K, $c_2/k_\text{B} = -68.19$ K, and $c_3/k_\text{B} = 791.32$ K. For calcite, Xiao et al. (2011) describes the torsion potential as Eq. A.2, with $k_\phi = 28.9$ kJ·mol^{-1}.

$$u_{\text{torsions}} = \sum_{\text{torsions}} \frac{1}{2} k_\phi (1 - \cos(2\phi)) \tag{A.2}$$

A.2 Nonbonded parameters

Table A.1: LJ parameters. Hydrocarbons were modeled using the Transferable Potential for Phase Equilibria (TraPPE) force field from Martin and Siepmann (1998) and calcium carbonate parameters were taken from Xiao et al. (2011).

Particle	C_6 (kJ· mol^{-1}· nm^{-6})	C_{12} (kJ· mol^{-1}· nm^{-12})	Charge (e)
CH_4	1.33×10^{-2}	3.57×10^{-5}	0
CH_3	9.06×10^{-3}	2.52×10^{-5}	0
CH_2	5.81×10^{-3}	2.21×10^{-5}	0
Ca	1.42×10^{-3}	2.52×10^{-7}	+1.668
C	4.61×10^{-3}	1.44×10^{-5}	+0.999
O	2.03×10^{-3}	1.77×10^{-6}	−0.889

Table A.2: Crossed nonbonded LJ parameters. Hydrocarbons were modeled using the Transferable Potential for Phase Equilibria (TraPPE) force field from Martin and Siepmann (1998) and calcium carbonate parameters were taken from Xiao et al. (2011).

Particle 1	**Particle 2**	C_6 (kJ· mol^{-1}· nm^{-6})	C_{12} (kJ· mol^{-1}· nm^{-12})
CH_4	CH_4	1.33×10^{-2}	3.57×10^{-5}
CH_3	CH_3	9.06×10^{-3}	2.52×10^{-5}
CH_2	CH_2	5.81×10^{-3}	2.21×10^{-5}
CH_4	CH_3	1.10×10^{-2}	3.00×10^{-5}
CH_4	CH_2	8.80×10^{-3}	2.82×10^{-5}
CH_3	CH_2	7.27×10^{-3}	2.37×10^{-5}
Ca	Ca	1.42×10^{-3}	2.52×10^{-7}
Ca	O	0	9.49×10^{-7}
C	C	1.43×10^{-2}	4.61×10^{-6}
C	O	3.08×10^{-4}	9.04×10^{-10}
O	O	5.21×10^{-5}	5.94×10^{-7}

B

Vapor-liquid equilibrium of natural gas components and their binary mixtures

Oil and gas industries handle different systems from a wide range of thermodynamic states, and it is important to know the phase coexistence properties under the desired conditions. This appendix provides phase equilibrium data for pure components and binary mixtures of methane and heavier hydrocarbons. The results were obtained with PC-SAFT equation of state, and although it covers bulk systems with a different model and parameter from our simulations, this mapping provides key information to guide the study of thermophysical and transport phenomena involving natural gas.

B.1 Introduction

Operations in oil and gas industry involve a broad range of thermodynamic conditions and compositions, presenting a great challenge to describe fluid behavior (Ungerer et al., 2007; Aimoli et al., 2020). Knowledge of phase coexistence properties is important for mass transfer and separation processes in hydrocarbon processing (distillation- or adsorption-based), influencing energy requirements and equipment design (Ungerer et al., 2005). When aiming to study oil and gas systems, it is important to know to fluid behavior under desired reservoir conditions.

To correctly describe the phase behavior of these multicomponent systems, a good representation of its binary constituents is required (Tassin et al., 2019b). Equations of

state extend the existent experimental data, and have been extensively studied and improved to predict the phase properties of hydrocarbon mixtures (Han et al., 1988; Duarte et al., 2015; Cismondi, 2018; Tassin et al., 2019a). The theoretical models based on the associating fluid theory have a strong background that allows reliable extrapolations for a wide range of temperatures and pressures, being a realistic alternative to the conventional cubic equations of state (Tan et al., 2008). A robust model already used in petrochemical industries, and present in reservoir simulation software, is the perturbated chain-SAFT equation of state (PC-SAFT), developed by Gross and Sadowski (2001).

Regarding unconventional reservoirs, the geometrical confinement imposed to hydrocarbons changes fluid properties and its phase behavior, requiring additional parameters and details of the surface-fluid interaction (Gelb et al., 1999; Travalloni et al., 2014). PC-SAFT is one of the equations of state used as a base to create models for the phase coexistence and capillary effects of confined systems of interest to the oil and gas industry (Tan and Piri, 2015a,b; Barsotti et al., 2016).

Considering the natural gas main constituents (Pedersen et al., 2015; Wu et al., 2017; Baghooee et al., 2021), we calculate vapor-liquid equilibrium (VLE) of bulk methane and its binary mixtures with ethane and n-pentane using PC-SAFT equation of state. As a first knowledge of the systems, we evaluate only bulk conditions - that is further required for the study of the thermodiffusion phenomena. Data for pure components is also provided to evaluate the influence of heavier hydrocarbons on the phase equilibria of the fluid.

B.2 PC-SAFT equation of state

Equations of state derived from statistical mechanics principles enable the prediction of fluid properties from the interactions between its particles. The Statistical Associating Fluid Theory (SAFT) introduced by Chapman et al. (1990) is a successful molecular-based family of equations of state. Based on the perturbation theory of Barker and Henderson, Gross and Sadowski (2001) incorporated the effects of chain length on the dispersion term to describe non-associating components in the perturbed-chain SAFT (PC-SAFT) equation of state.

PC-SAFT equation of state (Eq. B.1) is given as the sum of the ideal gas contribution (id), a hard-sphere contribution (hs), a chain term ($chain$) connecting the spherical segments, a contribution for the dispersion attraction ($disp$), and a term for associating interactions ($assoc$). Further improvement was made by explicitly accounting for polar interactions to accurate describe the phase behavior of more complex mixtures (Gross, 2005; Gross and Vrabec, 2006; Vrabec and Gross, 2007; Tang and Gross, 2010).

$$A = A^{\text{id}} + A^{\text{hs}} + A^{\text{chain}} + A^{\text{disp}} + A^{\text{assoc}} \tag{B.1}$$

A non-polar substance is represented by only three pure component parameters: the number of segments, m, a segment size parameter, σ, and the segment energy parameter, ε/k_{B}, being k_{B} the Boltzmann constant. Table B.1 shows the parameters used on this chapter.

Table B.1: Pure component parameters for PC-SAFT equation of state from Gross and Sadowski (2001).

Component	m	σ **(Å)**	$\varepsilon/k_{\mathbf{B}}$ **(K)**
CH_4	1.0	3.7039	150.03
C_2H_6	1.6063	3.5210	191.45
C_5H_{12}	2.6896	3.7729	231.20

B.2.1 Pure components

Knowing the behavior of each component at the usual reservoir average temperature of 375 K (Santos et al., 2018) is crucial. We show the vapor-liquid properties of pure components in Fig. B.1. PC-SAFT data was obtained using the code kindly provided by Prof. Joachim Gross' research group (ITT).

An important property is the critical temperature, which can be found on Table B.2. Nevertheless, it is one of the most difficult properties to model due to phase instability. All the most common equations of state have difficulties predicting properties near the critical point because of the large density fluctuations. The values were calculated with PC-SAFT, and compared to a standard reference.

Table B.2: Critical temperature (K) of pure components

Component	**PC-SAFT**	**NIST**
CH_4	191.4	190.6
C_2H_6	309.0	305.3
C_5H_{12}	479.3	469.7

B.2.2 Binary mixtures

To access the influence of the heavier hydrocarbon on methane mixtures, we calculated the phase equilibria for binary mixtures at different temperatures using PC-SAFT equation of state (Fig. B.2).

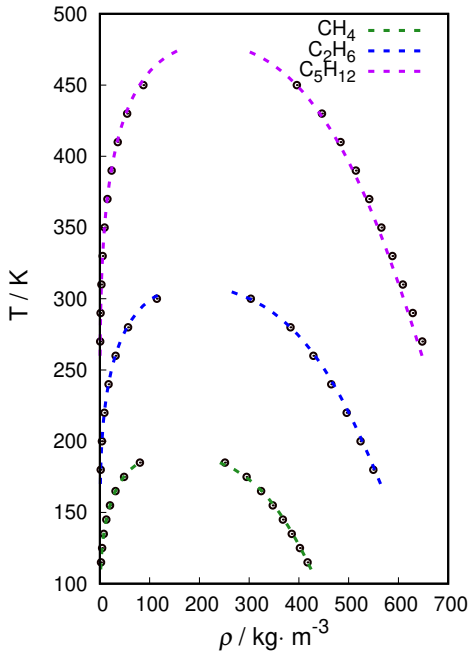

Figure B.1: Phase envelope of pure hydrocarbons from PC-SAFT (dashed lines). Reference values from NIST (Eric W. Lemmon and Friend, 2021) in open circles.

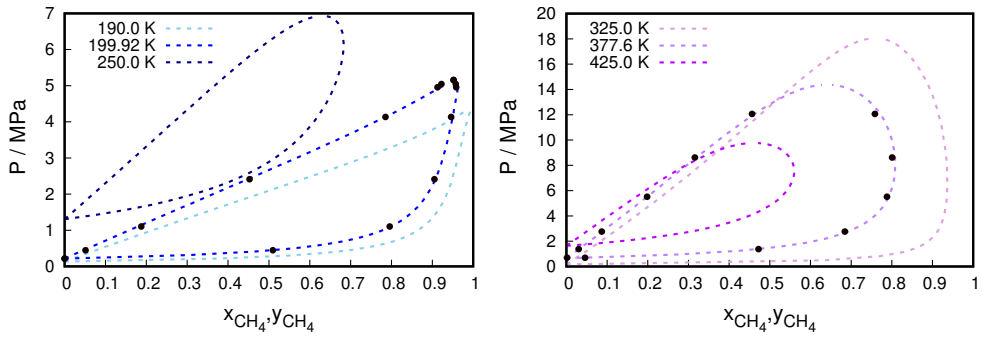

Figure B.2: Vapor-liquid coexistence curves for binary mixtures with methane. Dashed lines for PC-SAFT data at different temperatures, calculated at this work. Filled circles for experimental data. Blue: methane-ethane, experimental data at 199.92 K from Wichterle and Kobayashi (1972); Pink: methane-*n*-pentane, experimental data at 377.6 K from Sage et al. (1942).

Methane-*n*-pethane binary mixtures show phase separation for bulk fluids at 375 K, depending on pressure and on composition. Fluid phase behavior changes under confinement (Jin et al., 2017), but information of the unconfined system can guide our simulations.

Mixtures are described with regular Lorentz-Berthelot combining rules, with the introduction of a binary interaction parameter, k_{ij}, to correct the energy parameter according to Eq. B.2.

$$\varepsilon_{ij}/k_\mathrm{B} = \sqrt{(\varepsilon_i/k_\mathrm{B} \cdot \varepsilon_j/k_\mathrm{B})}(1 - k_{ij}) \tag{B.2}$$

Binary interaction parameters values were taken from Gross and Sadowski (2001) for ethane and n-pentane binary mixtures with methane. Average Absolute Relative Deviation (AARD) from experimental data was calculated with Eq. B.3, where N is the number of considered points, ϕ_i^{REF} is the experimental value from the literature, and ϕ_i^{CALC} is the value obtained using the equation of state.

$$\mathrm{AARD} = \frac{1}{N}\sum_{i=1}^{N}\frac{|\phi_i^{\mathrm{REF}} - \phi_i^{\mathrm{CALC}}|}{\phi_i^{\mathrm{REF}}} \tag{B.3}$$

Table B.3 presents the deviation results for mixtures with their respective k_{ij}. The description of the gas phase is much more accurate than the liquid phase, where interactions are stronger and deviations from ideality are higher.

Table B.3: Average absolute relative deviation (AARD) from VLE phase compositions calculated from PC-SAFT with experimental data of binary mixtures with methane.

Component	**T (K)**	k_{ij}	**AARD %**	
			x1	**y1**
C_2H_6	199.92	0	5.51	3.21
C_5H_{12}	377.60	0.024	0.24	0.04